THE IMPACT OF ION-HOST INTERACTIONS ON THE 5d-to-4f SPECTRA OF LANTHANIDE RARE EARTH IONS

by

BRIAN FRANCIS AULL

B.S.E.E., Purdue University
(1977)
S.M.E.E. and E.E., Massachusetts Institute of Technology
(1979)

Submitted to the Department of Electrical Engineering and Computer Science in Partial Fulfillment of the Requirements for the Degree of

DOCTOR OF PHILOSOPHY

at the

MASSACHUSETTS INSTITUTE OF TECHNOLOGY

June, 1985

Signature of Author_____
Department of Electrical Engineering and Computer Science
May 21, 1985

Certified by_____
Dr. Hans P. Jenssen
Thesis Supervisor

Accepted by_____
Professor Arthur C. Smith
Chairman, Departmental Committee on Graduate Students

THE IMPACT OF ION-HOST INTERACTIONS ON THE 5d-to-4f SPECTRA OF LANTHANIDE RARE EARTH IONS

by

BRIAN FRANCIS AULL

Submitted to the Department of Electrical Engineering and Computer Science on May 21, 1985 in partial fulfillment of the requirements for the Degree of Doctor of Philosophy in Electrical Engineering

Abstract

Dielectric crystals doped with Ce^{3+}, Eu^{2+}, Sm^{2+}, and Yb^{2+} display broadband 5d-to-4f emission, and are candidate solid-state tunable laser materials. The absorption and emission wavelengths, however, are very host-sensitive, and a better understanding of 5d crystal field interactions is needed in order to design high performance materials. The adequacy of a purely ionic model of the crystal field is experimentally tested.

Crystal growth of Ce-doped fluoride elpasolites is reported. Single crystals of Rb_2NaYF_6 and Rb_2NaScF_6 have been obtained by both vertical Bridgman and Czochralski techniques. Attempts to grow K_2NaYF_6 by both methods yielded only polycrystalline samples.

Ce-doped Rb_2NaYF_6 and K_2NaYF_6 display two distinct emitting centers, one in the blue and another in the near uv. $Ce:Rb_2NaScF_6$ displays only the blue-emitting center, and $Ce:K_2NaScF_6$ displays only the uv-emitting center. Growth and spectroscopic investigation of Rb_2NaYF_6 doped with other rare earths established that the blue-emitting center is Ce^{3+} in the normal (Y or Sc) site. The uv-emitting center is Ce^{3+} in a larger, lower symmetry site. It is hypothesized that this second site is related either to disordering or to the intergrowth of a second phase.

Absorption, emission, excitation, and vacuum uv transmission spectra were measured on Ce-doped elpasolites. Covalent contributions to the crystal field are numerically estimated by comparing the observed 5d energy levels with those predicted by an ionic-model calculation. These estimates as well as the qualitive dependence of the 5d energies on the lattice constant indicate that covalent contributions to the crystal field are significant.

The long-wavelength emission of Ce-doped elpasolites as compared to $Ce:LiYF_4$ is due to a lower 5d center of gravity, a larger Stokes shift, and larger 4f splittings. The anomalously broad emission bandwidth suggests that the Jahn-Teller effect on the emitting 5d level softens the

Jahn-Teller-active vibrational modes.

The Stokes shift increases with site size in the elpasolites, a counter example to the hypothesis of Blasse that it should decrease. Data on Ce-doped fluorides does not suggest that the Stokes shift displays any simple, universal pattern of correlation with site size or degree of site symmetry.

These results suggest three design rules for obtaining a visible-wavelength Ce^{3+} laser in a fluoride host:

1. Seek hosts in which nearest-neighbor cations and anions alternate along a straight line, including the substituted cation. This enhances the ligand polarizability along the dopant-ligand bond axis and brings the 5d centroid down. Simple cubic or perovskite lattices are good candidates.

2. Seek hosts with low coordination numbers (4 or 6), since this usually coincides with tight, strong-field sites.

3. Seek hosts with high site symmetry, so that the Jahn-Teller effect on the emitting 5d level can potentially contribute to the Stokes shift.

The elpasolites exemplify these criteria quite well.

Thesis Supervisor: Dr. Hans P. Jenssen
Title: Principal Research Associate

TABLE OF CONTENTS

LIST OF FIGURES

LIST OF TABLES

ACKNOWLEDGEMENTS

The author wishes, first and foremost, to acknowledge the guidance of his friend and mentor, Dr. Hans P. Jenssen. If I mature into as good an experimentalist as he is, I will have done well.

Other members of the Crystal Physics Laboratory made major contributions to this work. Dr. David Gabbe and Dr. Arthur Linz in particular guided my first timid steps into the field of crystal growth. Professor David Epstein served as my academic advisor throughout graduate school. As a reader of this thesis, he made many suggestions which substantially improved its quality.

This thesis could not have been completed without the assistance of Dr. Roger French. His vacuum uv spectroscopy system provided indispensible data.

Dr. Clyde Morrison and Dr. Richard Leavitt at Harry Diamond Labs discussed the intricacies of crystal field theory with me on numerous occasions, and provided many calculations which were immensely helpful.

A special note of thanks goes to Professor Michel Baranger, whose superb teaching of 8.321 and 8.322 provided the author with an understanding of quantum mechanics which proved indispensible in the course of the research.

Several of the figures were drawn by my father-in-law, Mr. Bill Foster. Several others were drawn by Mr. John Mara.

The author thanks his wife, Zarrin-Taj Foster, for being a kind and loving helpmate throughout the past three years.

The author thanks his parents, Roger Aull and Wilma Gootee, for providing nurturing and encouragement throughout life. I would never have reached this point without it.

Other notes of thanks go to Elaine Cook, Vladimir Belruss, Frank Payne and Peter Kloumann for logistical support. Peter's patience with my stealing his voltmeter is specially acknowledged. Thanks also go to Dr. Charles Naiman, Prof. David Adler, Stanley Rotman, Prof. Harry Tuller, and Prof. Bernard Wuensch for valuable suggestions.

My fellowship and many of my research expenses were subsidized by Sanders Associates during the past three years. My thanks to Tom Pollak and Evan Chicklis at Sanders for their support. Additional funding was provided by the Army-Electronics Research and Development Command under contract DAAK20-82-C-0135.

As regards thine assertions about the beginning of creation, this is a matter on which conceptions vary by reason of the divergences in men's thoughts and opinions...

That which hath been in existence had existed before, but not in the form thou seest today. The world of existence came into being through the heat generated from the interaction between the active force and that which is its recipient. These two are the same, yet they are different. Thus doth the Great Announcement inform thee about this glorious structure.

-from The Tablet of Wisdom,
revealed by Baha'u'llah in the
prison of 'Akka (c. 1885)

CHAPTER I

INTRODUCTION

In recent years there has been a growing interest in solid-state tunable lasers based on impurity-doped dielectric crystals. For example, crystals doped with transition-metal ions such as chrysoberyl doped with Cr^{3+} [1], MgF_2 with Ni^{2+} [2] and with Co^{2+} [3] have been lased. The iron-group transition-metal ions display vibrationally assisted optical transitions within the 3d shell and generally lase in the red or near ir region.

The lack of tunable solid-state lasers at shorter visible wavelengths has motivated investigation of the 5d-to-4f optical transitions of lanthanide rare earths, particularly Ce^{3+}, Eu^{2+}, Sm^{2+}, and Yb^{2+}. Figures 1 through 4 are typical energy-level diagrams of these ions for cubal* coordination in fluoride hosts. Optical transitions between the $4f^N$ ground state and the first excited configuration $4f^{N-1}5d$ are parity-allowed, and because of the large spatial

---

* The terminology of McClure [4] is used here, in which the term "cubic" denotes any field of O_h symmetry, and "cubal" denotes the more specific case of a cubic field produced by eight ligands at the corners of a cube. "Octahedral" denotes a cubic field produced by six ligands at the corners of an octahedron.

extent of the 5d wavefunction, they are vibrationally broadened much more than the forced electric-dipole transitions which occur within the 4f shell. 5d-to-4f emission bands in crystals are typically several tens of nanometers in width. By the same token, the peak wavelength of the emission band varies greatly from host to host, and a few examples illustrate that this causes the choice of host to be a critical design parameter.

Ce^{3+}:$LiYF_4$ and Ce^{3+}:LaF_3 have been lased [5,6], but the lasing wavelengths are in the near uv near 300 nm. Ce^{3+}:YAG emits in the visible, but laser action seems to be frustrated by excited-state absorption losses [7,8].

The fluorescence of Eu^{2+} and Sm^{2+} has been studied in many hosts. The lowest 5d levels of Eu^{2+} and of Sm^{2+} often lie close to excited 4f levels ($^6P_{7/2}$ in Eu^{2+}, and $^5D_0$ in Sm^{2+}). Unless the crystal field lowers this 5d level to below these excited 4f levels, it will be completely depopulated by rapid relaxation, and there will be no broadband emission. Even if broadband emission occurs, there may be excited 4f levels at twice the energy of this emission, leading to allowed excited-state absorption transitions. Thus a 1000-wavenumber change in the 5d crystal field splitting, the 5d centroid, or the Stokes shift could "make or break" tunable laser action.

Yb^{2+} fluorescence has been studied in many hosts and usually displays broadband emission, but with an anomalously long lifetime for an ostensibly allowed transition (60 μs in

$LiBaF_3$). One probable reason for the long lifetime is that one of the 6s levels lies just below the 5d levels [9]. Another is the $^1S_0$ character of the ground state. This raises the question of how the lifetime might be manipulated by judicious choice of host crystal.

The foregoing discussion establishes the importance of understanding crystal field effects on the 5d levels. In order to "design" good tunable lasers, we must be able to predict the spectroscopic effects of parameters such as site size, site symmetry, ligand electronegativity, and host covalency. This requires that we study trends that occur when the host is varied in systematic ways. This work deals with the more specific issue of how to vary the 5d energies in fluoride hosts, that is, with the effects of site size and symmetry.

In the case of Ce^{3+}, three spectroscopic parameters are of interest, as illustrated in Figure 5. First, the center of gravity of the 5d configuration is lower in a polarizable matrix than in the free ion (using the 4f ground state as the zero of energy). The parameter Δ measures this centroid shift. Second, the 5d level is split by the crystal field. Figure 5 shows the splitting, 10Dq, for a field of cubic symmetry. For lower symmetry fields, there will be more than one splitting parameter. Third, the emission from the lowest 5d level to the ground state is at a lower energy than the corresponding absorption because of lattice relax-

ation. This is S, the Stokes shift.

In most of the spectroscopy reported on Eu^{2+}, Sm^{2+}, and Yb^{2+}, with their more complex configurations, the investigators use a strong field description [10] of the 5d electron and ignore the d-f coulombic coupling. This may be a reasonable starting point; however, the problem with many of the "host dependence" studies in the literature is that the three parameters in Figure 5 are not separately measured. Bril et. al. [11], for example, reported room-temperature emission spectra of several Ce-doped oxide powders, but it is not possible to tell from their data whether a red shift from host to host is due to a larger splitting, a lower centroid, or a larger Stokes shift.

One of the best examples of "host dependence" studies is the work of Hernandez et. al. [10]. They reported room-temperature absorption and emission spectra of Eu^{2+}-doped alkali halides. Using the centroids of the two observed absorption bands as energy values for the e_g and t_{2g} levels of the 5d electron, they tabulated the crystal field splitting (10Dq), the 5d centroid, and the Stokes shift in all these hosts. The lattice-constant dependence of the splitting deviates from what is predicted by a point charge model ($1/R^5$), and they ascribe this to "contact interactions."

Interpretation of the Hernandez data is complicated by several factors, however. First, the excited configuration of Eu^{2+} is $4f^65d$, so that the "5d levels" are complicated by

the f-f and d-f coulombic and exchange splittings of the free ion. These interactions are effectively modified by a polarizable host. The absorption spectrum from the $^8S_{7/2}$ reveals levels with octet spin character, and not levels with sextet spin character. Thus the assignment of a "5d splitting" and a "5d centroid" on the basis of absorption bands is questionable.

Second, incorporation of Eu^{2+} into the alkali halides requires charge compensation, which lowers the site symmetry. Hernandez neglects this, and it is uncertain how much impact this factor has.

Third, the incorporation of any dopant ion must distort the lattice locally, even if the distortion does not lower the site symmetry. Of all possible "contact interactions", this one should be considered before worrying about departures from ionicity. Thus the lattice constants used to plot the Hernandez data should be replaced by the actual nearest neighbor distances at the dopant site (although determination of this may be difficult).

The purpose of this work is to study crystal field effects on the 5d levels of rare earths in the same manner as Hernandez et. al., that is to measure 5d energies in a series of isostructural hosts. However, this work will focus on the Ce^{3+} ion. Ce^{3+} has only one electron in its 4f shell, so there are no coulombic or exchange splittings

complicating the interpretation of absorption spectra.

The hosts used in this work are fluorides of the elpasolite structure (A_2BRF_6, where A and B are alkali metals, R is Sc or Y). Fluoride crystals are advantageous because of their wide bandgap and highly ionic character. This assures transparency well into the uv. Furthermore, this study is a testing ground for departures from a purely electrostatic model of crystal field effects, and highly ionic crystals provide a better test than covalent ones.

The elpasolites specifically are advantageous because the R site is an isovalent site for Ce^{3+} with perfect O_h symmetry and octahedral F coordination. Thus the 5d level splits into two levels and there is only one crystal field splitting parameter to measure (B_{40} or equivalently, 10Dq). The high symmetry is also advantageous because it gives rise to a splitting which decreases rapidly with the distance from neighboring ions. For example, the splitting displays a $1/R^5$ range dependence in a point charge model, so the contribution to the splitting from the second-nearest neighbors is at least an order of magnitude smaller than the nearest-neighbor contribution. This is ideal for studying the "contact interactions" referred to by Hernandez.

The strategy of this research has been to grow and spectroscopically evaluate several Ce^{3+}-doped elpasolites with a range of site sizes and lattice constants, and compare 5d splittings and centroids to the predictions of a totally ionic model for the crystal field interactions. The

reasons for the vastly different emission spectra of $Ce:LiYF_4$ (YLF) and $Ce:Rb_2NaYF_6$ are explored. The trend in the Stokes shifts is also discussed, and elpasolite is compared to lower symmetry systems in relation to the current state of knowledge about the Stokes shift.

Chapter II is a review of ligand field theory, focusing particularly on the electrostatic model and on its shortcomings, on the covalent-complex approach, and on lattice relaxation and vibronic effects. Chapter III describes the crystal growth and x-ray analysis of the elpasolites. Chapter IV presents the spectroscopic evaluation, and the investigation of unexpected inhomogeneities present in Ce^{3+}-doped elpasolites. In Chapter V a model for the 5d splitting and centroid shift is presented and its predictions compared with the data. Comparisons are made with YLF and other low symmetry systems. Chapter VI presents conclusions and proposes further work.

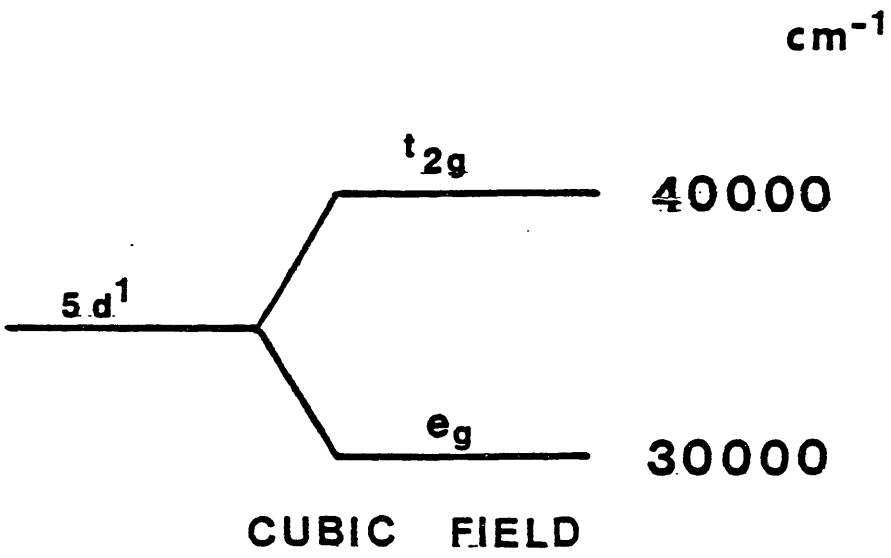

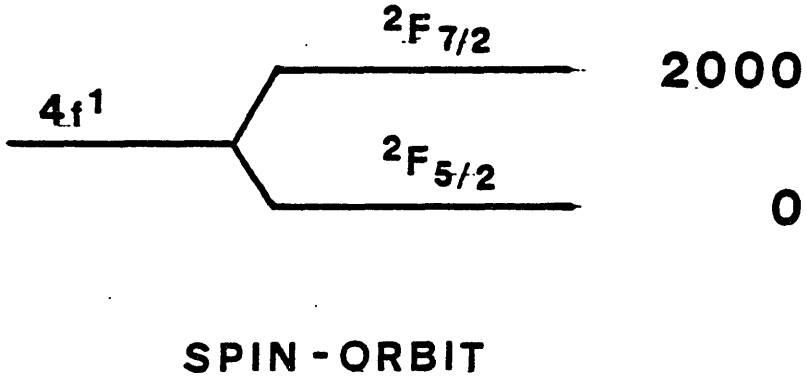

FIGURE 1 Ce^{3+} ENERGY LEVELS

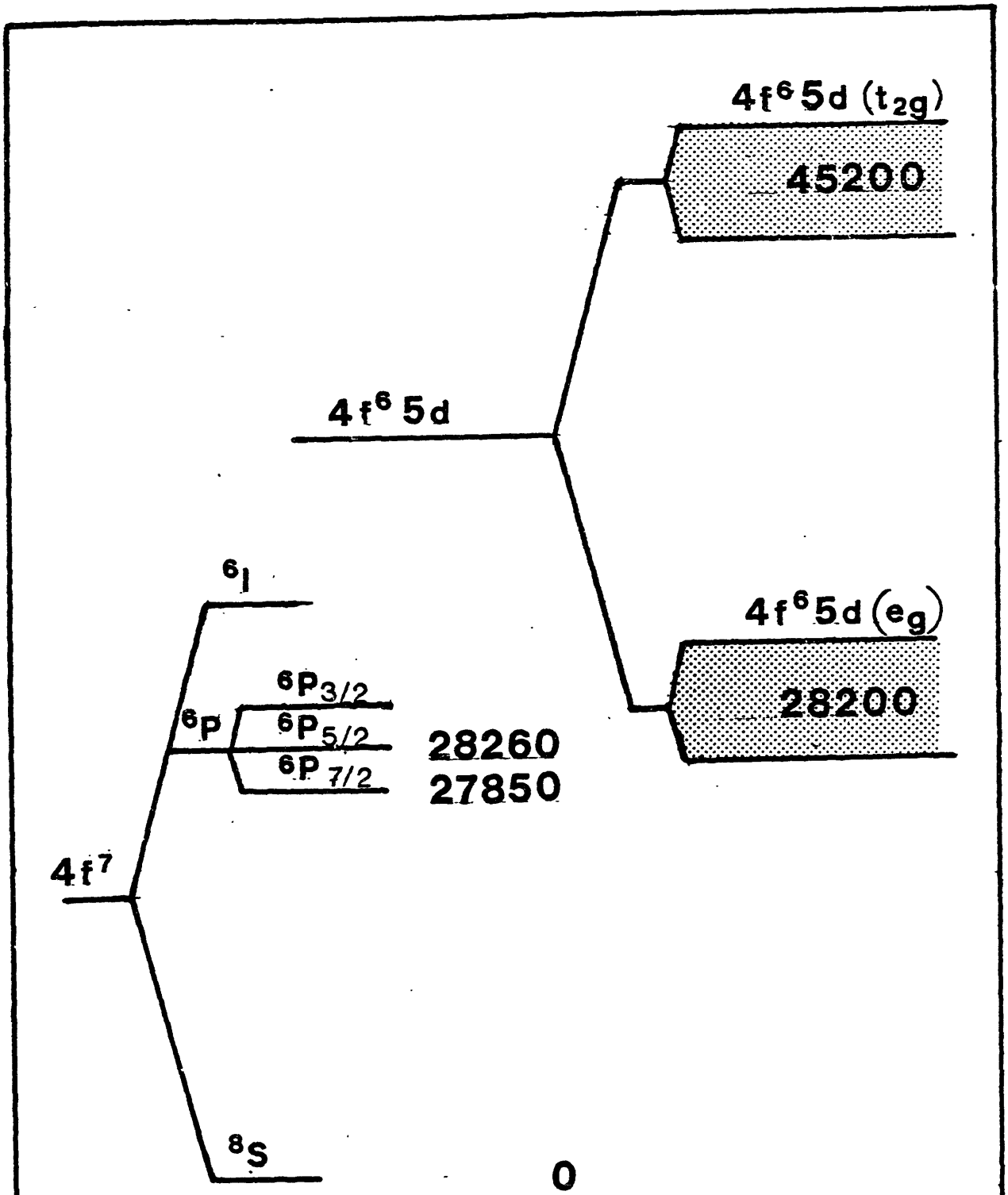

FIGURE 2 Eu^{2+} ENERGY LEVELS

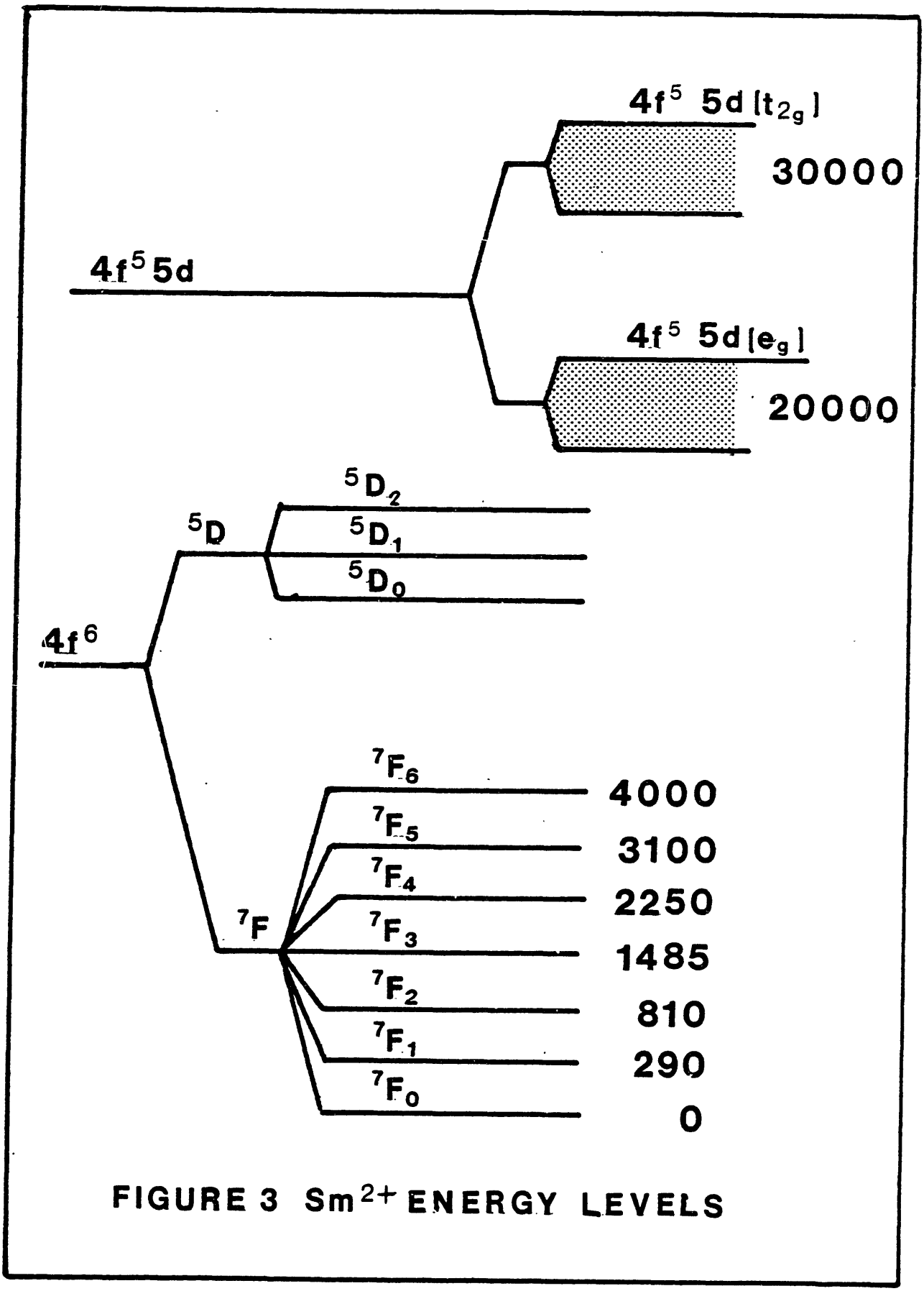

FIGURE 3 Sm^{2+} ENERGY LEVELS

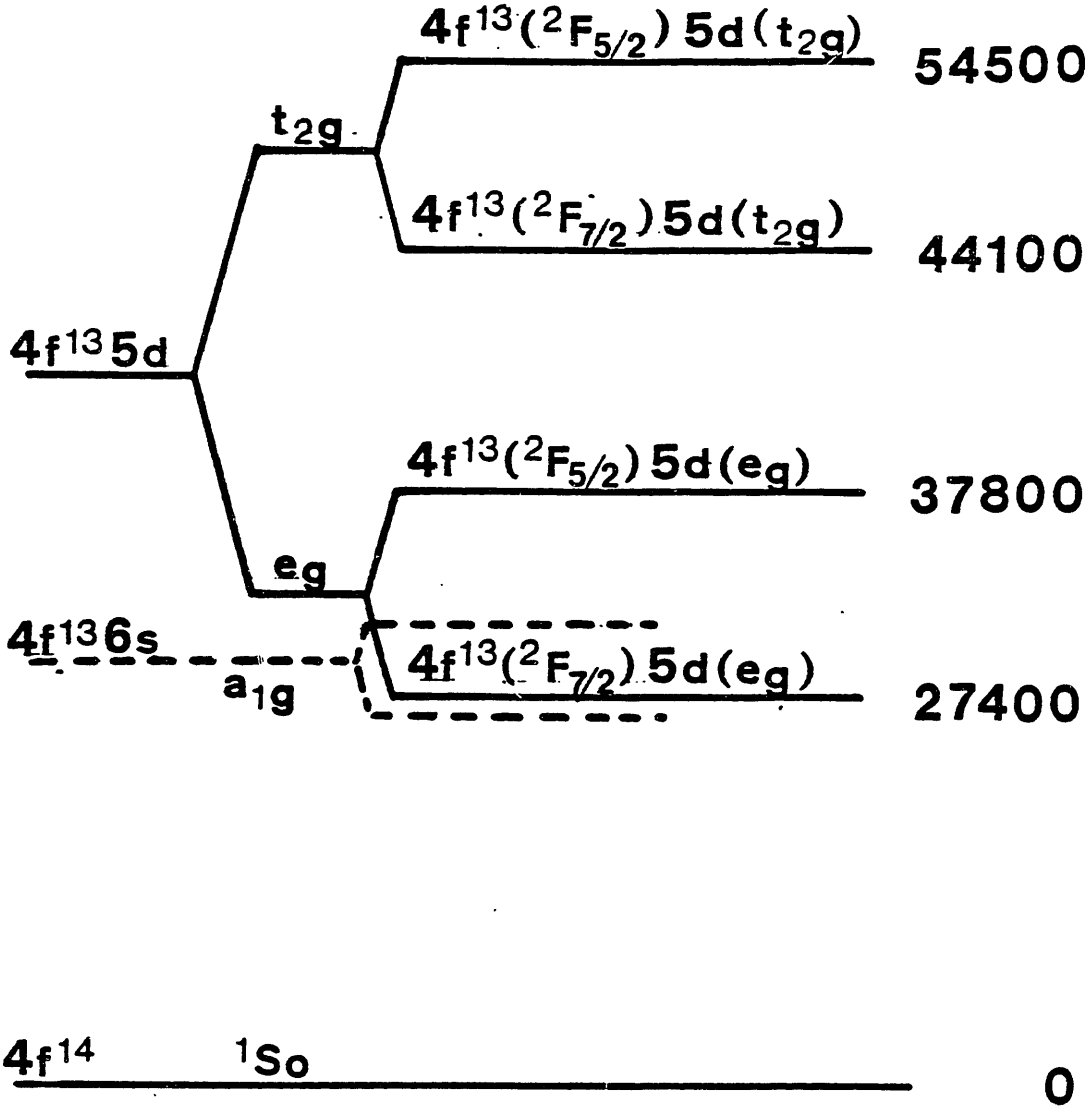

FIGURE 4 Yb^{2+} ENERGY LEVELS

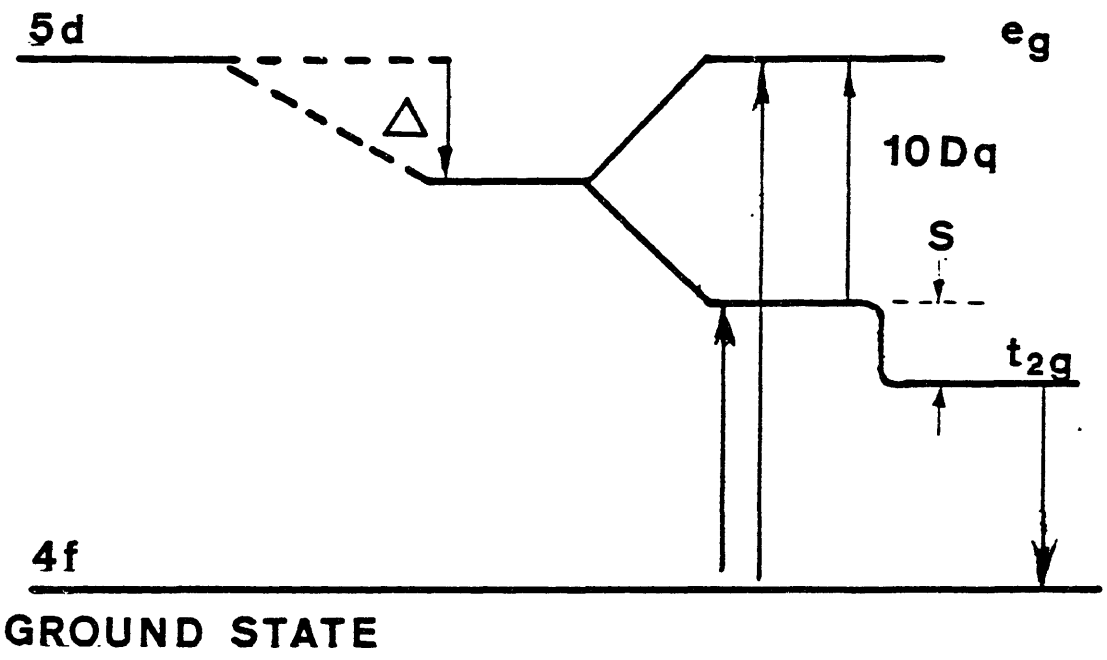

FIGURE 5 Ce^{3+} spectroscopic parameters in a cubic crystal field

CHAPTER II

LIGAND FIELD THEORY

2.1 The Electrostatic Crystal Field Model

The crystal field interaction for a localized state of an impurity atom is generally expanded in spherical harmonics. For the i^{th} electron at position r_i

$$V(r_i) = \Sigma\, B_{kq}(r_i)C_{kq}(\hat{r_i}) \qquad (1)$$

where $\hat{r_i}$ denotes the angular part of r_i and the radial dependence is in the crystal field parameter B_{kq}. The C_{kq} are the spherical harmonics. If the crystal field arises from *fixed* classical electrostatic charge distributions in the lattice, it must obey Poisson's equation. If the charge distributions do not overlap the 4f or 5d wavefunction in question, the field must obey Laplace's equation. The solution to Laplace's equation in spherical coordinates is (1), provided that

$$B_{kq} = A_{kq}r^k \qquad (2)$$

where A_{kq} is a constant, and the subscript i is dropped. If

the lattice charge distributions are expanded in multipoles, it is found that a 2^p-pole moment located a distance R away contributes a term proportional to $R^{-(k+p+1)}$ to the A_{kq} parameter.

In O_h site symmetry, (1) becomes

$$V(r) = A_{00} + A_{40}r^4\{C_{40}(\hat{r}) + 5[C_{44}(\hat{r}) + C_{4\bar{4}}(\hat{r})]/\sqrt{70}\} \quad (3)$$

For d electrons the matrix elements vanish for k>4. The A_{00} term is the Madelung potential, and for negatively charged ligands this quantity is positive, destabilizing 4f and 5d electrons by the same amount. The A_{40} term splits the d level into e_g and t_{2g} levels with energies

$$E(e_g) = E_{centroid} + 6Dq$$
$$E(t_{2g}) = E_{centroid} - 4Dq \quad (4)$$

In this model, the point charge contribution to Dq for an octahedral $(CeF_6)^{3-}$ complex is positive because the lobes of the e_g wavefunction point toward the repulsive F^- ligands, and the lobes of the t_{2g} wavefunctions avoid them. This point charge splitting has a $1/R^5$ range dependence. (NOTE: The parameter 10Dq is often used as a purely experimental parameter quantifying a splitting. In this work, it is also strictly identified with the parameter B_{40}. For the d electron, B_{40}=21Dq.)

The ligands also possess permanent multipole moments induced by the crystal field. This "lattice-induced" multipole field must be self-consistently solved; that is, the point charge field induces multipole moments on all the atoms, and the field due to these moments induce more moments, and so on [12]. For a highly charged cation like Ce^{3+} in an isovalent site, lattice-induced multipole moments would tend to make the ligands more repulsive to the 5d electron. Another effect which contributes to the multipole moments of the ligands is the field due to the instantaneous displacement of the 5d electron. This gives rise to a correlation crystal field, to be discussed in section 2.3, but also causes the ligands to look more attractive on the average. The latter effect is called the "self-induced" multipole field [13]. As long as the ligands are modeled as *point multipoles*, both lattice-induced and self-induced fields obey (1) and (2).

So far we have insisted on a crystal field that obeys Laplace's equation. Such a model predicts that the 5d-4f centroid difference should be unchanged from the free ion value (neglecting configuration mixing by the crystal field). It further predicts a cubic 5d splitting whose leading contribution goes as $1/R^5$, where R is the metal-to-ligand distance.

The model can be refined by solving Poisson's equation, that is, by regarding the ligands as delocalized charge

clouds obtained by summing the squared magnitudes of ligand orbitals, and then calculating the crystal field classically. We will refer to this as "classical overlap", although in the absence of actual metal-ligand overlap, it is equivalent to including all terms in a ligand multipole expansion.

2.2 Failures of Electrostatic Crystal Field Theory

Experimentally, there are deficiencies in the electrostatic crystal field model, even for 4f electrons. Morrison [12] points out that corrections must be introduced for screening and covalency. Furthermore, the 5d-4f centroid difference decreases quite significantly for rare earths in crystals. In Ce:YLF, for example, the shift is 6000 cm^{-1} with respect to the free ion value.

The inclusion of classical overlap in the calculation of splittings makes things even worse. Such calculations were done by Kleiner [14] on 3d electrons and by Garcia and Faucher [15] on 4f electrons; the delocalization of the ligand electron clouds in this model causes the positive ligand cores to become more "visible". As a result, F^-, Cl^-, or O^{2-} ligands are predicted to be more "attractive" than they really are experimentally. The discrepancy is accentuated for higher-rank crystal field components because

of the r^k weighting.

In order to clarify and classify what is missing from electrostatic crystal field theory, consider a simple quantum mechanical model. Let r_1 be the coordinate of a 5d electron on a Ce^{3+} ion and r_2 the coordinate of a ligand electron. Let both electrons be moving in a common background potential V(r). Let us write the wavefunction as a Slater determinant.

$$\Psi(r_1,r_2) = [\phi_M(r_1)\phi_L(r_2) - \phi_L(r_1)\phi_M(r_2)]/\sqrt{2} \qquad (5)$$

The first order energy of the system is

$$E = E_M + E_L + \langle\phi_M\phi_L|e^2/r_{12}|\phi_M\phi_L\rangle$$
$$- \delta(m_{sL},m_{sM})\langle\phi_M\phi_L|e^2/r_{12}|\phi_L\phi_M\rangle \qquad (6)$$

The first two terms are the eigenvalues for the metal and ligand orbitals, respectively, in the absence of the coulomb repulsion. The third term is the coulomb repulsion and the last term is the exchange. In the product bras and kets, the first orbital is a function of the coordinate of electron 1, and the second orbital, electron 2.

If we assume that $|\phi_M\rangle$ and $|\phi_L\rangle$ are non-overlapping atomic orbitals, then $|\phi_M\rangle$ diagonalizes the one-body Hamiltonian,

$$H = p^2/2m + V + \int d^3r_2 |\phi_L(r_2)|^2 e^2/r_{12} \qquad (7)$$

The effective ligand field obeys Laplace's equation, and (2) is valid. If there is overlap, but the exchange term in (6) is ignored, the third term in (7) obeys Poisson's equation. In either case, (7) is a quantum mechanical equivalent of classical crystal field theory which includes the classical overlap field due to one ligand electron.

To go beyond electrostatic crystal field theory, several refinements in the model are possible:

1. Improve $|\phi_M\rangle$ and/or $|\phi_L\rangle$ by allowing configuration mixing by the crystal field.
2. Include the exchange term of (6) in the Hamiltonian.
3. Improve $|\phi_M\rangle$ and $|\phi_L\rangle$ by allowing for covalency. That is, admix $|\phi_L\rangle$ and $|\phi_M\rangle$ to form bonding and antibonding orbitals.
4. Include correlations between the orbital motions of the ligand and metal electrons.

Most crystal field calculations start by using the best available free ion wavefunctions and neglecting additional configuration mixing entirely. Sugano and Shulman [16] have done covalency calculations on Ni^{2+} in $KNiF_3$, incorporating improvements 2 and 3 above. They obtained 3d splittings

that are close to experimental values. We will discuss this approach to ligand field theory in detail, but first let us examine correlation crystal fields.

2.3 Correlation Crystal Fields

Regardless of how much we embellish the functions ϕ_M and ϕ_L in (5), our quantum mechanical model still cannot incorporate explicitly coupled orbital motions of the metal and ligand electrons. The original motive for investigating correlation crystal fields was the observation of host-induced shifts in the coulombic repulsion parameters of rare earths. Morrison [12] gives a semiclassical analysis of this mechanism, which we summarize here. The term "correlation crystal field" is used here in a different way than it is by Newman [17], who uses the term to denote any interaction which can be parameterized by two-electron crystal field parameters.

The instantaneous displacement of a 4f (or 5d) electron induces multipole moments on the ligands, and the field due to these moments reacts back on the electron or on other electrons. In the case of Ce^{3+}, the self-interaction is most important because it explains the 4f-5d centroid shift. In the case of many-electron configurations, as in the divalent rare earths, the two-electron crystal field is also

important.

Referring to Figure 6, let there be a ligand at **R** and two electrons at r_1 and r_2 with respect to the metal ion. $\mathbf{R}_1$ and $\mathbf{R}_2$ are the vectors from electrons 1 and 2, respectively, to the ligand. The electrostatic potential at the ligand due to the field of electron 1 is expanded in spherical harmonics.

$$\phi(\mathbf{R}_1+\mathbf{x}) = -\Sigma\, E^{*}_{nm}(R_1)x^n C_{nm}(\hat{x}) \tag{8}$$

where

$$E_{nm} = e(-1)^n C_{nm}(\hat{R}_1)/R_1^{n+1}$$

Each term in the above sum induces a multipole moment Q_{nm} on the ligand given by

$$Q_{nm} = \alpha_n E_{nm} \tag{9}$$

The potential of electron 2 in the field of the n^{th}-rank multipole is

$$U^{(n)} = -e\Sigma\, Q_{nm}(-1)^n C_{nm}(\hat{R}_2)/R_2^{n+1} \tag{10}$$

The sum is over m. Substitution yields

$$U^{(n)}(r_1,r_2) = -e^2\alpha_n\Sigma\, C_{nm}(\hat{R}_1)C'_{nm}(\hat{R}_2)/R_1^{n+1}R_2^{n+1} \tag{11}$$

The self-interaction is obtained by setting $R_1 = R_2$ and introducing a factor of 1/2 to account for the disappearance of the second electron.

$$U^{(n)}(r_1) = -e^2\alpha_n/2R_1^{2n+2} \tag{12}$$

Next, (12) must be expanded in r_1. The leading two spherically symmetric terms turn out to be

$$U^{(n)}(r_1) = -e^2\alpha_n[1/R^{2n+2} + (n+1)(n+2)r_1^2/3R^{2n+4}]/2 \tag{13}$$

In the special case of dipoles (n = 1) this is

$$U^{(1)}(r_1) = -e^2\alpha(1/R^4 + 2r_1^2/R^6)/2 \tag{14}$$

The first term is a "self-induced" contribution to the Madelung potential which is not really correlation. It could have been incorporated into our quantum mechanical model (5) by admixing excited ligand orbitals into ϕ_L.

The second term of (14) is an isotropic parabolic potential with a maximum at r = 0, an apparent violation of classical electrostatic theory. This term arises purely from correlation. It causes the effective one-electron potential of the metal ion to be "less steep", which decreases energy differences between configurations. In particular, the 5d-4f centroid difference changes by the

amount

$$\Delta = -\alpha e^2[\langle r^2\rangle_{5d} - \langle r^2\rangle_{4f}]/R^6 \qquad (15)$$

If there are many ligands with different values of R and α, we sum them.

Similarly we can treat the fourfold field, obtaining a mean self-induced B_{4q} proportional to $\langle r^4\rangle/R^8$ and a correlation B_{4q} proportional to $\langle r^6\rangle/R^{10}$.

This semiclassical approach yields the same results as a more rigorous quantum mechanical analysis [18], as long as it is understood that the polarizability used is the in-crystal value rather than the free ion value.

2.4 Covalency

So far we have considered a strictly ionic model, that is, one not allowing for any electronic excitations which involve transfer of charge between the ligand and metal ions. There is good evidence that such effects have important spectroscopic consequences for 3d electrons. Sugano and Shulman [16] performed NMR and optical measurements on $KNiF_3$, and showed that their results fit a covalency model in which the F^- 2s, $2p\sigma$, and $2p\pi$ orbitals display different amounts of mixing with Ni^{2+} 3d orbitals.

They performed a calculation of the 3d cubic splitting using a Hartree-Fock potential which was the superposition of free-ion Hartree-Fock potentials. Their trial wavefunctions were

$$\Psi_{ai} = (\phi_i - \lambda_i \chi_i)/\sqrt{N_i}$$
$$\Psi_{bi} = (\chi_i + \gamma_i \phi_i)/\sqrt{N_i'} \qquad (16)$$

where ϕ_i is a metal orbital, and χ_i a ligand-complex orbital. N_i and N_i' are normalization constants. Orthogonality of the antibonding and bonding wavefunctions imposes the constraint $\lambda_i = \gamma_i + S_i$, where S_i is the overlap, $\langle\phi|\chi\rangle$. The i subscript in (16) includes an O_h symmetry group representation and partner index. So χ_i is a linear combination of ligand s or p orbitals which transforms like ϕ_i.

The phase factors of the orbitals ϕ and χ are such that they constructively interfere in the bonding region. Thus the parameters S, γ, and λ are positive, and the algebraic signs in (16) are physically significant, indicating charge buildup in the bond region for the bonding orbital, and a node in the bond region for the antibonding orbital.

The calculation of Sugano and Shulman is equivalent to a variational approach, minimizing the energy of the system with respect to the parameter γ. The Hamiltonian of the

system is written with a one-body potential which has the full symmetry of the complex.

$$H = \Sigma\, T + V_M + V_L \tag{17}$$

The summation is over the electrons, T is the kinetic energy operator, V_M is the metal ion potential, and V_L is the ligand-complex potential.

For each value of the label i, which we drop, the bonding and antibonding orbital energies are

$$E_a = E_M' + [S\langle\phi|V_L|\phi\rangle - \langle\phi|V_L|\chi\rangle]^2/(E_M' - E_L')$$
$$E_b = E_L' - [S\langle\chi|V_M|\chi\rangle - \langle\phi|V_M|\chi\rangle]^2/(E_M' - E_L') \tag{18}$$

where
$$E_M' = E_M + \langle\phi|V_L|\phi\rangle$$
$$E_L' = E_L + \langle\chi|V_M|\chi\rangle$$
and
$$(T + V_M)\phi = E_M\phi$$
$$(T + V_L)\chi = E_L\chi$$

This model is an isolated complex model, and the rest of the crystal merely fixes the bond distances. The Madelung potential at the metal ion site should be added to E_M, and the Madelung potential at the ligand site should be added to E_L. Sugano and Shulman neglect contributions to this from outside the NiF_6 complex.

Sugano and Shulman measure the "amount of covalency" by

the parameter γ, not λ or S. This is physically reasonable because $\gamma>0$ indicates bonding. If $\gamma=0$, however, there is still "antibonding" needed to assure orthogonality. That is, we have

$$\Psi_a = (\phi - S\chi)/\sqrt{1-S^2}$$

$$\Psi_b = \chi \qquad (19)$$

Thus $\langle\Psi_a|H|\Psi_a\rangle$ contains a term of the form $-S\langle\chi|H|\phi\rangle$ which is ascribed to "non-orthogonality" rather than to "covalency". The normalization coefficient in (16) introduces a term of the form $(2\lambda S - S^2)\langle\phi|H|\phi\rangle$ which is termed "renormalization." Sugano and Shulman reserve the term "covalency" exclusively for contributions arising from non-zero γ.

Sugano and Shulman determine an experimental value for 10Dq by measuring the absorption from the (t^6e^2) $^3A_2$ ground state to the (t^5e^3) $^3T_2$ excited state of Ni^{2+}. This experimental value was 7250 cm^{-1}. The calculated value was 6350 cm^{-1}, and the breakdown of the contributions to this are shown in Table I.

TABLE I Calculated Contributions to 10Dq of Ni^{2+} in $KNiF_3$ (cm^{-1})[16]

Point charge	1390
Classical overlap	-2080
Exchange	-2880
Renormalization	900
Non-orthogonality	3730
Covalency	5290
Total	6350
Experimental	7250

Neglect of metal-ligand wavefunction mixing ($S=\gamma=\lambda=0$) leads to a crystal field splitting of the wrong sign because of the attractive exchange and classical overlap interactions. The other terms are all repulsive. The covalency gives a surprisingly large percentage of the total splitting. The calculated mixing is also quite large. λ for $p\sigma$ is 0.396, for example.

The NMR measurements of Sugano and Shulman measure the covalency in a more direct fashion. The applied magnetic field necessary to produce a an ^{19}F hyperfine splitting of 60 MHz was measured as a function of the angle between the field and the 100 axis. The F atom sits at a site of D_{4h} symmetry, halfway between two Ni^{2+} ions on the symmetry axis. In the absence of covalency, a simple dipolar sum predicts the additional field at the F nucleus due to the

unpaired 3d electron spins. This gives an anisotropic contribution to the NMR spectrum. A nonzero value of λ causes unpaired electron spin density to be introduced into the F 2s and 2p orbitals. This introduces an isotropic shift in the NMR spectrum, and the difference between the $2p\sigma$ and $2p\pi$ spin densities introduces an additional anisotropic contribution. In this way, the value of $\lambda/\sqrt{N}$ in (16) can be deduced and compared to the calculated value.

For Ni^{2+} the ground state does not π antibond, so the hyperfine shift is solely due to 2s and $2p\sigma$ antibonding. The results are shown in Table II.

TABLE II $\lambda/\sqrt{N}$ values of Sugano and Shulman

	Calc.	NMR
s	0.109	0.116
σ	0.383	0.337

Sugano and Shulman point out that there have been other explanations proposed for the large crystal field splitting. Radial wavefunction expansion (configuration mixing) has been invoked, for example. However, Sugano and Shulman find that the covalency explains Racah parameter shifts just as well, and that wavefunction expansion is inconsistent with the lack of any observable shift in the spin-orbit parameter, and is also inconsistent with NMR data.

Several methods of approximation have been applied to (18). The extended Huckel method, and Wolfsberg-Helmholtz approximation [19] both express the numerator of the covalency term as S^2 times the square of an effective diagonal matrix element. Therefore, to a first approximation, the antibonding destabilization energies should have an exponential dependence on the metal-ligand distance.

For Ce^{3+} in elpasolite the overlap of the 5d wavefunction with the fluorine ligand should be similar in magnitude to the case of Ni^{2+} in $KNiF_3$. Covalency probably plays a significant role in the crystal field effects. Unfortunately, the 5d levels are excited states with extremely short lifetimes (70 ns), so direct measurement of 5d covalency by means of NMR or ESR is not feasible. The strategy adopted in this work is to deduce covalent contributions to the crystal field by comparing the splittings and centroids observed in optical spectra with those calculated on the basis of a purely ionic model.

The 5d splitting of Ce^{3+} in an octahedral field would have a contribution proportional to the difference between the e_g σ and s antibonding energy and the t_{2g} π antibonding energy. This contribution should have the same sign as the point charge contribution. A degeneracy-weighted average of these antibonding energies gives a positive centroid shift.

2.5 Configuration Mixing

In this work the term "configuration interaction" will be used to denote admixture of atomic configurations by the coulombic repulsion interaction of the free ion. "Configuration mixing" will denote an additional admixture introduced by the crystal field.

Configuration interaction is a spherically symmetric interaction in the product space of all the electrons, mixing states with the same values of L, S, and other quantum numbers indicating Lie group representations. The quantum number ℓ is not valid, but for a lone 4f or 5d electron plus closed shells, ℓ mixing is negligible. The principal effect is n mixing, which arises from the spherically symmetric interaction with the closed shells and leads to wavefunction expansion with respect to hydrogenic wavefunctions. In multielectron configurations (like Pr^{3+} $4f^2$) ℓ mixing is significant and leads to an L and S dependence of the phenomenological crystal field parameters. This effect has been parameterized by Newman [17] as a two-electron crystal field ("correlation crystal field" in his terminology).

Configuration mixing, on the other hand, is a departure from spherical symmetry which has several potentially important consequences for Ce^{3+}. First, the crystal field acting on the (Xe) core mixes excited configurations into the $5s^25p^6$ state, which in turn alters the effective crystal

field on the 4f or 5d electron. For 4f electrons in the rare earths, this effect shields the crystal field. Sternheimer [20] calculated reduction factors for $4f^n$ crystal field parameters, and found that A_{2q} is reduced by about 65 percent, A_{4q} by 9 percent, and A_{6q} by 4 percent. For 5d electrons this effect will lead to less shielding because the 5d wavefunction extends further outside the (Xe) core, but quantitative values for the shielding parameters are not known. This effect does not alter the range dependence of the crystal field, that is, a shielded point charge B_{40} still has a $1/R^5$ dependence. Experimentally, however, this effect would manifest itself in a difference between the phenomenological A_{kq} obtained for 4f electrons and those obtained for 5d electrons (assuming the $\langle r^k \rangle$ values used are valid).

The second consequence of configuration mixing is that it acts on the 4f or 5d state directly. A cubic field will mix 6d, 7d and 5g (e_g, t_{2g}) states into the 5d states. This gives a second order downward shift of the 5d levels. For 6d mixing, for example,

$$\Delta E(t_{2g}) = -|\langle 5d\ (t_{2g})|V|6d\ (t_{2g})\rangle|^2/(E_{6d} - E_{5d}) \quad (20)$$

This shift, however, should only be a few tens of wavenumbers because the energy denominator is on the order of 100,000 wavenumbers, and the matrix element in the numerator is no more than 2000 or 3000 wavenumbers. The

isotropic overlap and correlation crystal field terms will also mix the 5d with 6d and 7d states, again leading to a slight second order downward shift of the 5d energy levels.

A measure of the importance of configuration mixing is the degree to which ion polarizabilities are altered by the crystalline environment. Mahan [21] studied this effect. For anions, the spherically averaged crystal field rises sharply beyond the nearest-neighbor distance. This compresses the potential, which increases the energies of excited anion configurations and reduces the amount of admixing between configurations. For cations, the overlap with negative ligands expands rather than contracts the potential, which lowers the energies of excited configurations and admixes them more. Mahan calculated cation and anion polarizabilities in alkali halides, and compared the results to experimental values. He found that while the polarizabilities of anions decrease significantly from free ion values, the cations show no significant increase.

2.6 The Stokes Shift and Vibronic Interactions

In order to predict trends in the Stokes shift of impurity ion spectra, an understanding of the role of lattice relaxation is needed. The potential energy used to solve for nuclear motions in a solid is the adiabatic

potential of Born and Oppenheimer, derived as follows.

Consider a solid with the collective coordinates of the electrons of interest given by x and the collective nuclear coordinates given by Q. The basic assumption is that the nuclei "feel" only the average field exerted on them by the electronic charge cloud. That is, the nuclear wavefunction should not depend explicitly on electron coordinates, but should depend on the electronic quantum numbers. (The Jahn-Teller effect, described later in this section, represents a breakdown of this approximation.) So we write the wavefunction of the solid as follows.

$$\Psi_{ni} = \psi_n(x,Q)\chi_i^n(Q) \tag{21}$$

ψ_n is the electronic wavefunction, which depends parametrically on the nuclear coordinate Q, and χ_i^n is the vibrational wavefunction, indexed by both the vibrational quantum number i, and the electronic quantum number n. The Hamiltonian of the system is

$$H = T_N+T_E+U(x,Q) \tag{22}$$

T_N is the nuclear kinetic energy, T_E is the electron kinetic energy, and U is the potential energy of the solid.

The next approximation usually made is the adiabatic approximation, that the electron "feels" the nuclei in a

quasistatic fashion. The nuclear motion does not induce electronic transitions. This is equivalent to saying that T_N commutes with ψ_n. In this approximation the electronic Schroedinger equation becomes

$$[T_E+U(x,Q)]\psi_n(x,Q) = \epsilon_n(Q)\psi_n(x,Q) \qquad (23)$$

The wavefunction deforms quasistatically as the lattice moves. Bear in mind that $U(x,Q)$ contains internuclear repulsion terms that depend only on Q, and these terms also appear in the electronic eigenvalue $\epsilon_n(Q)$. The Schroedinger equation for the nuclei becomes

$$[T_N+\epsilon_n(Q)]\chi_i^n(Q) = E_{ni}\chi_i^n(Q) \qquad (24)$$

where E_{ni} is the total energy of the solid.

The important result is that the electronic eigenvalue reappears in the nuclear Schroedinger equation as a potential energy function. Let us now predict the Stokes shift, assuming that the local lattice relaxation principally involves a symmetric breathing motion of the nearest neighbors, as should be the case in the absence of Jahn-Teller effects. We will also take a semiclassical approach to the problem by assuming that the lattice remains stationary during the electronic transitions. The electronic quantum number n now refers to the cerium 4f or 5d electron.

$\epsilon_n(Q)$ can be separated into a crystal field energy of

the electronic state, E(n), and a parabolic potential $(1/2)kQ^2$ for the breathing mode coordinate Q. k is a background spring constant for the mode, which arises from Madelung energies, Van der Waals attractions and overlap repulsions between the closed shells of the ions. That is, k arises solely from interactions which are not a function of the electronic quantum number n. E(n), the crystal field energy, arises only from interactions which are sensitive to the electronic quantum number n.

Figure 7a shows qualitatively the expected dependence of E(4f), $E(5d,t_{2g})$, and $E(5d,e_g)$ on the breathing mode coordinate (or, equivalently, the Ce-F bond distance) Q. The 4f crystal field interaction is relatively weak, so in Figure 7a, E(4f) is a constant. The 5d levels display a crystal field splitting which increases as the bond distance decreases, and a centroid which decreases at first and then increases again as the bond distance decreases. The initial dropping of the centroid is due to the self-induced dipolar interaction (Equation 15), and the centroid rise at shorter ranges arises from antibonding and exclusion effects. The equilibrium mode coordinate in the ground state is Q=0. When the ion is excited into the t_{2g} state, a force $dE(t_{2g})/dQ$ is exerted on the ligands, and the ligands move until the force is counterbalanced by the background spring constant of the lattice. If Q=0 lies to the left of the t_{2g} minimum in the figure, the bonds stretch; if Q=0 is to the

right of the minimum the bonds compress. The Stokes shift is the change in $E(t_{2g})$ resulting from the shift in Q from 0 to the new value Q_e.

The value of Q_e in Figure 7a is determined by force balance.

$$dE_{LATTICE}/dQ = -dE(t_{2g})/dQ \qquad (25)$$

If we assume that the change in Q is small the Stokes shift is

$$S = [dE(t_{2g})/dQ]^2/k \qquad (26)$$

The standard configurational coordinate diagram for this problem, shown in Figure 7b, is obtained by taking a small portion of Figure 7a in the vicinity of Q=0 and adding the background parabola to all the curves. For the 5d states, this leads to a shifted parabola with a different curvature if the 5d curves of Figure 7a are expanded to second order in Q.

Does (26) enable us to predict a qualitative pattern of the variation of Stokes shift with site size when the site symmetry and ligand species is fixed? Blasse [22] makes such a prediction, based on the following reasoning. An absorption to the lowest 5d parabola excites the dopant ion into a state whose wavefunction lobes avoid the negatively charged ligands. The ligands see a more positive effective

charge on the dopant ion and are attracted toward it. If the dopant ion was squeezed into a small site, it is energetically very favorable for the ligands to move inward, and this leads to a large Stokes shift. If the dopant ion was put in a large site, the ligands have already moved in, and further inward movement should be energetically unfavorable, which leads to a small Stokes shift.

On purely theoretical grounds, it is easy to find fault with the Blasse hypothesis, even if a single breathing mode can be assumed to play the dominant role. First, Blasse ignores covalency forces. The antibonding nature of the 5d orbitals would repel rather than attract the ligands. Second, he regards the Stokes shift as being determined by how far the ligands move, and ignores the issue of how sensitive the electronic energy is to this motion. If the model depicted in Figure 7b is correct, Equation 26 predicts a Stokes shift of zero for a site size at the minimum of the $E(t_{2g})$ curve. To date there is no comprehensive theory that enables us to predict Stokes shifts based on simple qualitative arguments such as the Blasse hypothesis. Indeed, rigorous calculations or experimental observation of many systems may show that even the qualitative trends displayed by the Stokes shift are sensitive to the actual values of many physical parameters.

So far we have assumed that the system in the excited state is stable with respect to asymmetric distortions, or at least that the "spring constants" resisting such distor-

tions are so great that the distortions have a negligible effect. The e_g and t_{2g} levels are both degenerate, and the Jahn-Teller theorem states that certain modes of distortion give rise to a first-order splitting of the degeneracy which is linear in the mode coordinates. Therefore, when the state becomes occupied, nonzero forces arise and distort the system into a lower symmetry configuration until all the degeneracy is removed. With the exception of Kramers doublets, where the symmetry is in time rather than space, degenerate electronic states in molecules and solids are unstable. The following survey of theoretical and experimental aspects of Jahn-Teller interactions follows Englman [23] and Bersucker [24,25].

Group theory limits the symmetry of the modes which cause this effect. For the e_g level, only vibrations transforming as e_g are Jahn-Teller-active, and for the t_{2g} level, both e_g and t_{2g} modes are Jahn-Teller active.

From a theoretical standpoint, the first consequence of this is that the adiabatic wavefunction (21) is no longer adequate because small displacements in the JT-active mode strongly and non-adiabatically admix the electronic states. In fact, the matrix elements of the linear vibronic interaction become singular when the basis of (21) is used. It is better to expand the wavefunction in electronic eigenfunctions which solve the Schroedinger equation at Q=0.

$$\Psi_n(x,Q) = \Sigma\, \chi_k^n(Q)\phi_k(x) \tag{27}$$

where

$$[T_E + U(x,0)]\phi_k = \epsilon_k\phi_k \tag{28}$$

We separate the potential,

$$U(x,Q) = U(x,0) + V(x,Q) \tag{29}$$

and define the electronic matrix elements of V.

$$V_{km}(Q) = \langle\phi_k|V|\phi_m\rangle \tag{30}$$

This leads to coupled equations for nuclear motion.

$$[T_N + \epsilon_k + V_{kk}(Q) - E_k^n]\chi_k^n(Q) + \Sigma V_{km}(Q)\chi_m^n(Q) = 0 \tag{31}$$

For widely separated nondegenerate electronic states, the first term dominates, and the adiabatic approximation is valid.

The vibronic interaction V is usually expanded in normal coordinates.

$$V = \Sigma\, (dV/dQ_i)_0 Q_i + (1/2)\Sigma\, (d^2V/dQ_i dQ_j)_0 Q_i Q_j + \ldots \tag{32}$$

The leading two terms are the linear and quadratic vibronic interactions, respectively.

Although in the case of electronic degeneracy, we

cannot describe the motion of the system adiabatically, it is of interest to solve for the electronic energies at fixed values of Q in the space of the JT-active modes. These functions $E_k(Q)$ are termed the adiabatic potentials or adiabatic surfaces, and are solved by deleting T_N from (31) and solving the resulting secular equation. Only terms with JT-active symmetries in (32) contribute to off-diagonal matrix elements V_{km} in (31). The diagonal elements V_{kk} come both from JT terms and from totally symmetric quadratic terms. The latter give rise to a background force constant for the JT mode. So for a particular JT mode with symmetry Γ the adiabatic potential is written

$$E_k(Q) = (1/2)K\Sigma Q_i^2 + E'_k(Q) \qquad (33)$$

where i is the partner label for the vibrational mode, k is the electronic partner label, K is the background force constant, and E' includes linear, quadratic and higher order JT splittings. If there is more than one JT mode, their background paraboloids are just summed and E' is determined from a matrix which includes coupling terms arising from all the partners of all the JT modes.

For O_h symmetry the two problems of interest are E-e and $T-(e+t_2)$. (In this notation, the capital letter indicates the symmetry of the degenerate electronic term, and the lower case letters indicate the symmetry of the

JT-active vibrations.) In the E-e problem, there are two surfaces in the two dimensional space of the e modes. If only linear coupling is included these surfaces form the "Mexican hat" shape, shown in Figure 8. The upper (+) and lower (-) surfaces meet at a single branch point at the point of degeneracy.

If the linear coupling is strong enough to render the circular trough in the bottom surface many vibrational quanta deep, the motion of the system for low lying states is approximately adiabatic; it undergoes simple harmonic radial oscillation and slow angular rotation in Q space. In real space, this corresponds to a rapidly oscillating tetragonal distortion wave whose orientation gradually rotates from z to y to x, and back to z again. Thus even the so-called "static" Jahn-Teller effect (the term for a deep distortion well) does not necessarily imply static distortion with slight zero-point motions.

The addition of the quadratic interaction produces three wells in the bottom of the trough 120 degrees apart, corresponding to tetragonal distortions along the x, y, and z directions. If the barrier between the wells is small compared to the vibrational quantum of energy, the motion is similar to the pure linear case, except that the rotation is hindered - more time is spent in the wells, with more rapid well-to-well rotation. For stronger quadratic coupling, the wells become separated by barriers which exceed the vibrational quantum. In this case there is well-to-well

tunneling, producing a pulsating pattern of tetragonal distortion waves.

The linear T-e problem is particularly simple because the off-diagonal matrix elements V_{km} vanish by symmetry. The adiabatic surfaces are three separate paraboloids with respective minima at the x-, y-, and z-directed tetragonal distortions. Each electronic wavefunction (|xy>, |xz>, and |yz>) has its own paraboloid; the wavefunctions are not mixed by the distortion. As long as there is no quadratic or higher order coupling the the eigenstates of the system are:

$$\begin{aligned} &\phi_{xz}\chi_y \\ &\phi_{xy}\chi_z \\ &\phi_{yz}\chi_x \end{aligned} \qquad (34)$$

where the ϕ's are the partners of the T representation, and χ_i is a simple harmonic oscillator wave function centered around the i^{th} tetragonal distortion. The system will not tunnel between the paraboloids because the above states are eigenstates.

The linear T-t_2 problem has only off-diagonal matrix elements (aside from the background paraboloid). The adiabatic surfaces have minima at the four equivalent trigonal (111) distortions. If the minima are deep, the vibronic mixing will cause the system to tunnel among them,

producing a pulsating pattern of trigonal deformations.

Simultaneous linear interaction of a T state with both e and t_2 vibrations is a complex problem. Depending on the sizes of the vibronic coupling constants, the adiabatic surfaces can have tetragonal, trigonal, and/or orthorhombic minima.

The "pseudo-Jahn-Teller effect" [23] is also potentially important. This is the vibronic mixing of two electronic states separated by an energy gap. It generally leads to a "softening" of the lower surface and "hardening" of the upper one with respect to displacements in the mode responsible for the mixing. If this effect is strong enough, the curvature of the lower surface can become negative, leading to dynamic instability. For example, the t_{2g} level of Ce^{3+} splits into a Γ_7 and a Γ_8 level because of the spin-orbit interaction. e and t vibrational modes can admix these two states, softening the lower surfaces (the Γ_8) and hardening the upper ones (the Γ_7). The spin-orbit splitting is only a few hundred wavenumbers, so this effect would occur for vibronic coupling constants of a similar magnitude.

We now turn to the experimental manifestations of the Jahn-Teller effect. In the ground state, a JT interaction will cause "static" or "dynamic" distortion. In compounds where the Jahn-Teller ion is a major component, cooperative Jahn-Teller effects can drive structural transitions in the material. Even if the JT ion is a dopant, a ground state JT effect lends itself to low level measurements such as ESR,

NMR, infrared and Raman spectra. The lanthanide rare earths have extremely weak vibronic coupling because of the well-shielded nature of the 4f states. In particular, Ce^{3+} in octahedral coordination has a Kramers doublet Γ_7 ground state. Therefore, the ground state JT interaction is of no concern to us here.

The 5d configuration of Ce^{3+} and other rare earths are short lived excited states well out of reach of the low level measurements mentioned above. It primarily through optical spectra in the blue and near uv regions that JT effects can be investigated, and they manifest themselves in several ways:

1. Progressions and splittings in the vibronic fine structure of low-temperature absorption spectra due to JT interactions.

2. The appearance of multihumped envelopes in low-resolution, high-temperature optical spectra.

3. Vibronic reduction of the spin-orbit splittings (which is an example of a general phenomenon called the Ham [26] effect).

4. "Polarization memory" - a correlation between the polarization of the fluorescence and the polarization of the exciting light. This is due to different selection rules for excitation of the

different minima of the adiabatic surfaces.

5. Anomalously broad emission bands (compared to the absorption bands) due to vibronic mode softening in the excited state.

Struck and Herzfeld [27] performed low-temperature absorption measurements on Ce^{3+}-doped CaF_2 (cubal coordination) and fitted the vibronic fine structure to a numerical solution of the vibronic energy levels of the linear E-e problem. However, the intensities of the vibronic lines are not consistent with the assumption that quadratic and higher-order interactions are negligible. A more fundamental problem is the likelihood of nearby charge compensators in the crystal producing extra lines.

Kaplyanskii and Przhevuskii [28,29] observed splittings of the zero-phonon lines in the absorption spectra of Eu^{2+} and Sm^{2+} in CaF_2 and SrF_2. Chase [30] later ascribed these splittings to tunneling among the tetragonal minima of the E-e problem.

The shape of the envelope of the absorption band from a singlet A state to a JT E-e state, calculated semiclassically, is a symmetrical double-humped structure centered around the electronic energy difference at Q=0 in the e space. The dip between the humps goes to zero in the absence of interaction with symmetric modes, and fills in as this interaction increases. Quantum mechanical calculations

predict asymmetrical double-humped shapes. For very strong linear interaction the high energy hump splits into several narrower humps due to the appearance of quasi-vibrational states in the steep upper well of the "Mexican hat." However, this only begins to happen for improbably large values of the coupling strength.

For A to T-e absorption the band displays no splitting. The displacement of the paraboloids simply contributes to the width of a Gaussian band in the same manner as for symmetrical vibrations.

For A to T-t absorption, the semiclassical bandshape is a symmetrical triple-peaked structure, the middle peak being much sharper because it arises from a singularity in the joint density of states at Q=0. Again, quantum mechanical calculations predict asymmetrical shapes.

From the point of view of broadband absorption spectra from a non-JT ground state, a linear JT coupling in the excited state is a splitting and broadening mechanism. The integrated absorption cross section and the center of gravity of the band is unaffected by it [31] (assuming we can neglect vibronic mixing with other electronic states, which is not the case for forbidden transitions). Furthermore, the symmetric and JT-active modes give additive contributions to the second moment (the width) of the spectrum.

From the viewpoint of emission spectroscopy, the

Jahn-Teller stabilization energy makes a direct contribution to the Stokes shift. The semiclassical expression for this contribution is of the same form as (26), except that Q is a JT coordinate pointing in the direction of a minimum, and k is the background spring constant for the JT mode.

The Ham [26] effect is a reduction of matrix elements of purely electronic operators by Jahn-Teller interactions. It arises because the electronic matrix elements are multiplied by vibrational overlap integrals, which are less than unity when JT effects are operative. As long as the matrix elements pertain only to the lowest vibronic state, and the operator does not involve nuclear coordinates, the vibronic reduction factor depends only on the symmetries of the state and of the operator, not on their specific natures.

Ham effect reduction is a drastic effect, generally displaying an exponential dependence on the JT stabilization energy (e.g., the trough depth in Figure 8). For example, in the T-e problem, spin-orbit splitting is reduced by the factor $\exp(-3E_{JT}/2h\omega_E)$, and a similar expression is approximately valid in the T-t case.

"Polarization memory" was observed by Kaplyanskii et. al. [32] in Yb^{2+}-doped CaF_2 at low temperatures. They excited the sample with light polarized along the [001] direction and propagating along the [100] direction, and they observed the fluorescence in the [010] direction. They found that the [001]-polarized fluorescence was 38% more

intense than the [001]-polarized fluorescence. [111]-polarized excitation gave rise to unpolarized fluorescence. This is consistent with the three tetragonal minima expected in an e-mode Jahn-Teller problem.

Payne, Goldberg, and McClure [33] cite evidence for t_{1u} mode softening in the excited configuration of Cu^+ in NaF. In the fine structure of the $(3d^{10})\ ^1A_{1g}$ to $(3d^9 4s)\ ^1T_{2g}$ absorption spectrum, they observed a 36 cm^{-1} vibrational progression which they assigned to a t_{1u} mode on the basis of intensity ratios. The t_{1u} frequency for the ground state was determined from the temperature dependence of the total 3d to 4s oscillator strength, based on the assumption that this is a t_{1u}-assisted transition with 4p as an intermediate state. The frequency obtained was 200 cm^{-1}. Thus the excited state mode softening factor is greater than 5, assuming that the assignments are correct. The mode softening was ascribed to vibronic 4s-4p mixing.

There is no evidence of anomalously broad emission, however [34]. The emitting state in this system is a ^3E_g lying 10000 cm^{-1} below the singlet states, and may not be susceptible to t_{1u} mode softening.

Ce^{3+}, however, displays allowed transitions, and therefore any mode softening in the emitting 5d states should increase the emission bandwidth.

2.7 Summary

In this chapter we have explored the crystal field interactions which determine the rare earth 5d energy levels in octahedral symmetry, as revealed by band positions in an absorption measurement. Electrostatic interactions dominate for distant (non-overlapping) ligands and give inverse power law splittings and centroid shifts. At closer ranges, overlap and covalency contributions become important. These are "repulsive" interactions and vary roughly exponentially with the ligand distance. Thus by looking at band centroids in absorption and viewing JT interactions as a broadening mechanism, one can find the values of the splitting and centroid shift appropriate to the equilibrium position of the lattice.

In emission the symmetrical and JT-active modes should give additive contributions to the Stokes shift. A "universal pattern" of host-to-host variation in the Stokes shift is difficult to predict based on qualitative arguments; the vibronic coupling may be greater in a "tighter" site, but so may be the background spring constant which resists distortion. The outcome of this competition is highly dependent on the parameters of the case at hand, and generalizations should be based on the observation of many cases or on careful and detailed calculations.

The Jahn-Teller effect on the excited 5d state leaves

several clues for the optical spectroscopist. It should lead to reduction of the spin-orbit splitting, correlation between the polarization of the exciting and emitted light, distinctive multihumped bandshapes, and, in the case of appreciable mode softening, anomalously broad emission bands. For allowed transitions, the pseudo-JT coupling will not change the total band intensities appreciably, whereas forbidden transitions depend entirely on this coupling to steal their intensity from allowed transitions.

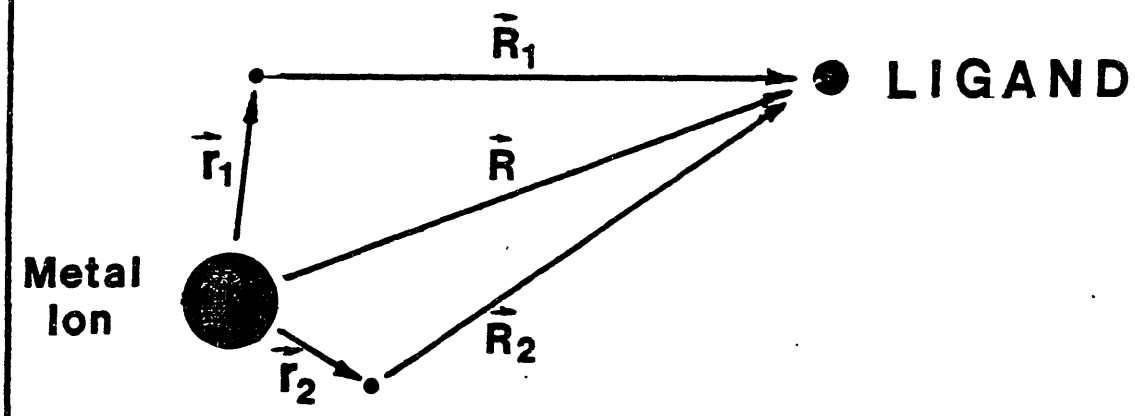

FIGURE 6 NOTATION FOR THE ANALYSIS OF CORRELATION CRYSTAL FIELD

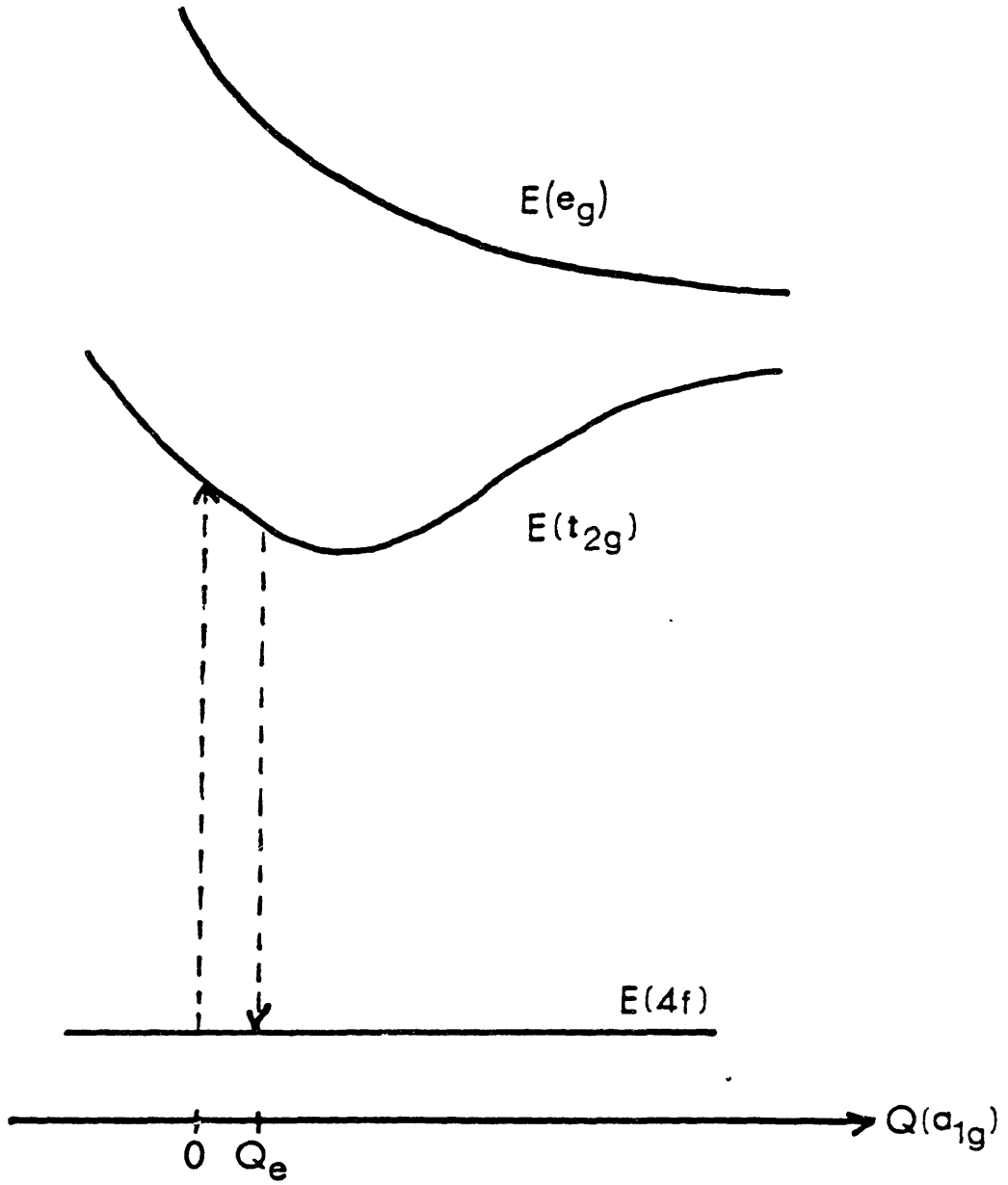

Figure 7a Ce^{3+} 4f and 5d crystal field energies as a function of bond distance Q

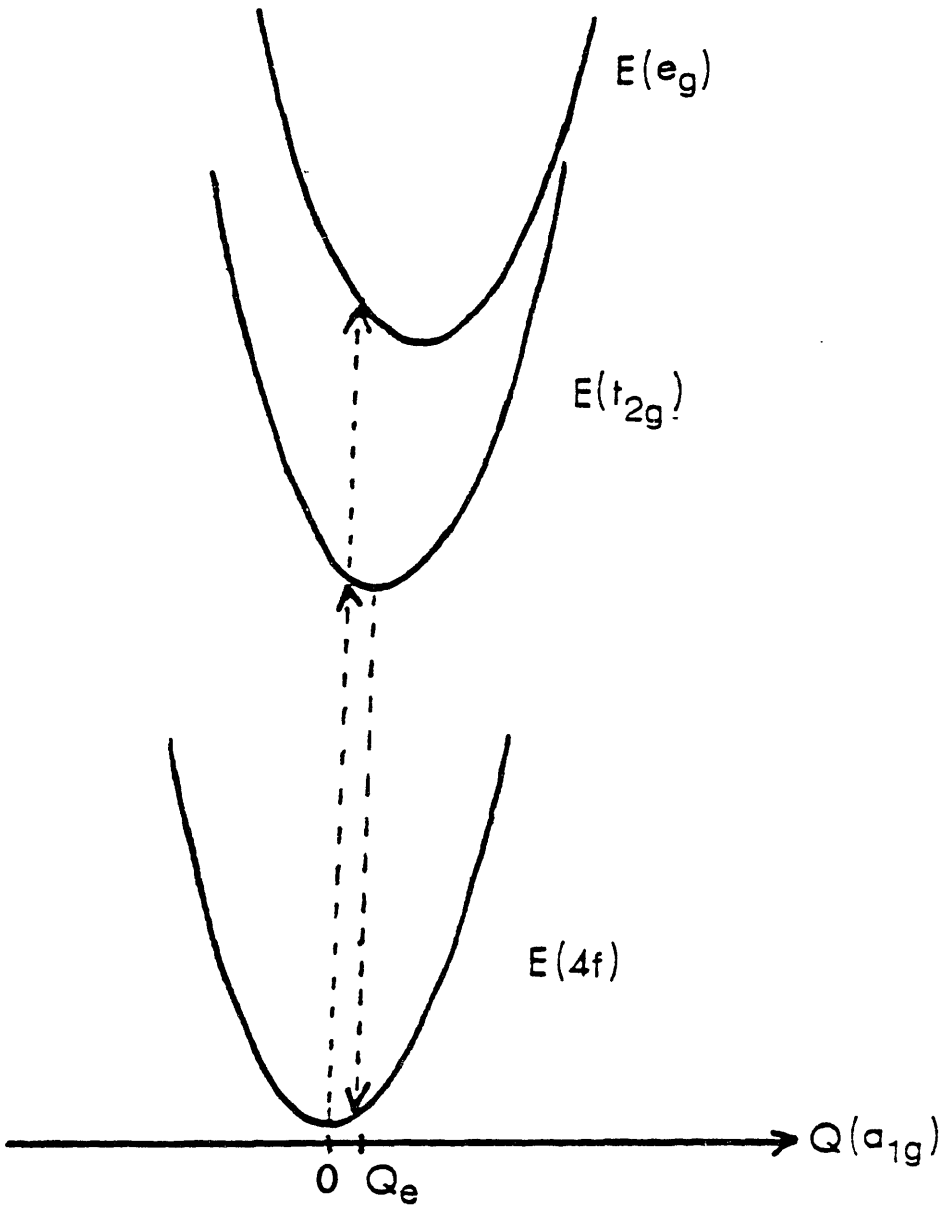

Figure 7b Configurational Coordinate Diagram for Ce^{3+} in Octahedral Symmetry

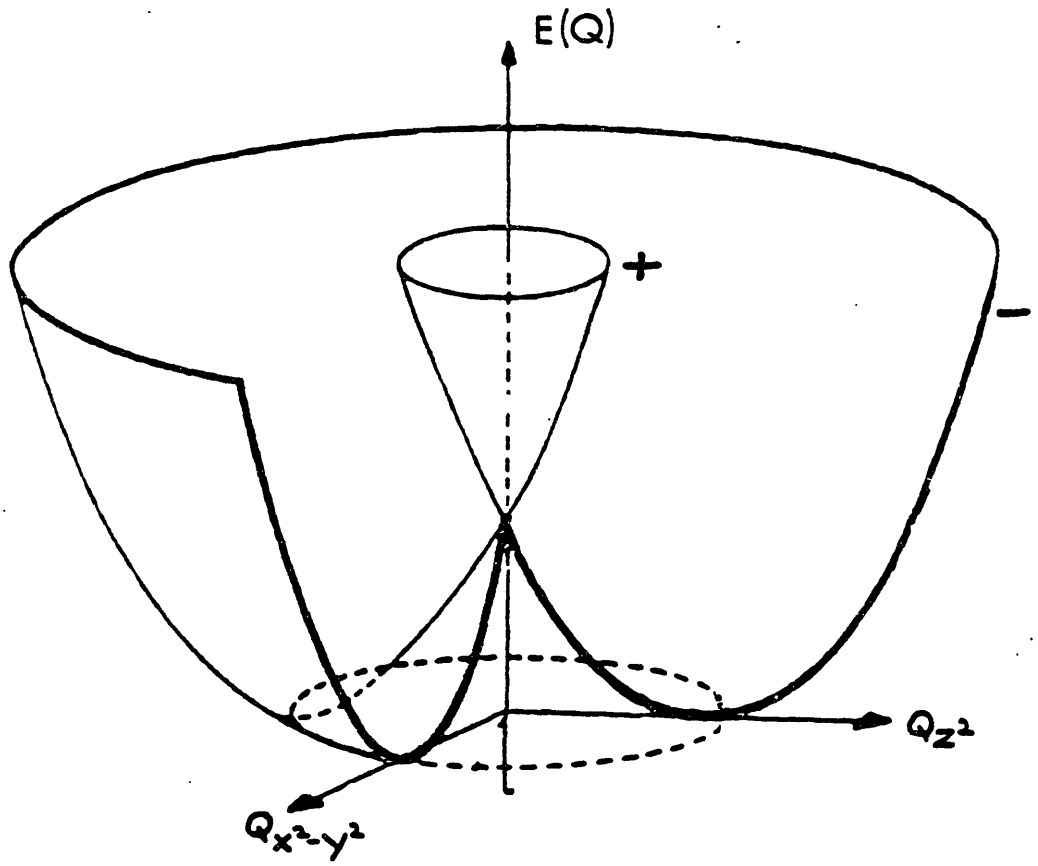

Figure 8 Adiabatic Surfaces for the E-e Jahn-Teller Problem

CHAPTER III

CRYSTAL GROWTH AND X-RAY ANALYSIS

3.1 Background and Past Work

The elpasolite lattice belongs to space group Fm3m (O_h^5), and Figure 9 shows one octant of a cubic unit cell of A_2NaRF_6. The Na^+ and R^{3+} ions form a rocksalt lattice, and the A^+ ions sit at all equivalent (1/4, 1/4, 1/4) positions. The F^- ions lie between the Na^+ and the R^{3+} ions at some fractional distance, forming regular octahedra around R^{3+} and slightly larger regular octahedra around Na^+. The Na and R sites have O_h symmetry, the A site has T_d symmetry, and the F site has C_{4v} symmetry.

The first reported synthesis of fluoride elpasolite was by Roy [35], who produced K_2NaAlF_6 in 1954 by melting and recooling intimate mixtures of fluorides.

In 1957, Wurm et. al. [36] produced K_2NaTiF_6 by electrolysis of K_2TiF_6 and Na_2TiF_6 in a molten bath of KCl and NaCl. The intention was to produce Ti metal; the result was dendritic growth of Ti metal on the cathode, embedded in a ball of a deep violet salt which was identified as K_2NaTiF_6. The cubic structure and optical isotropy of the material (as contrasted to K_3TiF_6 and Na_3TiF_6) were later

[37] cited as evidence that K_2NaTiF_6 is not a continuous K-Na solid solution between the end members K_3TiF_6 and Na_3TiF_6.

Knox and Mitchell [38] prepared K_2NaGaF_6, K_2NaCrF_6, and K_2NaFeF_6, in 1961 by adding the trivalent fluorides to molten KHF_2 and $NaHF_2$ in a Pt crucible over an open flame.

In 1966, Garton and Wanklyn [39] grew small crystallites of K_2NaCrF_6, and Cs_2KCrF_6 by melting and slow cooling of the fluorides in a PbF_2 flux and then dissolving the flux in water. K_2NaAlF_6 was prepared by the same method using KCl, NaCl flux, and Rb_2KGaF_6 using a RbCl, KCl flux and using a PbF_2 flux.

In 1968, Aleonard and Pouzet [40] prepared powders of Rb_2NaRF_6 and Cs_2NaRF_6 by subsolidus reaction (R = Yb, Er, Ho, Y, Tb, Sm). They indexed x-ray powder patterns for all the compounds and found the best fit F^- position for the Er compounds.

Nassiff et. al. [41] prepared K_2NaTiF_6 in 1971 by melting and recooling KHF_2, $NaHF_2$, and Ti metal in a crucible over an open flame.

K_2NaScF_6 and K_2NaYF_6 were first prepared by Schneider and Hoppe [42] in 1970 by subsolidus reaction. Siddiqi and Hoppe [43] prepared Cs_2KLnF_6 compounds in the same year by subsolidus reaction (Ln = La through Lu). Hoppe and his coworkers have published much data on the synthesis and properties of such powders.

Rb_2NaScF_6 was first prepared by Chassaing [44] in 1971

by subsolidus reaction.

The first reported growth of large single crystals of fluoride elpasolite was by Guggenheim and coworkers [45] at Bell Labs in 1974. They grew Cs_2KPrF_6, Cs_2NaHoF_6, and Rb_2NaLnF_6 (Ln = Eu, Gd, Tb, Ho, Er, Y, Tm, Yb) by horizontal zone melting a stoichiometric feed in a Pt boat. The molten zone was about 20% of the length of the charge, and a single pass was done at 3-5 mm/hour. The resulting ingots consisted of a clear single crystal midsection with mixed phase regions at either end, each section comprising about one third of the total length.

Merchandt et. al. [46] in 1980 prepared Rb_2KNdF_6 and Cs_2KNdF_6 by subsolidus reaction, and then grew single crystals of the latter compound in a sealed Pt crucible by the Bridgman technique. The material was extremely hygroscopic; the polishing of the crystals had to be done in a dry box.

There are two properties reported for some fluoride elpasolites which are of potential concern in this work. First, a subtle structural phase transition can occur at low temperatures. Veenendaal et. al. [47] reported that Rb_2NaHoF_6 undergoes a transition at 172 K involving a 5 degree rotation and a slight tetragonal compression of the fluorine octahedra.

Second, solid solutions are possible. Babaeva and Bukhalova [48] do not acknowledge K_2NaScF_6 as a compound,

but show a continuous solid solution in the binary system K_3ScF_6-Na_3ScF_6. Vedrine et. al. [49] prepared powders of A_2BYF_6 (A = Cs, Rb, K; B = Rb, K, Na) by subsolidus reaction, from materials with excess A or with excess B. The density and lattice constant were measured and the lattice constant plotted as a function of the fractional excess of the cation. A nonzero slope was ascribed to solid solution, i.e., excess B "spills over" into the A site and the lattice contracts, or excess A "spills over" into the B site and the lattice expands. They found that the larger alkali metals (Cs, Rb, K) form solid solution quite readily, but whenever B = Na, solid solution did not occur. It is important to remember that crystallization from the melt might have yielded different results.

K_2NaTiF_6 structural studies bear some examination because the ground state of Ti^{3+} in octahedral symmetry is a 3d t_{2g} state, very similar to the emitting state of Ce^{3+}. Reported studies might give clues as to how large the Jahn-Teller coupling is for octahedral fluoride complexes. Bright and Wurm [37] claim cubic symmetry for K_2NaTiF_6 on the basis of x-ray powder patterns. Later ^{19}F NMR and magnetic susceptibility measurements were done by Burkert et. al. [50], who claim a tetragonal compression of the TiF_6 octahedra due to the Jahn-Teller effect. (The x-ray data does not conflict with this, however, because if the distortion is dynamic, the long time constant associated

with the x-ray measurement would reveal cubic symmetry on a "time averaged" basis. In this case one would see cubic reflections in the powder pattern, though the intensities would be altered.)

Trustworthy phase diagrams of the fluoride elpasolites are nonexistent. Babaeva and Bukhalova [48] show K_2NaScF_6 as simply a point in a phase field of continuous K-Na solid solution. The same authors [51] show K_3YF_6 as the only intermediate compound in the $KF-NaF-YF_3$ system; they show it as congruently melting, and show no structural transitions. Richter and Pistorius [52] claim that K_3YF_6 is polymorphic, undergoing transitions at 825 C, 410 C and 290 C. A binary phase diagram of the $NaF-YF_3$ system by Thoma et. al. [53] shows many regions of Na^+-Y^{3+} disordering, whereas they do not report Na^+-Sc^{3+} disordering in the $NaF-ScF_3$ system [54]; rather, they show Na_3ScF_6 as a congruently melting compound which undergoes a structural phase transition as 680 C. Similarly, Rb_3YF_6 is shown as a congruently melting compound by Chassaing [55], which undergoes a transition from a high temperature cubic form to lower symmetry at 161 C. Babaeva and Bukhalova [56] show Rb_3ScF_6 and K_3ScF_6 as congruently melting compounds with no structural transitions.

3.2 Crystal Growth Facilities

Crystal growth of elpasolites at the Crystal Physics Laboratory has been carried out by the Czochralski method and by the vertical Bridgman method. In both cases commercial grade oxides and carbonates are first converted to fluorides by reaction with gaseous HF. Figure 10 shows the system used for this processing step. The charge is placed in a platinum boat supported in a graphite hemicylinder. This in turn is placed in a Pt-Rh process tube which is sealed at the ends with Teflon-lined brass endcaps. The tube is heated in a three-zone furnace with separately controllable silicon carbide heating elements. The controller ramps the temperature at 300 ^{o}C per hour so as not to crack the alumina cylinder which houses the process tube. Typically, argon is flowed through the process tube until 300 ^{o}C is reached, at which point the temperature ramping is halted and HF is flowed through the tube for 1 to 2 hours, and reacts with the solid charge. This converts oxides and carbonates to fluorides, releasing water and CO_2 which pass out of the tube. The temperature is then ramped up to a setpoint above the melting point and maintained for three to four hours, so that the reaction can be completed with molten material. Finally the temperature is ramped back down, and the argon flow is resumed once the charge has resolidified.

Figure 11 shows the furnace used for Czochralski

growth, designed by Dr. David Gabbe. It consists of a water-cooled stainless steel chamber evacuated by an oil diffusion pump. The water-cooled seed rod, made of stainless steel, is introduced through the top of the furnace through a double o-ring gland with guard vacuum; this allows for leak-free rotation and translation. The upper and lower portions of the chamber can be separated by an isolation valve and separately evacuated. This allows for multiple growth runs from the same melt without exposing the melt to the atmosphere. The feed is placed in a platinum crucible which rests on a graphite support, and is heated by a graphite ohmic heating element with a "picket fence" design. The power is delivered through feedthroughs on the bottom plate of the chamber. Molybdenum sheet is used to construct heat shielding around and above the heating element. A thermocouple fed through the bottom plate measures the temperature directly underneath the crucible.

The diffusion pump is able to evacuate the furnace to pressures below 10^{-4} Pa, allowing the system to be outgassed and then back filled with argon (or argon with hydrogen if a reducing atmosphere is desired). In the absence of a seed crystal, nucleation is started on a twisted platinum wire attached to the end of the seed rod. During growth, a typical pulling rate is 1 mm/hour, and a typical temperature lowering rate is 3 ^{o}C/hour. The seed rod is rotated at a rate of about 15 rpm. Temperature control is achieved using a Barber-Colman three-term controller.

The Bridgman furnace, designed by Dr. Arthur Linz, consists of an r.f. coil driven by a Lepel Hartley oscillator operating at 450 kHz. The coil is enclosed in a water-cooled stainless steel chamber, which is evacuated by a mechanical pump through a mesh trap. Figure 12 shows the components in the interior of the chamber. A water- or air-cooled stainless steel pedestal is introduced through the bottom plate of the furnace through a double o-ring gland to permit leak-free vertical translation. The graphite crucible rests on the top of the pedestal. A stainless steel support stand fixed to the bottom plate supports a cylindrical graphite susceptor and quartz tube. The susceptor absorbs the r.f. power and distributes the heat, and also is intended to prevent large changes in the oscillator load impedance as the crucible is lowered during growth. A molybdenum heat shield is fixed to the inside of the quartz tube using smaller diameter quartz rings. There is a vertical gap in the heat shield to avoid short circuiting the r.f. field, and pyrometric measurements of the susceptor temperature are made through the gap.

The graphite crucible is a 1-inch diameter cylindrical tube whose inner walls are slightly tapered to facilitate removal of the crystal from the top. A narrow weep hole connects the bottom of the interior chamber of the crucible to the exterior surface where contact with the cooled pedestal is made. When the feed is loaded, the top of the

crucible is sealed with a graphite cap and gasket. The feed is then outgassed through the weep hole by pumping at a temperature about two hundred degrees below the melting point. The furnace is then back filled with argon (or argon-hydrogen) and the r.f. power is increased until the charge melts and flows down into the weep hole, freezing it shut. In this way, a closed system is formed which minimizes contamination of the melt. With the r.f. voltage held constant the crucible is lowered (typically at 1 mm/hour) into the cooler regions of the chamber, causing crystallization of the melt from the weep hole up. Thus the weep hole also serves as a site for initial nucleation.

Care must be taken to polish the interior of the crucible to prevent spurious nucleation there. This is accomplished by constructing a large cotton swab which fits tightly in the interior of the crucible when damp. 3 μm alumina grit is sprinkled on the swab and then the swab is spun within the crucible using a drill press.

Not shown in Figure 12 are the thermocouple wells, two 0.144 inch holes drilled into the walls of the crucible. The depths are such that one thermocouple can be mounted close to the lower portion of the charge, and another one can be mounted close to the upper portion of the weep hole. The temperature difference between the upper and lower thermocouples facilitates estimation of the axial temperature gradient so that the proper setpoint can be established. Too little r.f. power results in incomplete

melting of the charge; too much causes the melt to completely drain out through the weep hole. In principle, the melting point can be judged by observing a thermal arrest in the upper thermocouple as the r.f. power is initially increased. In practice, the setpoint was established by previous experience with identical or similar feed materials, as the thermal arrest was seldom sharp enough to be located with certainty.

Early Bridgman runs employed a crucible with a finned structure on the lower portion (shown in the figure), to reduce the cooling from the pedestal. Later runs employed a crucible without the fins and with a longer weep hole. The design modification (explained later) was incorporated to improve the interface shape and try to eliminate constitutional supercooling, which was suspected to be a problem.

3.3 Early Work by Gabbe

The earliest crystal growth experiments on the fluoride elpasolites in the Crystal Physics Laboratory were Czochralski runs done by Dr. David Gabbe.

Three boules of Cr-doped K_2NaAlF_6 were grown; the first two from stoichiometric feed, and the last one from a Na-enriched feed. The resulting crystals contained bubbles and other inclusions. The runs were discontinued because

evaporation of AlF_3 fogged the furnace windows and interfered with visibility.

Several specimens of K_2NaScF_6 were then grown. First, a stoichiometric feed with 1% Cr was prepared. (Doping levels are always specified in molar % with respect to the substituted ion, in this case 1 mole of Cr for every 99 moles of Sc.) An initial growth run was done in a zone refiner in a single pass. The resulting material was entirely clear, though cracked. An x-ray powder pattern showed that it was elpasolite.

Another stoichiometric melt was prepared with 2.5% Cr and a Czochralski run was done using a Pt wire to start nucleation. Throughout the run, radiation from Cr^{3+} obscured visibility of the crystal, the melt, and the interface. After about three days, this was compounded by fogging of the furnace windows due to evaporation. The run was discontinued and two subsequent crystals grown from the remaining melt. Both crystals cracked upon cooling. The first contained a second phase precipitate at the top which thinned out along the length. The second was substantially clear with some inclusions.

An undoped stoichiometric melt was then prepared and two K_2NaScF_6 crystals grown from it. The final result was similar, but improved visibility made it apparent that the precipitate formed during cooling to room temperature; the boule was clear during growth.

A third feed was prepared doped with 2.5% Cr. This feed was Na-enriched (31% molar NaF, 47% molar KF, and 22% molar ScF_3). The first crystal pulled from the melt was entirely clear with less cracking than had occurred before. A seed crystal was obtained from the bottom of this boule, and used to grow a second boule from the remaining melt. Cracking was even less, and was limited to the surface, although cracks developed during subsequent cutting and polishing.

X-ray fluorescence was measured on the crucible residues from these three K_2NaScF_6 feeds using the scanning electron microscope. Samples from the undoped set of Czochralski-grown boules were cut from the top, middle and bottom portions and chemically analyzed by atomic absorption spectroscopy. A sample of the undoped crucible residue was also analyzed. The results indicate that Na concentration increases and K concentration decreases along the boule from top to bottom, with Sc concentration remaining constant at the stoichiometric concentration. The crucible residues were enriched in Sc and depleted in K. Gabbe tentatively interprets these results as indicating growth of a solid solution $K_{2-x}Na_{1+x}ScF_6$, and ascribes the Sc enrichment of the melt to the fact that K and Na evaporate from the melt more rapidly than Sc, and subsequent crystallization further enriches the melt in Sc.

X-ray powder patterns show the elpasolite reflections plus, to a varying degree, weak additional reflections which

cannot be indexed on a cubic cell. The crystals, however, were optically homogeneous and showed no birefringence under a polarizing microscope. The first boule grown from the Na-enriched melt was good enough to allow preparation of (100) plates from the top, middle, and bottom portions for x-ray diffraction measurements. Three effects are notable, as shown for the (800) and (400) peaks in Figure 13. First, the diffraction peaks become narrower along the length of the boule from top to bottom. At the bottom the $k\alpha_1$ and $k\alpha_2$ components of the (800) reflection are resolvable. Second, the additional reflections become weaker along the length of the boule, and are undetectable at the bottom. Third, the lattice constant of the elpasolite increases slightly along the top half, and then decreases significantly along the bottom half.

A Cr-doped K_2NaScF_6 boule was grown by the Bridgman method from leftover melt from the zone refiner. The melt composition was unknown but was probably nearly stoichiometric. The boule showed the same behavior as the Czochralski-grown boules: a second phase precipitate thinning out along the length of the boule, with decreasing additional reflections in the x-ray powder pattern.

Rb_2NaScF_6 doped with Ti was grown by the Czochralski method from a Na-enriched melt (47% molar RbF, 31% molar NaF, 21% molar ScF_3, and 1% molar TiF_3). The boule which was pulled from the melt was transparent. The x-ray

diffraction pattern showed only elpasolite reflections, and these were sharper than the reflections observed for the K compound grown from a Na-enriched melt. The boule, however, was small because the windows were obscured by evaporation after about 36 hours, and the run had to be discontinued.

Rb_2NaYF_6 and K_2NaYF_6 doped with Ce were also grown in the Czochralski furnace from stoichiometric melts. Nucleation was started on a Pt wire. These systems show a different behavior from K_2NaScF_6. During growth the material is entirely clear. After about a third of the melt is used up, a faint but sharp boundary appears in the boule, and subsequent crystallization also produces clear material. Upon cooling to room temperature, however, the material above the boundary becomes opaque. The sub-boundary material, which remains clear, is shown by x-ray diffraction to be the elpasolite phase. Also the boule remains mechanically intact at the boundary; the decomposition of the pre-boundary material does not cause cracking. Gabbe interprets this behavior as indicative of a solid solution which becomes multiphase at some intermediate temperature, but which maintains a close crystallographic similarity to the elpasolite phase.

3.4 Czochralski and Bridgman Crystal Growth

Table III summarizes the Czochralski growth runs and Table IV summarizes the Bridgman growth runs of the elpasolites. Rb_2NaYF_6, K_2NaYF_6, and Rb_2NaScF_6 do indeed crystallize in the elpasolite structure. No elpasolite crystallization has been observed in the attempt to grow Rb_2KNdF_6 or Rb_2NaLaF_6, rather very fine mixed-phase boules were obtained and no further attempts were made to investigate those systems. K_2LiLaF_6 grown from a stoichiometric melt has so far resulted in columnar growth of a birefringent phase, with a small portion of cubic precipitate between the columns.

Note that Nd, La, and Er were used as dopants for Rb_2NaYF_6 as well as Ce. This was needed to provide clues in the spectroscopic "detective story" which developed in the Ce-doped elpasolites. (See Chapter IV.)

TABLE III Czochralski Crystal Growth Runs

DATE	RUN NO.	COMPOUND	MELT COMP.	DOPING
7/14/83	449F	Rb_2NaYF_6	Na-enriched	undoped
7/17/83	450F	Rb_2NaYF_6	Na-enriched	0.5 % Ce
5/26/84	472F 473F 474F	K_2NaYF_6	Na-enriched	0.5 % Ce

Melt composition was 47% mol RbF or KF, 31% mol NaF, 22% YF_3

TABLE IV Bridgman Growth Runs of Elpasolites

DATE	RUN NO.	COMPOUND	MELT	DOPING	COOLING, ATM.
11/1/83	1B	Rb_2NaLaF_6	E	0.15% Ce	air, Ar
12/11/83	3B	Rb_2NaScF_6	E	1% Ce	air, Ar
12/19/83	4B	K_2NaYF_6	↓	0.5% Ce	↓
1/12/84	6B	K_2NaYF_6	↓	↓	↓
2/8/84	8B	K_2NaYF_6	S	↓	↓
3/12/84	10B	K_2NaYF_6	E	↓	↓
4/4/84	12B	K_2NaYF_6	〃	↓	↓
4/22/84	13B	Rb_2NaYF_6	E	5% Er	air, Ar
5/8/84	14B	Rb_2NaYF_6	↓	5% Er	↓
6/22/84	15B	Rb_2NaYF_6	↓	5% Nd	↓
6/30/84	16B	Rb_2NaYF_6	↓	1% La	↓
7/14/84	17B	Rb_2NaYF_6	↓	1% Nd	↓
7/21/84	18B	Rb_2NaYF_6	↓	0.5% Ce	air, Fg
8/3/84	19B	Rb_2NaYF_6	↓	1% Nd	water, Ar
8/14/84	20B	Rb_2NaYF_6	↓	0.5% Ce	〃
8/22/84	21B	Rb_2NaYF_6	↓	0.5% Ce	water, Fg
9/7/84	22B	Rb_2NaScF_6	E	2% Ce	↓
10/4/84	24B	Rb_2KNdF_6	S	none	↓
10/10/84	25B	Rb_2NaScF_6	E	2% Ce	↓
11/3/84	26B	K_2LiLaF_6	S	0.5% Ce	↓
11/14/84	27B	K_2LiLaF_6	S	0.5% Ce	↓

E=Na-enriched melt (47 mol% K,Rb, 31 mol% Na, 22 mol% Y,Sc)

S=Stoichiometric melt, Ar=argon, Fg=forming gas (Ar, 5% H_2)

Rb_2NaScF_6

Three Bridgman growth runs of Rb_2NaScF_6 were carried out, runs 3B, 22B, and 25B. The first was doped with 1% Ce, and the latter two with 2% Ce. In all cases the composition of the feed was enriched in sodium with respect to a stoichiometric melt. (See the E composition at the bottom of Table IV.) It was found by Gabbe that this composition increased the extent of the elpasolite phase field in the case of Rb_2NaYF_6. We will refer to this composition as "Na-enriched."

Run 3B was done with the finned crucible, air-cooling to the pedestal, and an argon atmosphere. This was the most successful run. Except for the top cap precipitate, the boule consisted entirely of single crystal material, although the bottom portion displayed some coring, and there were a few cracks.

Run 22B failed to produce single crystalline material because of incomplete melting of the charge.

Run 23B was done with a water-cooled pedestal, the unfinned crucible, and a forming gas atmosphere. The boule displays severe coring and radial cracking, especially in the lower half.

Since there is no mixed phase region at the beginning (bottom) of the Rb_2NaScF_6 boules, this compound may be congruently melting, although a stoichiometric melt was not

tried. The best growth strategy is probably to use a stoichiometric melt and to keep the axial temperature gradients moderate by using air-cooling.

K_2NaYF_6

Five attempts were initially made to grow K_2NaYF_6 by the Bridgman method, doped with 0.5% Ce. These runs were designated 4B, 6B, 8B, 10B, and 12B. A stoichiometric melt was used in run 8B, and Na-enriched melts used for the other runs.

The feed material for run 4B melted prematurely in vacuum during the outgassing procedure. The resulting boule was removed and then reinserted with additional feed to restart the run. The crucible was not recleaned or repolished. The resulting boule had clear polycrystalline material around the periphery, but the core was full of inclusions, giving the boule a milky white appearance.

Run 6B produced a polycrystalline boule with a milky white mixed phase region at the bottom tip. An attempt was made to polish a slice from the midsection with alumina grit and water. Subsequent inspection under a microscope revealed that the material was polycrystalline with a cellular structure, and with a water soluble precipitate around the grains.

For the next run, 8B, several changes were implemented in the procedures. First, the crucible was polished not

only in the main interior chamber, but also in the weep hole using dental floss and around the top of the weep hole using a Q-tip. It was hoped that this would encourage single crystal formation in the early stages of growth. Second, a slower growth rate (0.3 mm/hour rather than the usual 1 mm/hour) was tried, in order to minimize constitutional supercooling, which was a suspected culprit. Finally, a stoichiometric melt was tried.

The resulting boule had a clear region in the bottom tip of about the same size as the milk-colored mixed phase of the previous run. The tip material was shown by x-ray diffraction not to be elpasolite. The body of the boule showed the elpasolite powder pattern and consisted of cracked single crystal with increasing degree of cloudiness along the length from bottom to top, due to an increasing concentration of a precipitate.

In run 10B, the use of the Na-enriched melt was resumed, and a slow growth rate used (0.4 mm/hour). The resulting boule was polycrystalline and had a milky appearance. When it was cut in half lengthwise with a water-lubricated saw, a section of very hygroscopic material revealed itself at the bottom tip, separated from the elpasolite by a sharp boundary. The elpasolite contained white filamentary inclusions. The interface between the two regions is concave, indicating that the growth interface itself may have been concave, which would cause spurious nucleation on the crucible walls. (See Figure 14.)

To test this possibility, several further changes were made for run 12B, designed to increase the axial temperature gradient, and reverse the radial gradient. First, the heat shield was lengthened to cut down radial heat loss. Second, air flow through the pedestal was increased to increase the axial heat removal. Third, the crucible was positioned higher up into the r.f. coil in the hope that this would place the growth interface in a position of radial heat input instead of radial loss. It was hoped that the radial heat input would make the growth interface convex, and that the increased axial heat removal would mitigate the constitutional supercooling problem.

In run 12B the feed was Na-enriched and the pulling rate was about 0.5 mm/hour. The result was very similar to run 10B: polycrystalline elpasolite with inclusions separated from a hygroscopic mixed phase region at the bottom tip. The procedure changes did affect the boundary shape, however. It was convex around the periphery with a deep concave cusp in the center. (See Figure 15.)

This result indicates that crucible wall nucleation is not the problem. The irregular interface shape suggests that kinetic factors are causing radial as well as axial composition gradients during the growth. The best strategy for future attempts at Bridgman growth of K_2NaYF_6 is to use a wider crucible to facilitate convective stirring and to experiment with the melt composition in order to find the

elpasolite phase field. Water cooling of the pedestal should also be tried, but with a thin-walled crucible, so that heat is removed primarily from the melt, not from the crucible walls.

In an attempt to better understand why these Bridgman results were so bad, and also to get some clear material, Czochralski growth of K_2NaYF_6 was attempted. Four separate boules were pulled from a Na-enriched melt doped with 0.5% Ce.

The first was a small sample which was quenched in order to preserve the high-temperature pre-boundary phase. Quenching was attempted by suddenly pulling the crystal to the top of the chamber, and shutting off the power. An x-ray powder pattern was immediately run on the sample, since rapid decomposition was expected. The reflections were diffuse and numerous, and could not be indexed on a cubic cell. Although the sample was clear at first, it is doubtful that the high temperature phase was successfully preserved. Over the next several days the sample decomposed, turning cloudy, and collecting water.

The three subsequent boules pulled from the melt were designated runs 472F, 473F, and 474F. The elpasolite phase boundary was not encountered until the last part of the 474F boule. During growth, all the boules were clear, but became cloudy upon cooling, including the elpasolite portion. Filamentary structures were present at the boundary. During subsequent weeks further decomposition in atmospheric mois-

ture occurred, especially for the pre-boundary material.

The run was extremely useful, however, because it yielded strong evidence that constitutional supercooling is the principal cause of the poor results. Starting late in the 472F run, the melt near the growth interface broke up into cells, and the pulling had to be stopped to allow the melt to remix itself. When pulling was resumed, even at only 0.5 mm/hour, it took only two or three hours before the cellular structure reappeared. (See Figures 16 a,b, and c.)

Rb_2NaYF_6

The first growth of Rb_2NaYF_6 was by Czochralski pulling (run 449F) from an undoped Na-enriched melt. Nucleation was started on a platinum wire, and a bell-shaped boule was grown. The run was discontinued because the interface had become concave, and the elpasolite phase boundary had already appeared and was a third of the way up the boule. As before, both the pre-boundary and post-boundary phases were clear during growth, but the former turned opaque upon cooling to room temperature. (See Figure 17.)

At this point, a small amount (approximately 0.5 mole %) of CeF_3 was introduced into the crucible through a furnace window, and the run was resumed, starting with a new platinum wire. A roughly onion-shaped crystal was grown; it was clear, single crystal elpasolite. There were some radial cracks extending from the platinum wire. (See Figure

18.)

Bridgman growth of several Rb_2NaYF_6 crystals was carried out. First, a Na- enriched feed doped with 5% Er was prepared. Two attempts were made to grow a crystal. The first one (13B) produced a milky-colored polycrystalline boule because of a sudden temperature rise during the run due to breakage of the quartz tube causing the molybdenum heat shield to slip downward. The second attempt (14B) was successful, producing about a centimeter of clear, single crystal material in the midsection of the boule, with mixed phase sections at either end. (See Figure 19.) The boundary between the first phase and the elpasolite seems to have a filamentary structure, and the first half centimeter of the elpasolite section is full of long axial streams of inclusions which terminate abruptly at the start of the clear section. The absence of pink tint anywhere along the boule is notable. Er^{3+} in a non-inversion site would produce such coloration, especially at a 5% concentration level. In these runs the finned crucible was used, and the pedestal was air-cooled.

Rb_2NaYF_6 was grown doped with 5% Nd from a Na-enriched melt (Run 15B). Again the boule showed the characteristic three-part structure, but the elpasolite was polycrystalline. Inspection of slices revealed a cellular structure, with the cells becoming smaller and more numerous toward the top. The elpasolite also had a light violet tint

which intensified greatly toward the top. The top of the boule displayed a deep violet cap. Since the Er-doped sample was grown with the same doping concentration and under similar conditions, the results indicate constitutional supercooling due to the large amount of Nd in the melt. The violet tint was due to a precipitate between the grains since Nd in a cubic site (and in single crystals of this elpasolite) does not show such coloration.

Starting with this run, the longer, finless crucible was used. The greater length of the crucible enabled the melt to be positioned higher up into the coil, increasing the radial heat input in order to encourage a concave growth interface. The finless design was intended to increase the axial heat removal in order to mitigate constitutional supercooling.

Run 16B was Rb_2NaYF_6 doped with 1% La. The resulting boule had the characteristic three sections again; the middle section was clear, single crystal elpasolite, about centimeter in length, although there were some axial bubble streams in the lower portion. Comparing the result with run 14B, the finless crucible did not increase the amount of clear material.

Run 17B was doped with 1% Nd. Again, the boule had a centimeter of clear, single crystal elpasolite between mixed phase regions at either end. Also, there were some axial bubble streams in the clear material, particularly toward the lower end. At the upper end of the clear section,

breakage into cells occurs, a symptom of constitutional supercooling.

Run 18B was doped with 0.5% Ce. Again there was about a centimeter of clear, single crystal material between two mixed phase regions. However, the bottom tip contained a clear section, separated from the first mixed phase region by a sharp boundary. The clear tip material has not been identified. This run was carried out in forming gas (95% Ar, 5% H_2) to investigate the effect of a reducing atmosphere on the spectra of Ce. (See Figure 20.)

Starting with run 19B, the pedestal was water-cooled rather than air-cooled. Again, this was an attempt to deal with constitutional supercooling by increasing the axial temperature gradient. For Rb_2NaYF_6 the water-cooling produced good results. Run 19B was doped with 1% Nd, and runs 20B and 21B were doped with 0.5% Ce. The first two of these runs was done in argon atmosphere, and last one in forming gas. All three boules had two centimeters of clear, single crystal elpasolite between the mixed phase regions, double the amount obtained with air-cooling. The Nd-doped sample had a few axial bubble streams at the bottom portion of the clear section. As before, the sample grown in forming gas had a sizable region of unidentified clear material at the bottom tip, separated from the first mixed phase region by a sharp boundary. (See Figures 21, 22, and 23.)

Rb_2NaYF_6 displays behavior very similar to K_2NaYF_6. The constitutional supercooling problem seems to be far less severe, however, and this has allowed for the growth of clear single crystals. The quality of Brigman-grown samples may indeed be improved by attempting the same measures suggested for K_2NaYF_6, that is, use of a wide, thin-walled crucible, and experimenting to find a composition closer to the elpasolite phase field.

3.5 X-ray Analysis

On each boule grown by the Bridgman method, x-ray powder patterns were run. The purpose was simply to verify that the elpasolite phase was present and to measure the lattice constant. Therefore, the diffractometer scans were limited to low angles. (2Θ ran from 80 to 10 degrees.)

In all the K_2NaYF_6 and Rb_2NaYF_6 boules the post-boundary material displays the elpasolite powder pattern. Rb_2NaScF_6 displays the elpasolite powder pattern throughout the length of the boule. The powder patterns were indexed on a cubic cell, and Table V lists the lattice constants, including the value for K_2NaScF_6 obtained by Gabbe. Also shown are lattice constants for the same compounds determined by other investigators.

TABLE V Elpasolite Lattice Constants (A)

Rb_2NaYF_6	8.869	8.8693 [40]
K_2NaYF_6	8.72	8.711 [42]
Rb_2NaScF_6	8.60	8.599 [44]
K_2NaScF_6	8.482	8.482 [42]

Because of the poor crystal growth results, however, x-ray powder patterns were run on the pre-boundary material in the K_2NaYF_6 runs. This powder pattern is composition dependent. It shows a diffuse elpasolite-like pattern plus many additional reflections. For the stoichiometric melt, the additional reflections are about equal in intensity to the "elpasolite" reflections; for the Na-enriched melt, the "elpasolite" reflections are stronger. This is consistent with a two-phase mixture resulting from decomposition of a high temperature solid solution of which elpasolite is an end member. No concerted effort was made to identify the exact nature of the phases present.

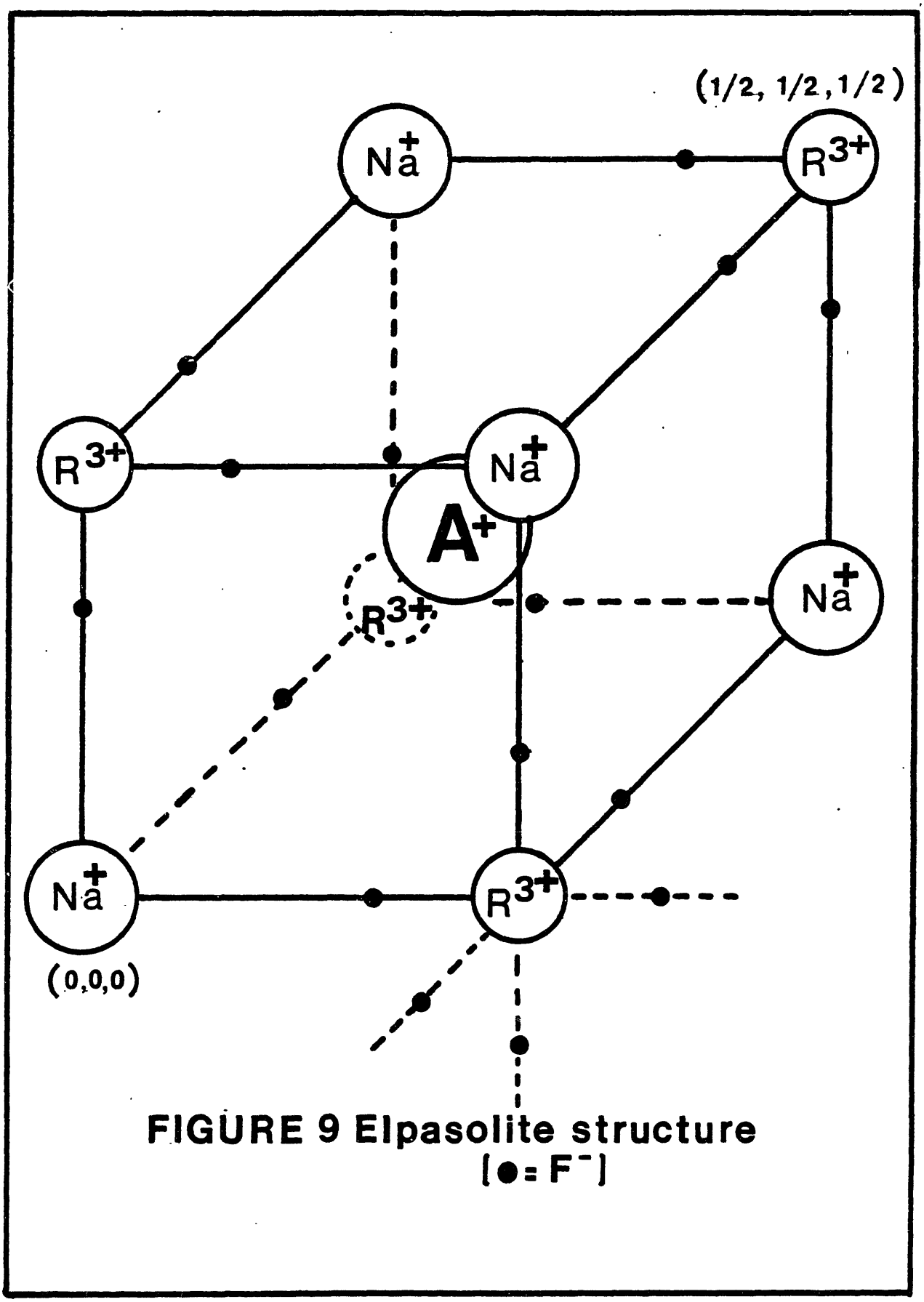

FIGURE 9 Elpasolite structure
[● = F^-]

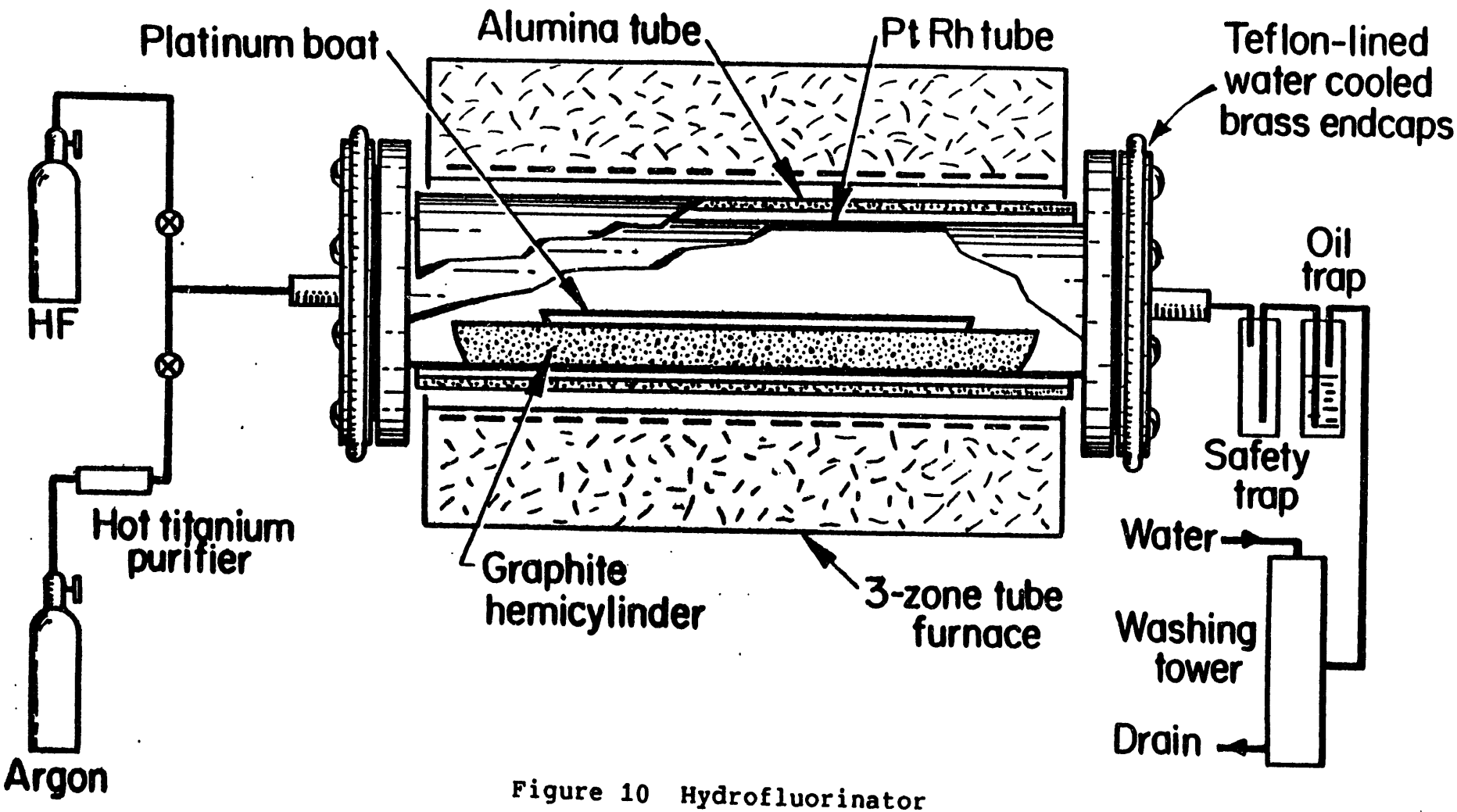

Figure 10 Hydrofluorinator

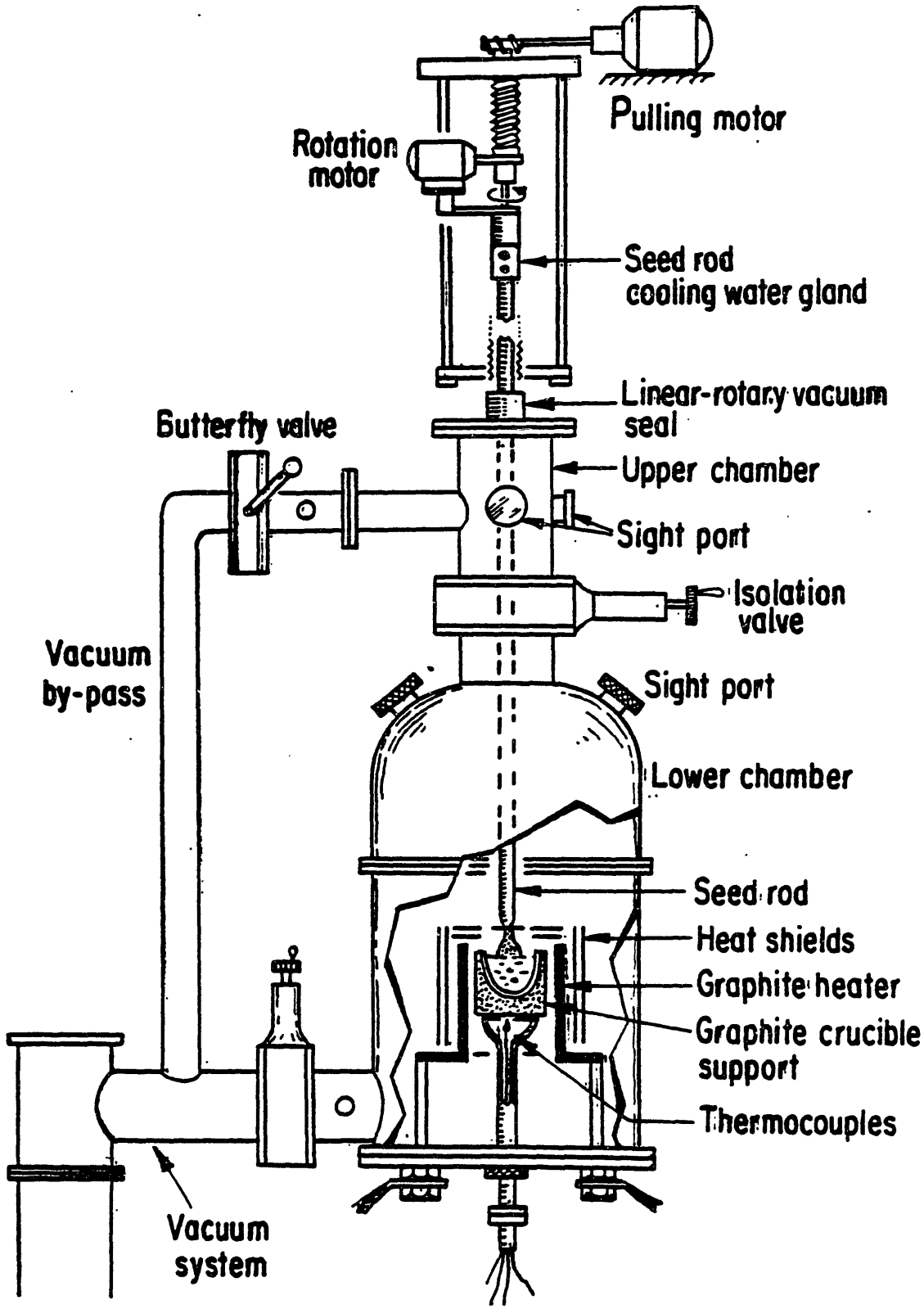

Figure 11 Czochralski Furnace

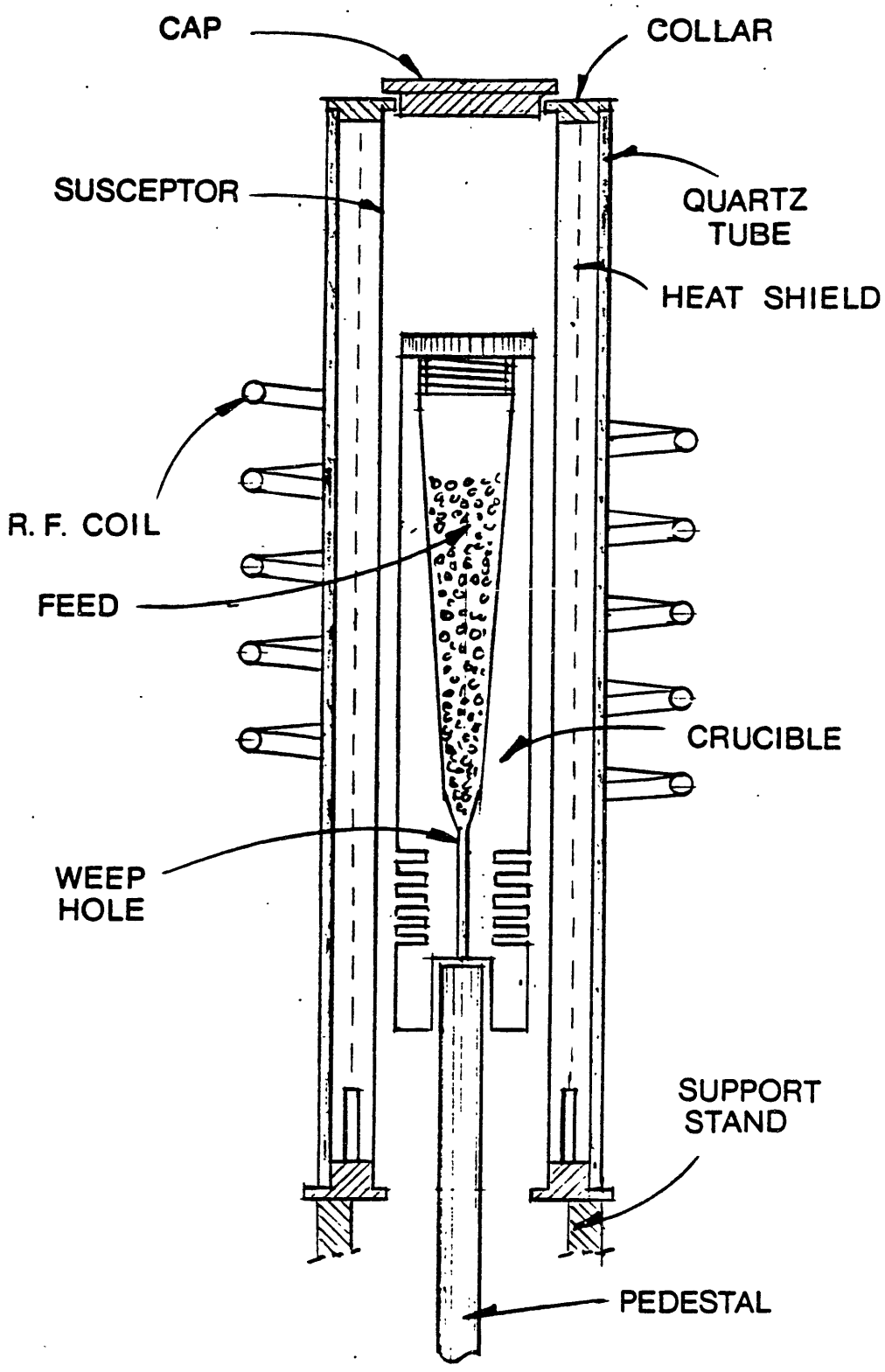

Figure 12 Bridgman Furnace

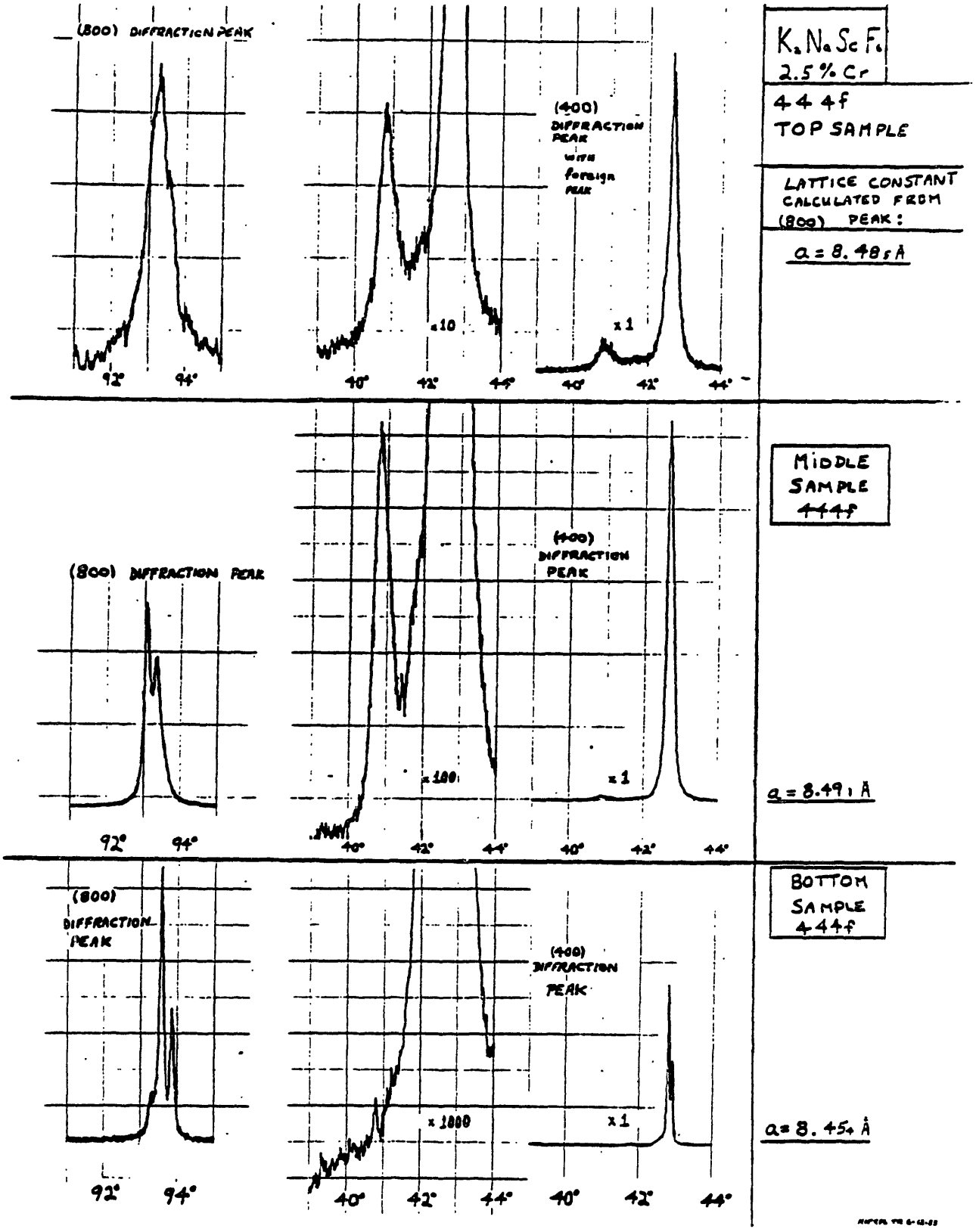

Figure 13 K_2NaScF_6 X-ray Diffraction Pattern

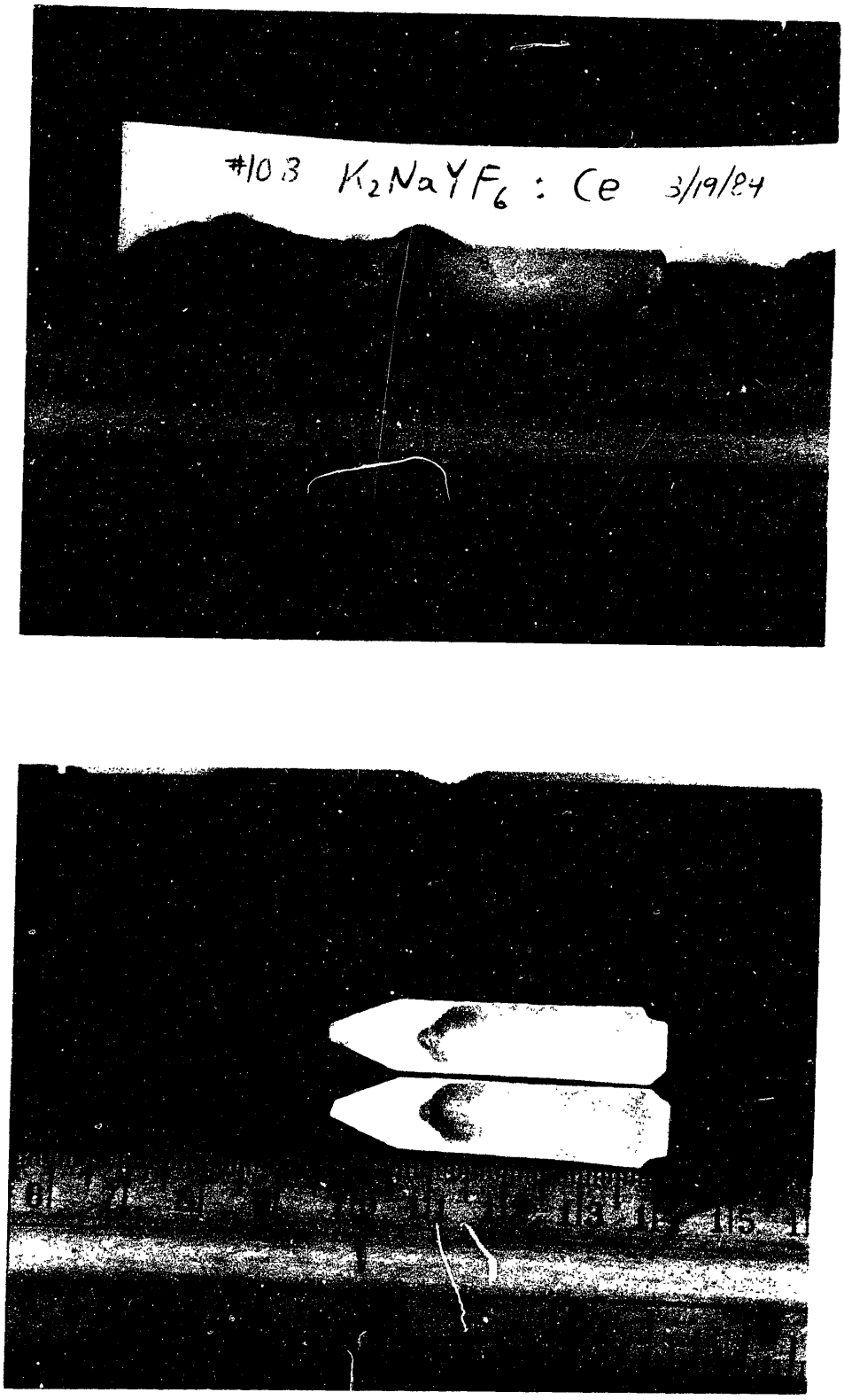

Figure 14 Results of Run 10B

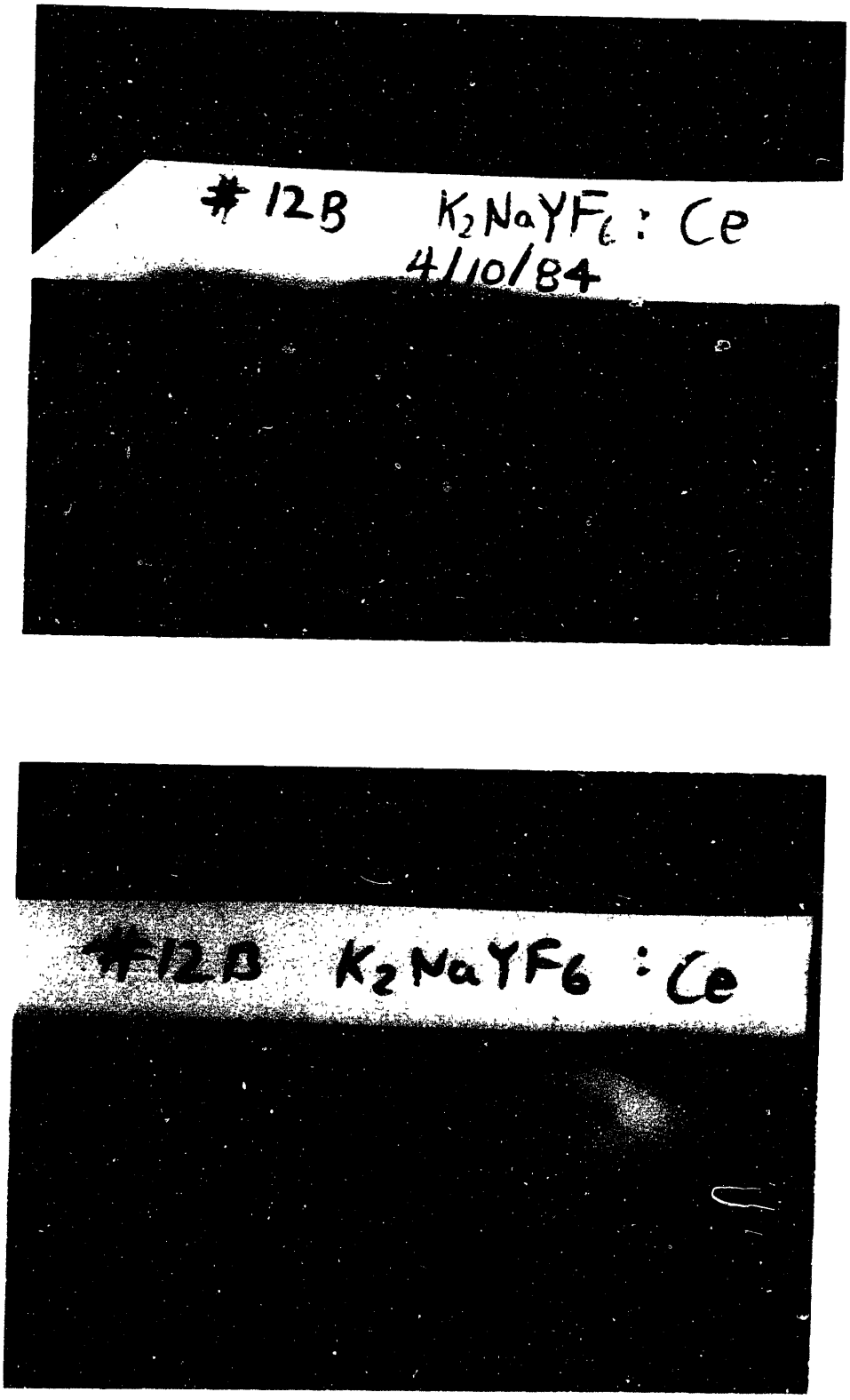

Figure 15 Results of Run 12B

Figure 16a 472F Results

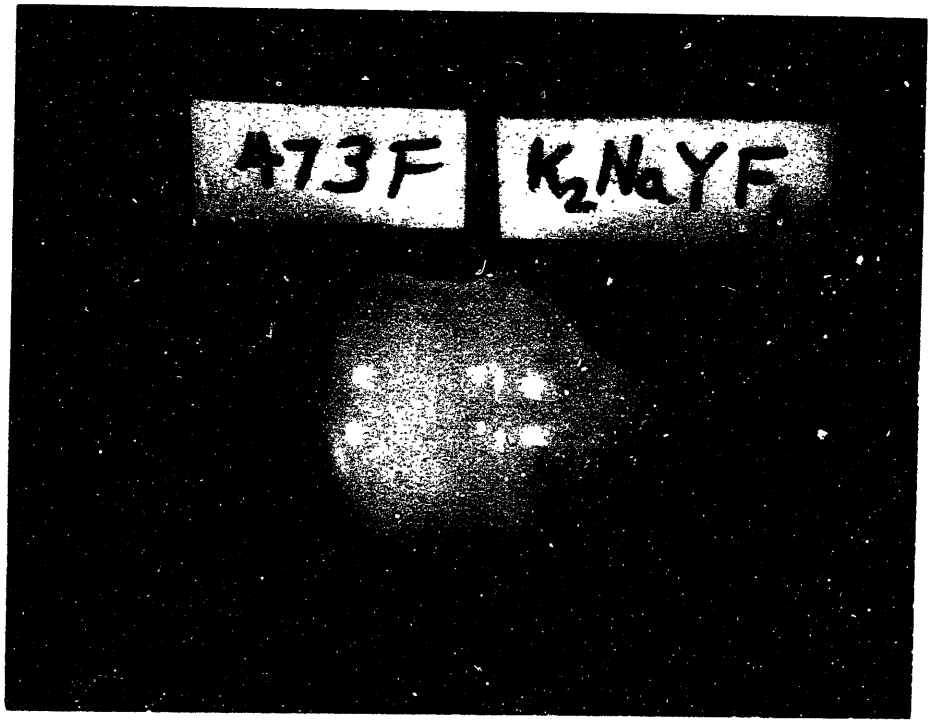

Figure 16b 473F Results

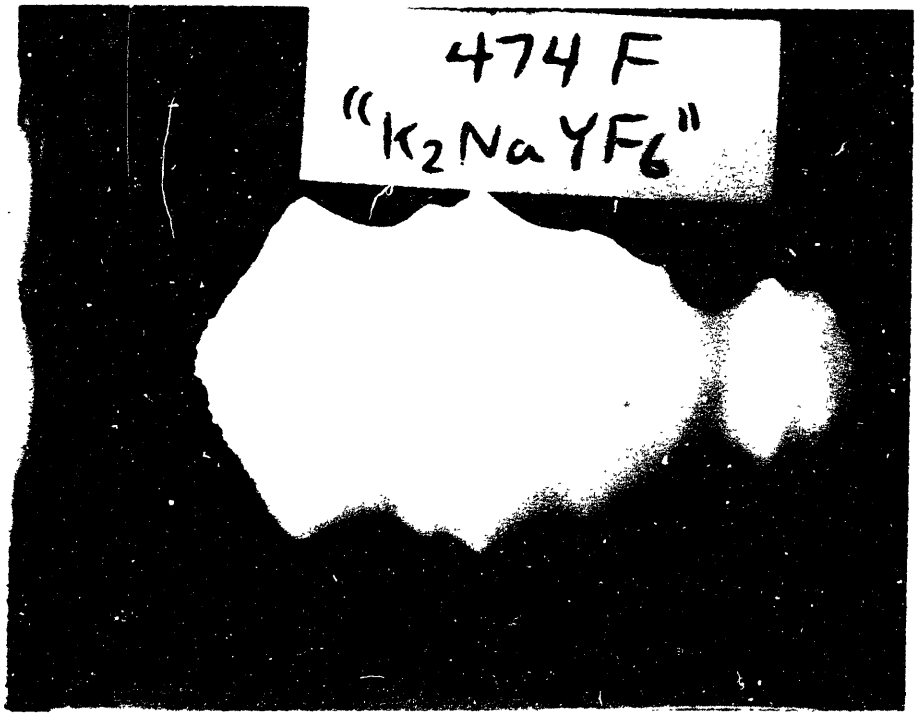

Figure 16c 474F Results. Note the boundary at 10.9 cm.

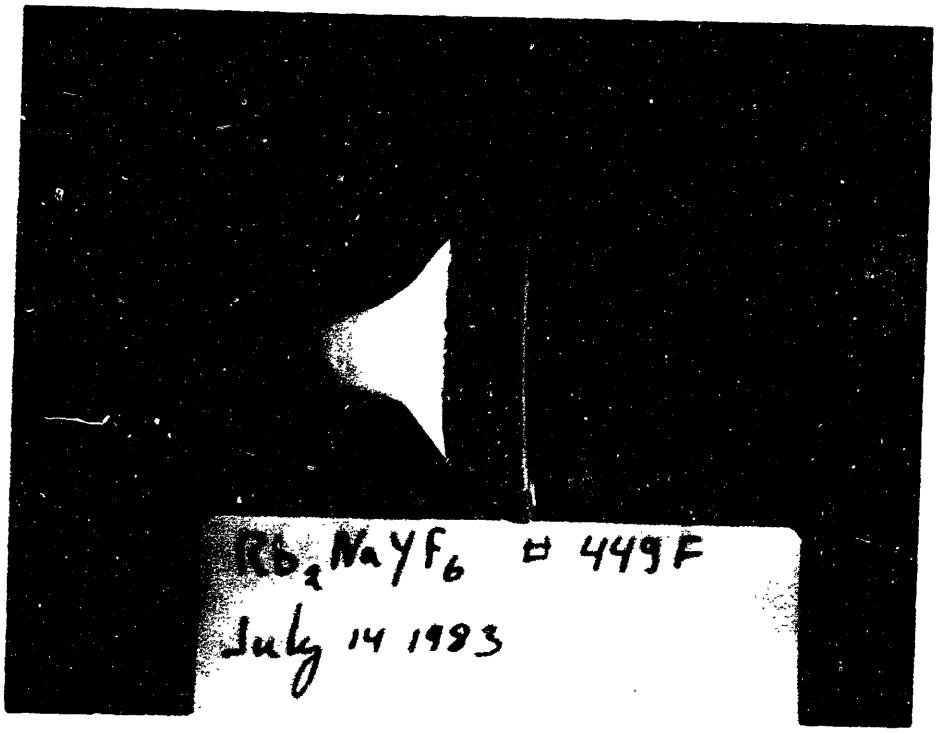

Figure 17 449F Results

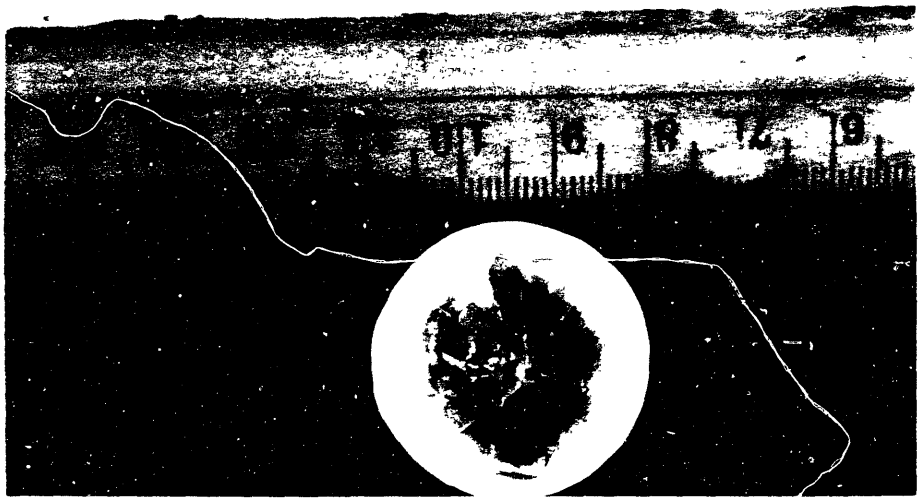

450F Rb_2NaYF_6

Figure 18 Top View of 450F

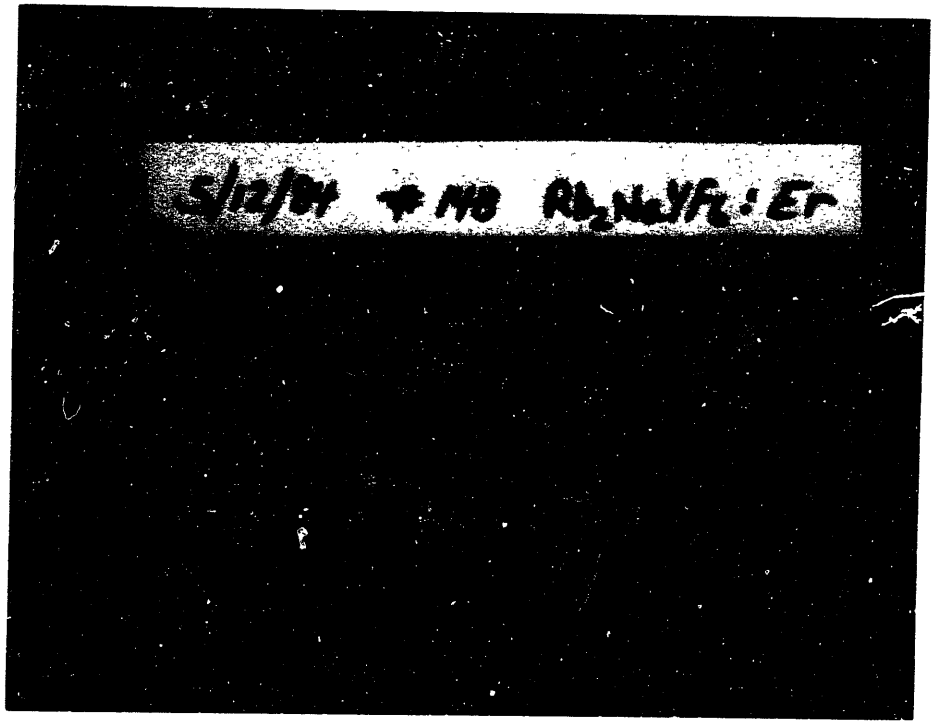

Figure 19 Results of Run 14B

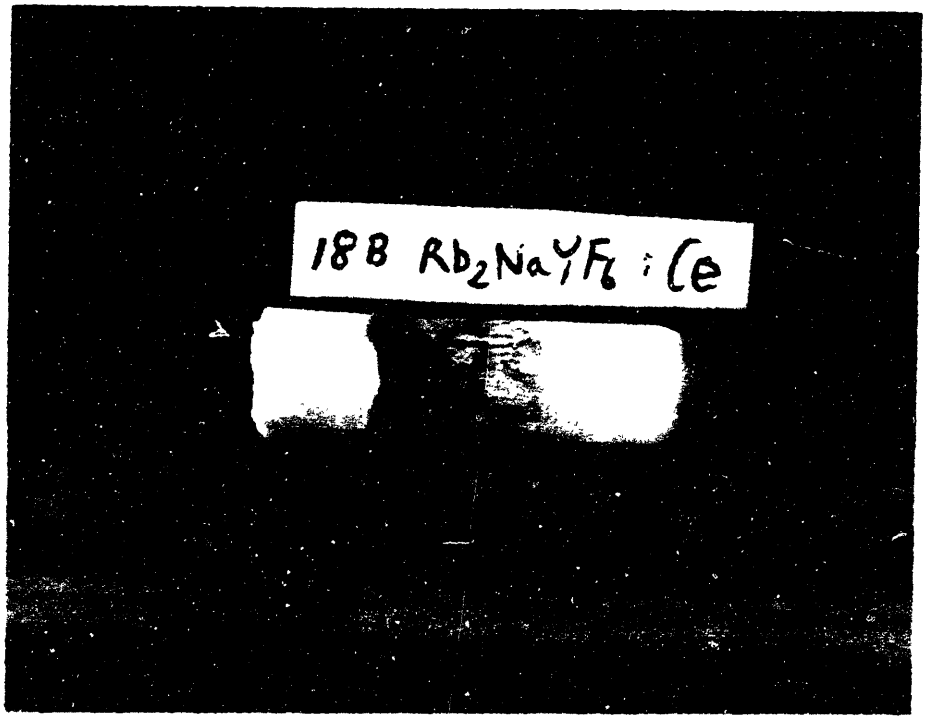

Figure 20 Results of Run 18B

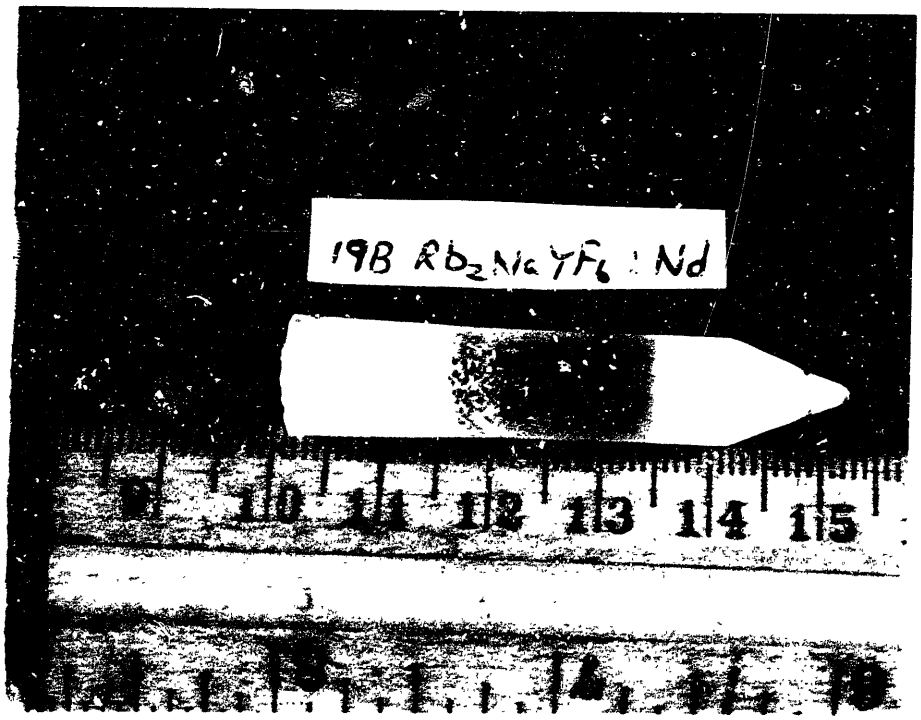

Figure 21 Results of Run 19B

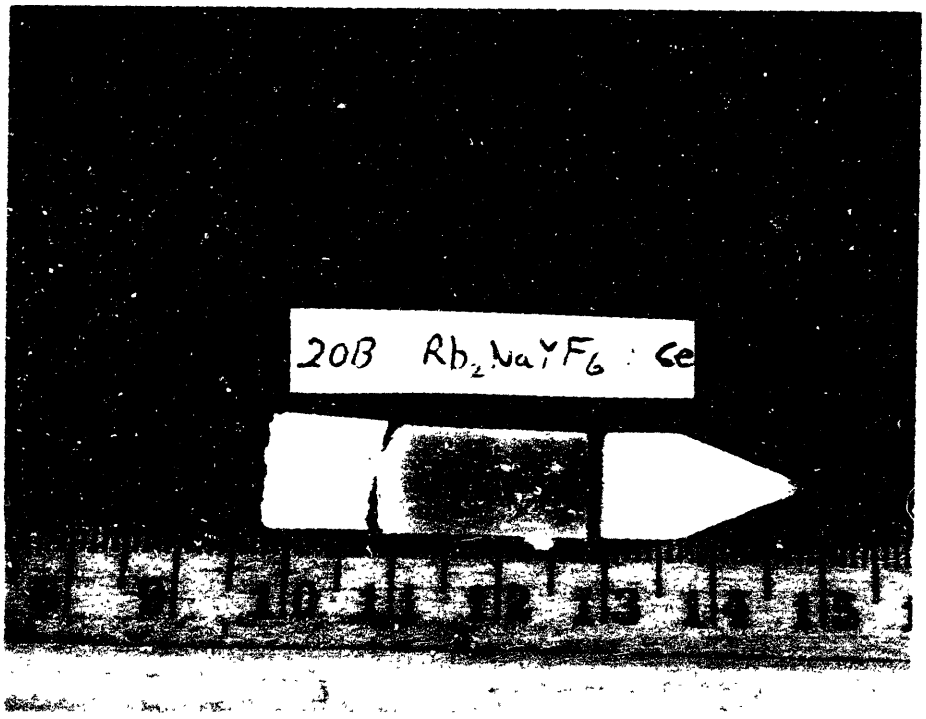

Figure 22 Results of Run 20B

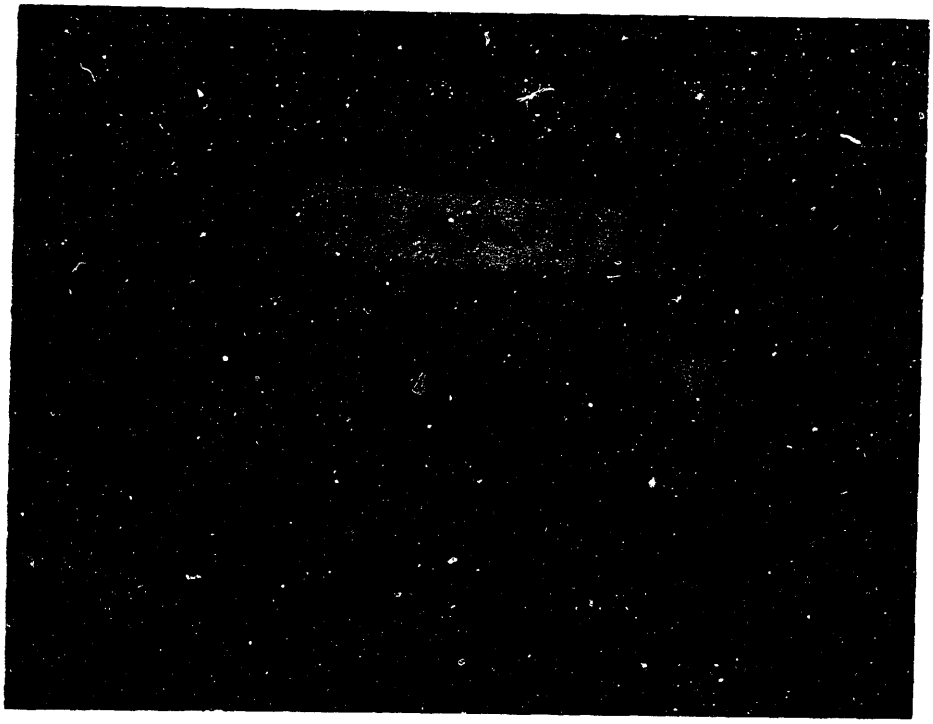

Figure 23 Results of Run 21B

CHAPTER IV

SPECTROSCOPY

4.1 Introduction

Interest in the Ce^{3+}-doped fluoride elpasolites was first sparked by Richard Chang [57] at Yale, who measured fluorescence, excitation and excited-state absorption on polycrystalline samples of Cs_2NaYF_6:Ce. He found broadband blue emission centered at 450 nm, a pump band centered at 310 nm which is compatible with nitrogen-laser- and XeCl-laser- pumping, and observed optical gain. So the Ce^{3+}-doped fluoride elpasolites showed promise as tunable blue laser materials with low excited state absorption and practical resonant pumping schemes.

The blue emission is significant because in other fluorides with Y^{3+} sites, such as YLF, LaF_3 and BaY_3F_8, the emission of Ce^{3+} is observed in the uv near 300 nm. The goal of this research was to measure 5d splittings, centroids, and Stokes shifts in the elpasolites in order to test the effect of "site size", and also to make possible a comparison with the lower symmetry fluorides.

We have measured the absorption and emission spectra of Ce, and confirmed that the absorption bands are due to Ce by

performing excitation measurements. The energy level positions are determined using a semiclassical approach, that is, band centroids in the absorption and transmission spectra are assumed to measure the energies of the purely electronic transitions with the lattice fixed in the equilibrium position. The difference in centroid between the lowest energy 4f to 5d absorption band and the corresponding emission band is the Stokes shift.

K_2NaYF_6 and Rb_2NaYF_6 display two distinct Ce^{3+} emitting centers. Thus much of the experimental work involved identification of the "normal" site.

4.2 Experimental

Figure 24 is a diagram of the measurement system used for emission and excitation measurements. The sample was excited by a 1000W xenon arc lamp focused through a McPherson 0.3-meter scanning monochromator. The monochromator housed a Bausch and Lomb 1200 line/mm holographic grating blazed at 250 nm. The output beam from the monochromator was focused onto the sample with a quartz lens. The fluorescence from the sample was focused with reflective optics onto the entrance slit of a McPherson 1-meter scanning monochromator. The monochromator housed a Bausch and Lomb 1200 line/mm ruled plane grating blazed at 200 nm. A tuning fork chopper was mounted at the entrance

slit and chopped the fluorescence at 400 Hz, providing a reference signal for synchronous detection. For blue-green or near uv detection, the photomultiplier tube at the exit slit was a Hamamatsu R292. Corning glass filters were used as needed in the excitation and detection paths. The detected signal was amplified by a PAR HR-8 lock-in amplifier.

The measurements were performed under computer control [58]. A Data General Nova 3 computer controlled the scanning of the monochromators, sampled the output of the lock-in, performed data reduction and floppy-disk storage, and plotted the spectra on an HP 7523B plotter. The computer was used to correct the data for the spectral response of the detection system, or the spectrum of the excitation source. (This correction, called "normalization", was always done on a radiant power basis rather than on a photon-counting basis.) The computer was also used to calibrate the transmission wavelengths of the monochromators, perform baseline subtraction, integration of spectra, and other data processing tasks.

Emission spectra were measured by fixing the excitation wavelength and scanning the detection wavelength. To calibrate the spectral response of the detection system, an EPI-1363 tungsten filament lamp operated at 8.3 amps was used. Its radiation at a 50 cm distance was apertured and focused onto the entrance slit of the 1-meter monochromator.

Its emission spectrum was measured and then divided by lamp irradiance curves obtained at NBS for the same current and distance.

Excitation spectra were measured by fixing the detection wavelength and scanning the excitation wavelength. Normalization required the measurement of the spectrum of the exciting beam at the position of the sample. For uv work, this measurement was first attempted by placing an EG&G FND100Q silicon photodiode at the position of the sample, scanning the excitation wavelength, and then dividing the signal by the spectral response of the diode as published on its data sheet. This was found to be inadequate at wavelengths below 250 nm because the light transmitted in first order through the 0.3-meter monochromator is weak, and the photodiode response falls off at low wavelengths, causing the signal to be dominated by "ghost" beams of other wavelengths due to spurious multipath transmissions through the monochromator. Thus it was desirable to characterize the "ghost" spectra as well as the desired excitation beam. This was done by placing a $MgSO_4$-coated diffuse reflector at the sample position, focusing the illuminated area of the surface onto the entrance slit of the 1-meter monochromator, and measuring the spectrum in the 200 to 350 nm range for various settings of the 0.3-meter monochromator wavelength. This was done for settings ranging from 200 to 350 nm in 20 nm increments.

Normalization of the spectra was achieved by reflecting deuterium lamp radiation off the diffuse reflector, measuring the spectrum, and dividing by NBS curves for the irradiance of the deuterium lamp.

For each wavelength setting of the 0.3-meter monochromator, the peak value of the first order transmission light was recorded, as well as that of any "ghost" lines. A data file containing a "continuous" spectrum for the filtered xenon lamp was constructed by linear interpolation between the measured peak values of the first order transmissions. This data file was extended to 400 nm using the silicon photodiode. The linear interpolation procedure was deemed adequate because the xenon lamp emits a line-free continuum in the 200-400 nm region. In subsequent excitation spectra, this data file was used for normalization.

The ghost spectrum of the 0.3-meter monochromator contains one principal ghost when the desired wavelength is in the 200 to 350 nm region. When the monochromator is set to 200 nm with its slits wide open, it transmits a ghost at 321 nm whose peak intensity is 60 % of the peak intensity at 200 nm. As the wavelength is scanned upward, the ghost wavelength tracks the desired wavelength in a linear fashion, with a slope of 0.58. At a wavelength setting of 240 nm, the ghost is at 344 nm and has only 5% the peak intensity of the 240 nm line. Closing down the slits

improves the signal-to-ghost ratio. Table VI summarizes the results of this calibration in arbitrary units of intensity.

TABLE VI Characterization of Filtered Xenon Lamp

λ(nm)	I	λ_{ghost}	I_{ghost}	I_{ghost}/I
200	1.00	320.9	0.60	0.60
210	2.07	326.7	0.81	0.39
220	3.14	333.3	0.84	0.27
230	11.5	338.6	0.96	0.08
240	19.9	344.2	1.03	0.05
260	48.4	355.7		
280	84.7	367.5		
300	126	379.1		
320	154	390.8		
340	149	402.5		
349	151			
356.4	148			
367.3	144			
375.5	150			
383.6	164			
389.1	172			
398.2	205			

In measuring excitation spectra in the 200 to 350 nm region, the ghost would scatter off the sample and propagate to the detector whenever the observation wavelength equalled the ghost wavelength. This would create a false peak in the excitation spectrum. The method used to check the genuineness of features was to repeat the measurement with a Corning glass filter in the excitation beam which cut out the desired light and passed the ghost. Features reappearing in this "ghostpass" spectrum were revealed to be bogus.

Below 200 nm, transmission measurements were done on a vacuum uv spectrometer designed by Roger French and Hans Jenssen [59]. The detectors for the reference and transmission paths were Hamamatsu R1080 photomultipliers, each in a special high vacuum hybrid assembly in which the tube and divider chain are potted inside a black-anodized aluminum case.

Fluorescent decay measurements were done by exciting the sample by either a Molectron UV 12 pulsed nitrogen laser, or by a Molectron DL-II tunable dye laser pumped by the nitrogen laser. The fluorescent wavelength of interest was isolated using a Jarrell-Ash Model 82-410 monochromator, Corning glass filters, and/or interference filters. The fluorescence was detected with an RCA 6199, RCA 7102, Hamamatsu R292, or a dry-ice-cooled Amperex 150 CVP

photomultiplier tube. A Tektronix 7623 oscilloscope was used as a wideband amplifier and the vertical output signal from it was averaged and processed by an Analogic Data Precision D-6000 Waveform Analyzer.

4.3 Optical Spectroscopy and Results

Initially, all four elpasolites doped with cerium were spectroscopically evaluated. Emission, excitation, and absorption spectra were measured at room temperature. (An absorption spectrum was not obtained for K_2NaYF_6 because there were no clear single crystalline samples.) The samples used were Czochralski-grown Rb_2NaYF_6 (Gabbe run 401F) doped with 1% Ce and grown from a stoichiometric melt, Czochralski-grown Rb_2NaYF_6 doped with 0.5 % Ce, grown from a Na-enriched melt (run 450F), Czochralski-grown K_2NaScF_6 doped with 1 % Ce, grown from a stoichiometric melt (Gabbe run 438F), Bridgman-grown Rb_2NaScF_6 with 1 % Ce (run 3B), and Bridgman-grown K_2NaYF_6 with 0.5 % Ce (run 6B).

In Rb_2NaYF_6 the excitation spectrum of the 400 nm emission (Figure 25) consists of a band centered at 310 nm with a shoulder on its short wavelength side and a weak peak at 240 nm. As the detection wavelength decreases, however, the shoulder and the 240 nm band grow and the 310 nm band shrinks. At 340 nm detection, the 310 nm band is barely discernible. There are two distinct emission spectra as well (Figure 26). Pumping at 320 nm produces a broad

emission band peaking at 390 nm, and 240 nm pumping produces a narrower band peaking at 340 nm. 295 nm pumping produces a mixture of the two emission bands.

The absorption spectra of the two Rb_2NaYF_6 samples differ (Figures 27, 28). While the 310 nm band is present in both cases, additional peaks on the low wavelength side are present in the sample grown from the Na-enriched melt (450F). The additional peaks are not present in the excitation spectrum, however. Also the baseline rises much more as the short-wavelength limit of the Cary 17D is approached. Both spectra show a bump at 235 nm. For comparison, the absorption spectrum of undoped Rb_2NaYF_6 was done and is shown in Figure 29. The 310 nm band and its shoulder are absent, but there is a bump at 235 nm, and the baseline rises in the short wavelength region.

K_2NaYF_6 behaves in a similar way. The excitation spectrum for 400 nm emission (Figure 30) consists of a band at 315 nm with a shoulder extending down to 280 nm, and a weak band centered at 255 nm. As the detection wavelength decreases, bands at 255 and 295 nm shoot up, at the expense of the 315 nm band. At 330 nm detection, the 315 nm band is gone (Figure 31). Again, two distinct emission spectra are observed (Figure 32). For 250, 280, or 295 nm pumping, the emission peaks at 340 nm. For 315 nm pumping, it peaks just above 400 nm. In Figure 32 the ghost lines from the 0.3-meter monochromator can be seen superimposed on the

broadband emission from the sample.

The two curves in Figure 30 were measured for the same slab of material 11 days apart, and the upper curve is the latter result. The sample was polycrystalline with a precipitate between the grains, and was susceptible to decomposition in atmospheric moisture. The additional features in the latter measurement are probably related to decomposition.

The Rb_2NaScF_6 excitation spectrum at 380 nm (Figure 33) consists of a double-humped band centered at 315 nm with a shoulder on the low wavelength side, and a very feeble band at 250 nm. As the observation wavelength increases, the shoulder shrinks, and for 500 nm detection it is gone (Figures 34, 35). 320 nm pumping produces an emission band which peaks at 380 nm but has an anomalously broad tail extending out beyond 550 nm (Figure 36). The emission spectrum of the second site suggested by the disappearing shoulder in the excitation measurement has not been observed.

The absorption spectrum of Rb_2NaScF_6 shows the 315 nm band as well as its low wavelength shoulder (Figure 37). There is also a rising baseline in the short-wavelength region with a bump at 235 nm.

K_2NaScF_6 has only one emitting center. It has excitation bands (Figure 38) at 240 and 270 nm, and emission centered just below 300 nm (Figure 39). Of the four elpasolites, this is the only one in which the ground state

spin-orbit splitting of Ce^{3+} is clearly resolvable in the emission spectrum. The absorption spectrum shows the 270 and 240 nm bands plus bands at 210 and 200 nm (Figure 40).

Fluorescent decay was measured for the 400 nm emission in Rb_2NaYF_6, Rb_2NaScF_6, and K_2NaYF_6. The pulsed nitrogen laser was used to excite the long wavelength tails of the 310-315 nm absorption bands and the decays were recorded on a Tektronix 7904 high speed oscilloscope using an oscilloscope camera. The decays were exponential and in the 70 to 90 ns range.

These results raised the question of whether or not disordering in the host creates an alternate Y^{3+} site for trivalent rare earths. To test for this possibility, The Er-doped Rb_2NaYF_6 was grown. First, Er^{3+} is a very close match in ionic radius for Y^{3+}. Thus if some disordering occurs which gives rise to an alternate Y^{3+} site, Er^{3+} would serve as a spectroscopic "marker" for the alternate site. Second, the $^4I_{15/2}$ to $^4I_{13/2}$ transitions in the absorption spectrum of Er^{3+} at 1.6 μm are magnetic-dipole allowed. Thus a low temperature absorption spectrum identifies the number and position of the $^4I_{13/2}$ levels, and this can be compared to what is expected for the normal Y^{3+} site. Third, most of the other optical transitions of Er^{3+} are forbidden in inversion symmetry, leading to the absence of the pink coloration of the sample that accompanies these

transitions when they are forced-electric-dipole allowed. Fourth, if a fairly sizable section of clear material can be grown, the distribution coefficient can be estimated by measuring the absorption coefficients at different positions along the boule.

The feed for Bridgman runs 13B and 14B was prepared with a 5% doping concentration of erbium, yet there was no pink coloration, either in the feed or the subsequently grown boules. Absorption spectra were measured on cut and polished slabs from 14B at room temperature, 77K, and 8K. The 8K absorption spectrum in the 1.6 μm region is shown in Figure 41. The three lines are the only ones which intensify as the sample is cooled, and their relative spectral positions closely match what is predicted by lattice sums run at Harry Diamond Laboratories [60] for the normal Y site, and the relative intensities of the three transitions also agree with the theoretically predicted pattern (Table VII). The theoretical levels in Table VII were obtained by taking phenomenological crystal field parameters for Er^{3+} in $Cs_2NaErCl_6$ and scaling according to the point charge model to account for the smaller lattice constant of the fluoride elpasolite.

TABLE VII Er^{3+} $^4I_{13/2}$ Levels
and absorption line strengths in Rb_2NaYF_6
Strengths are given as the square of the
magnetic-dipole matrix element from the
ground state as calculated by Morrison.

THEORY	EXPERIMENT	STRENGTH
6509.0	6508.6	1.99
6546.0	6549.6	1.17
6576.0	6585.8	0.45
7032.6	-	0.035
7078.3	-	0.006

These magnetic-dipole transitions are allowed in the free ion, and therefore should have intensities which are relatively independent of environment. Therefore, a significant concentration of Er^{3+} in a second site would have caused additional lines to appear in the spectrum which could not be attributed to a single normal site. No such lines were observed.

The peak absorption coefficient at 1.536 μm was measured for slabs cut from the top and bottom extremes of the clear section of boule 14B. The distribution coefficient was estimated by assuming an exponential concentration profile along the boule (which is what results from a constant distribution coefficient and a homogeneous melt during growth). The value obtained was $1.08 \pm .05$, where the uncertainty arises from estimating the fractional melt

remaining for each slab. The integrated absorption coefficient was estimated for the 1.536 μm line, and the absolute concentration calculated assuming the theoretically calculated magnetic-dipole transition probability. The value obtained was 4.8% Er replacing Y. Thus, Y^{3+} is found only in its "normal" site, and Er^{3+} substitutes there with a high distribution coefficient.

Ce^{3+}, however, is 17% larger than Er^{3+}, and its incorporation might generate an optically active defect. To test this possibility, La-doped Rb_2NaYF_6 was grown (run 16B). An absorption spectrum of this material is shown in Figure 42. Again, the baseline rises at short wavelengths due to scattering, and a slight bump is present at 235 nm. The 310 nm band and its shoulder are entirely missing. This sample showed none of the fluorescence or excitation bands present in the Ce-doped elpasolite. Therefore, both emission bands arise from electronic transitions of the cerium complexes in the host.

The possibility that Ce^{4+} is incorporated into the crystal must also be tested. So, Ce-doped Rb_2NaYF_6 was grown in forming gas (95% argon, 5% hydrogen) to reduce the cerium to the trivalent state. Figures 43 and 44 show the absorption spectra of samples taken from the top, middle, and bottom portions of boules 20B (grown in argon) and 21B (grown in forming gas). The peak absorption coefficient of the 310 nm band band is only 20% greater in boule 20B than

in boule 21B. The 310 nm band is therefore due to trivalent cerium. The second site is still observed in excitation, however, and therefore also arises from trivalent cerium present in a much lower concentration.

These absorption spectra also facilitate estimation of the Ce^{3+} distribution coefficient for the site which yields the 310 nm band. The peak absorption coefficients for the top and bottom slabs from 21B were fitted to the endpoints of an exponential profile and the distribution coefficient obtained was 0.48. The assumption of of a homogeneous melt is not valid when the distribution coefficient is this low, however.

The middle slab of both 20B and 21B was cut much thicker than the top and bottom slabs so that it could be seen which features in the absorption spectrum roughly scale with sample thickness. The 310 nm band indeed scales with sample thickness, but the bump at 235 nm and the rise at 200 nm do not. Thus, only the 310 nm band arises from bulk absorption.

Nd^{3+}-doped Rb_2NaYF_6 was grown to see if there are two sites for Nd^{3+}, since Nd^{3+} is almost as large as Ce^{3+}. A 1.7 cm thick slab was cut from boule 19B, and its absorption spectrum measured. The absorption was very weak (α = 0.02 cm^{-1} at 570 nm). Again, the 310 nm band present in the cerium-doped samples was absent here.

The fluorescent decay was measured at 1.06 μm, and the decay constants are shown in Table VIII for various tempera-

tures in the 4K to 600K range. Two distinct emitting centers were observed, and the intensity of either could be enhanced at the expense of the other by fine tuning the excitation wavelength. One center has a room temperature lifetime of less than 50 μs which increases to 130 μs at liquid helium temperature. The other site has a 4.4 ms lifetime at room temperature which increases to 10.7 ms at 77K and decreases again to 6 ms at 4K. Above room temperature the lifetime shows a steady decrease to 2.85 ms at 568 K. The room temperature long decay is shown in Figure 45, where voltage is plotted on a logarithmic scale.

TABLE VIII Decay Times of Nd Emission in Rb_2NaYF_6

T (K)	τ_{long}(ms)	τ_{short} (μs)
568	2.85	
544	3.05	
519	3.10	
488	3.10	
464	3.25	
441	3.35	
394	3.45	
376	3.60	
336	3.80	
294	4.4	<50
200	5.7	
150	7.0	
100	10.6	
77	10.7	50
4	6.0	130

The emission spectra of the two sites was measured at 4K by pumping the sample with an argon-pump Rhodamine 6G cw dye laser. Again, the two sites could be separated by fine tuning the laser wavelength. The spectra are shown in Figure 46. Though the two spectra are each scaled to fill the plot, the integrated intensity is a factor of 3 or 4 times stronger for the short lifetime site. Since there are no efficient quenching paths known for the $^4F_{3/2}$ state, it is reasonable to assume that the lifetimes reflect the transition probabilities, and that the total intensity scales roughly with the product of the inverse lifetime and the concentration. By this criterion, the concentration of Nd^{3+} in the long lifetime site is about twenty times the concentration in the short lifetime site. Furthermore, the 4.4 ms room temperature lifetime is one of the longest ever observed for Nd^{3+}, which indicates high symmetry.

The following conclusions are warranted for Ce-doped Rb_2NaYF_6:

1. There are two sites, but the dominant site is the normal, high symmetry one. About 95% of the cerium goes into this site, in the trivalent state, and gives rise to the absorption at 310 nm, and the 400 nm emission band. The exact nature of the other site is unknown.

2. The 235 nm plateau in absorption is a surface

effect, because it is present in samples not doped with cerium, and is of the same intensity in all three of the slabs cut from boule 20B (the middle slab being six times as thick as the others).

3. The other site seen in the excitation spectra is really cerium. It is more prominent in the sample grown by Czochralski from a stoichiometric melt. In the Bridgman-grown samples (all grown from a Na-enriched melt) it is very weak. The splittings observed in the excitation spectra seem consistent with a roomy, low symmetry site.

Our better understanding of Rb_2NaYF_6 enables us to formulate a consistent explanation for the other elpasolites in the series. The spectrum of Ce^{3+} in the Sc^{3+} site should be similar in Rb_2NaScF_6 and K_2NaScF_6. Since they are so drastically different, it is reasonable to conclude that a low symmetry site predominates in one of the two hosts. The absorption spectrum of K_2NaScF_6 shows four levels with relatively small splittings. The spectrum in Rb_2NaScF_6 shows a single band with at least an 18000 cm^{-1} gap separating it from any others. Therefore, it is reasonable to conclude that Ce goes into the Sc site in Rb_2NaScF_6, and into a lower symmetry site in K_2NaScF_6.

Similarly, Ce^{3+} should have similar spectra in the Y sites of Rb_2NaYF_6 and K_2NaYF_6. Therefore, the 315 nm band in the latter compound is most likely due to Ce^{3+} in the Y

site.

Vacuum-uv transmission measurements were done on $Ce:Rb_2NaYF_6$, $La:Rb_2NaYF_6$, and $Ce:Rb_2NaScF_6$, in two overlapping spectral ranges, 110-210 nm and 170-270 nm. The long-wavelength scans were done with a uv quartz filter in the beam, which cuts off at 165 nm. This filters out the strong line emission of the hydrogen lamp, while passing a weaker, line-free continuum. A close match between the high-wavelength and low-wavelength scans was always obtained in the 170-210 nm region, indicating an acceptably low level of stray radiation through the monochromator.

Ce^{3+}-doped Rb_2NaYF_6 displays a weak, broad absorption band centered at 197 nm (Figures 47,48). The absorption edge at 150 nm is due to interband optical transitions in the host. La-doped Rb_2NaYF_6 completely lacks the 197 nm band but displays absorption near the band edge not present in the Ce-doped sample. The signal was also weaker because of scattering from inclusions in the sample (Figures 49, 50).

Ce^{3+}-doped Rb_2NaScF_6 displays a double-humped band with a stronger peak centered at 163 nm and a weaker one centered at 180 nm (Figures 51, 52). The band edge is also at 150 nm but the transmission values in the 150-270 nm region are lower than for the other elpasolite because of greater surface scattering.

One remaining question is the apparent weakness of the Ce^{3+} absorption in the elpasolites. The absorption coefficient per melt percent doping in Rb_2NaYF_6 is over an order of magnitude smaller than in YLF, [5] and nearly two orders of magnitude smaller than in LaF_3 [6]. Spectrochemical analysis to determine cerium concentration presents formidable difficulties, because cerium has more than one oxidation state, and because its broadened spectrum leads to greater errors due to baseline effects in absorption measurements. Interference from trace transition metals is also a concern. However, an estimate of the Nd concentration in Nd-doped Rb_2NaYF_6 can be done far more easily. Because of the closeness in the ionic radii of Nd^{3+} and Ce^{3+}, such analysis gives an indication of the concentration for the latter dopant.

The analysis was performed by dissolving the sample in an aqueous solvent and measuring the absorption spectrum on the Cary 17D spectrophotometer. The solvent consisted of 0.5 moles/liter nitric acid and 1 mole/liter aluminum nitrate. The aluminum complexes strongly with the fluoride ions, and the nitric acid prevents the formation and precipitation of aluminum hydroxide, and also assists in the dissolution of the sample. The rare earth ion forms a hydrated complex.

Attempts to dissolve crushed Rb_2NaYF_6 in the solvent by heating to 125 ^{o}C in a teflon bomb did not succeed. Even

after 48 hours, the solution contained a cloudy precipitate. Therefore, a refluxing method was attempted. The elpasolite was crushed and mixed with the solvent in a round-bottomed flask seated in a heating mantle. A water-cooled condenser column was inserted into the flask and the contents gently boiled. This procedure dissolved the elpasolite within two hours. It is likely that the fluoride was attacking the glass and complexing with Si, assisting the dissolution process.

Three solutions were prepared by this method:

1. 1 g Rb_2NaYF_6 from the midsection of boule 19B was dissolved in 20 ml of solvent.

2. 25 mg of NdF_3 was dissolved in 50 ml of solvent.

3. A large piece of feed material from run 19B was crushed and mixed. 1 g of the powder was dissolved in 20 ml of solvent.

The absorption spectrum of each of these solutions was measured on the Cary 17D spectrophotometer in a 5 cm cell. An identical cell containing only solvent was placed in the reference beam. The spectra differed only in the intensities of the Nd^{3+} absorption lines. The ratios of the peak absorbances of solutions 1 and 3 were computed for several lines yielding values of 0.187 (578 nm), 0.190 (740 nm), and 0.185 (795 nm). Since the feed material was doped

with 1 atomic % Nd, the concentration in the crystal was in the range 0.18-0.20 atomic %. Solution 2 contained nominally twice the Nd concentration as solution 3, and indeed displayed absorption lines which were 1.9 to 2.1 times as intense. The melt distribution coefficient for Nd^{3+} in this elpasolite could easily be as low as 0.10, since the sample analyzed was from the middle of the boule, where rejected Nd had accumulated in the melt.

It has been found that for a given dopant site that the distribution coefficient varies exponentially with the fractional volume mismatch between the dopant and substituted ions [61]. Assuming a distribution coefficient of 1.08 for Er^{3+} and 0.15 for Nd^{3+} in Rb_2NaYF_6, the extrapolated value for Ce^{3+} using tabulated ionic radii is 0.07. This is a factor of 2 to 3 lower than the distribution coefficient expected for Ce:YLF.

Another important difference between elpasolite and YLF is that the latter compound has 2.44 times more Y sites per unit volume. This reduces the disparity in absorption cross sections to about a factor of three, well within the plausible variation of matrix elements.

LaF_3 probably has a distribution coefficient for Ce^{3+} close to unity, and also has nearly three times the dopant site density of elpasolite. This reduces the absorption cross section disparity to about a factor of two, again quite plausible.

We conclude that there is nothing anomalous or mysteri-

ous about the low intensities of the Ce^{3+} absorption bands in Rb_2NaYF_6 as compared to other hosts. They arise from a combination of a low distribution coefficient, a low density of sites in the host crystal structure, and a low transition probability.

The broad, structureless emission of Ce^{3+} in the elpasolites is partially due to large crystal-field splittings of the 4f ground state. Theoretical calculations presented in Chapter V place the highest 4f level at 5856 cm^{-1} above the ground state in Rb_2NaYF_6. 4f-to-4f absorption lines in the Ce-doped elpasolites have been sought using the Cary 17D and the Beckman Acculab 10 Ir Spectrophotometer, but were too weak to be detected.

Figure 53 shows an emission spectrum of Ce-doped Rb_2NaYF_6 at 4 K. Although the 4f splittings still cannot be resolved, there appears to be several heavily overlapping electronic transitions. In order to ascertain if the Jahn-Teller effect is present, polarization memory was sought. A slab from boule 3B was cooled to 4 K and excited with polarized light at near normal incidence to a polished face. Emission spectra were measured along the pump propagation direction from the other polished face for polarizations parallel to and perpendicular to that of the exciting light. Then, the polarization of the exciting light was rotated 90 degrees, and the experiment repeated. No significant changes in the emission band shape were observed.

Although the sample was randomly oriented, it is unlikely that the shape of the entire emission band would remain constant if there were a significant polarization memory effect.

Although the second Ce^{3+} site in the elpasolites has not been identified, an educated guess is possible. When a helium-neon laser beam was directed through the samples of Rb_2NaYF_6 and Rb_2NaScF_6, scattering was seen only at the surfaces and not in the bulk. Therefore, the second site is not due to a precipitate. If a second phase is present, it is intergrown with the elpasolite; if such a second phase is not cubic, the intergrowth would have to be occurring on a very fine level with domains oriented in all three directions in order for the sample to appear optically isotropic. The satellite reflections of Figure 13 are symptomatic of an intergrown second phase; K_2NaScF_6 is the only elpasolite displaying such reflections and is also the only elpasolite in which the second site is spectroscopically dominant. Therefore, one possible explanation is that the second phase houses a site with a much higher distribution coefficient than the normal site, but only in K_2NaScF_6 does the second phase occur in high enough concentrations to drown out the normal site. Another explanation is that the second site is the Rb or K site in elpasolite since rare earths tend to go into sites of large size and high coordination number. Indeed, the absorption spectrum of $Ce:K_2NaScF_6$ looks like that of a large, low symmetry site. However, the fact that

the second site is far more prominent in Rb_2NaYF_6 than in Rb_2NaScF_6 is consistent with the hypothesis that disordering in the former compound assists in providing the necessary charge compensation.

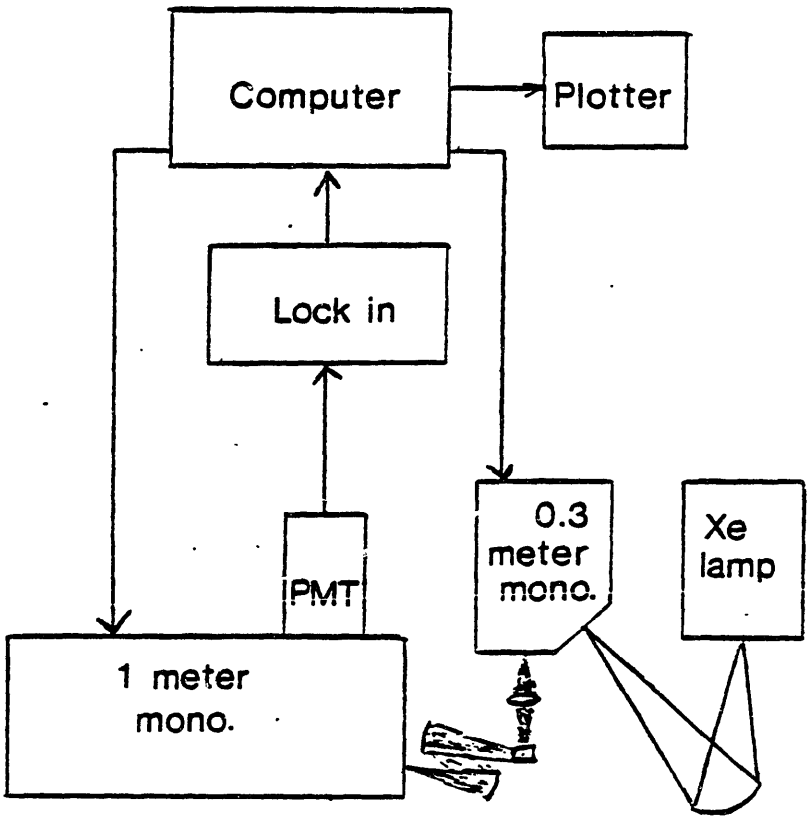

Figure 24 Experimental Apparatus for Emission and Excitation Spectroscopy

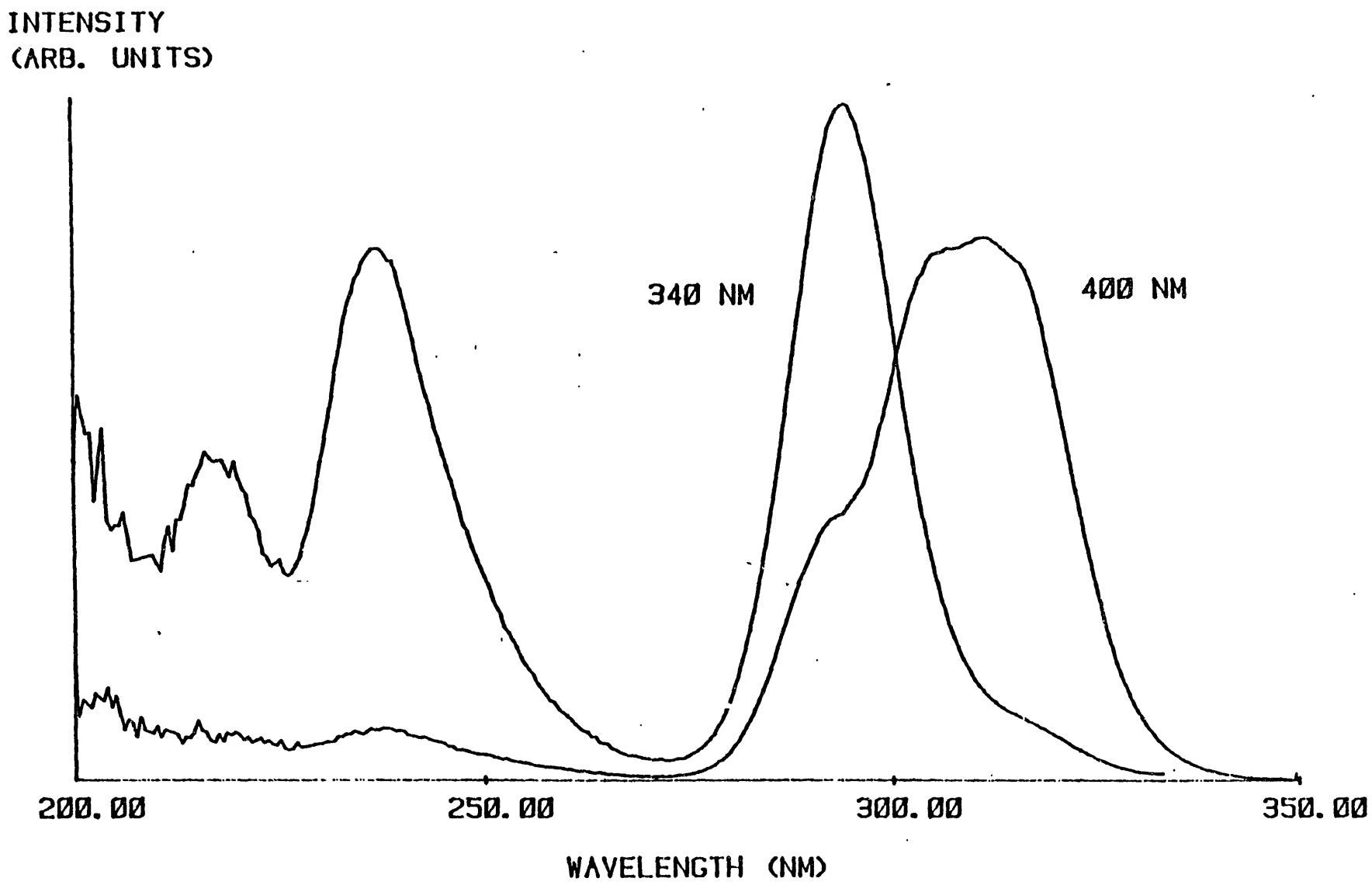

Figure 25 Rb_2NaYF_6 Excitation Spectra

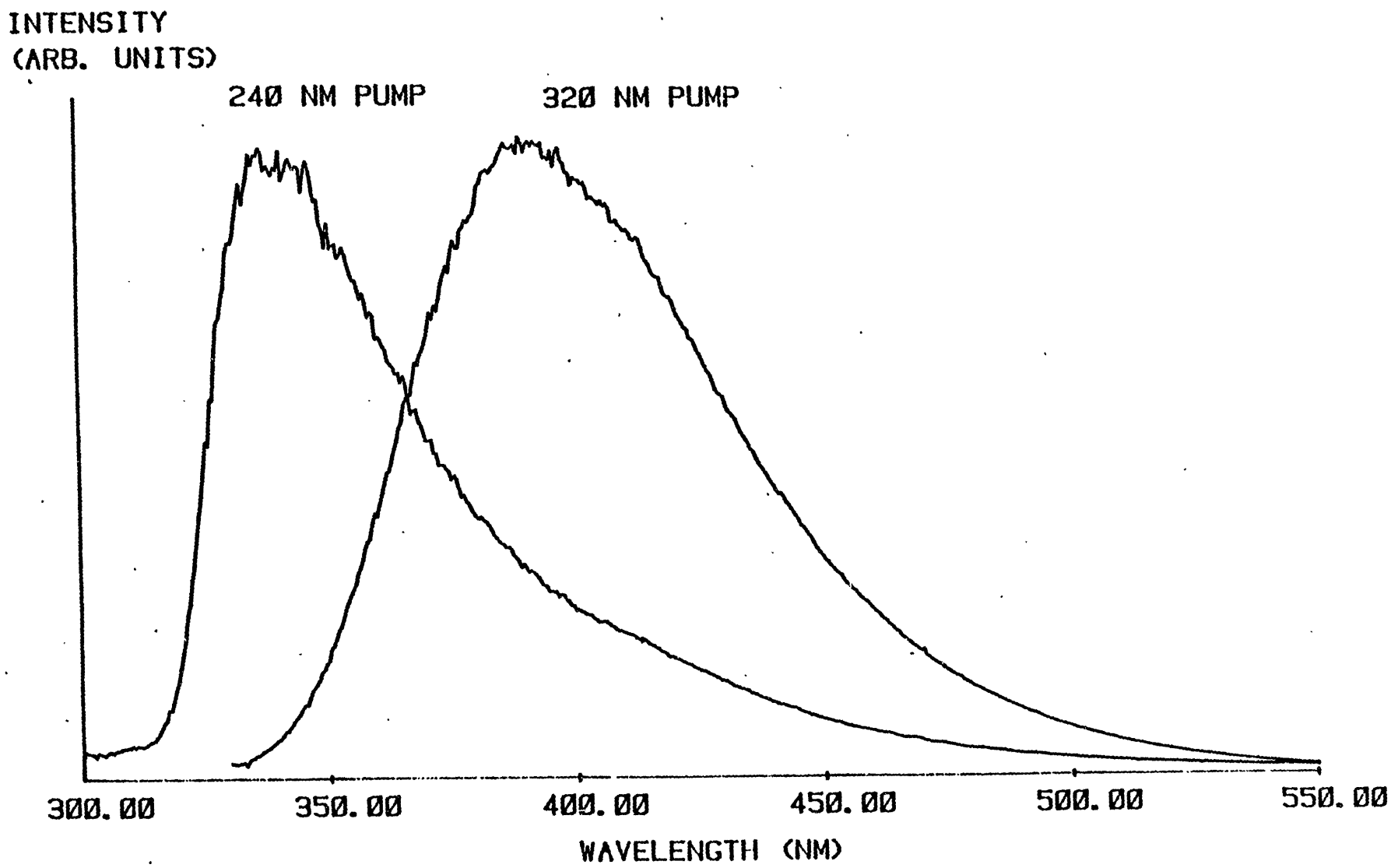

Figure 26 Rb_2NaYF_6 Emission Spectra

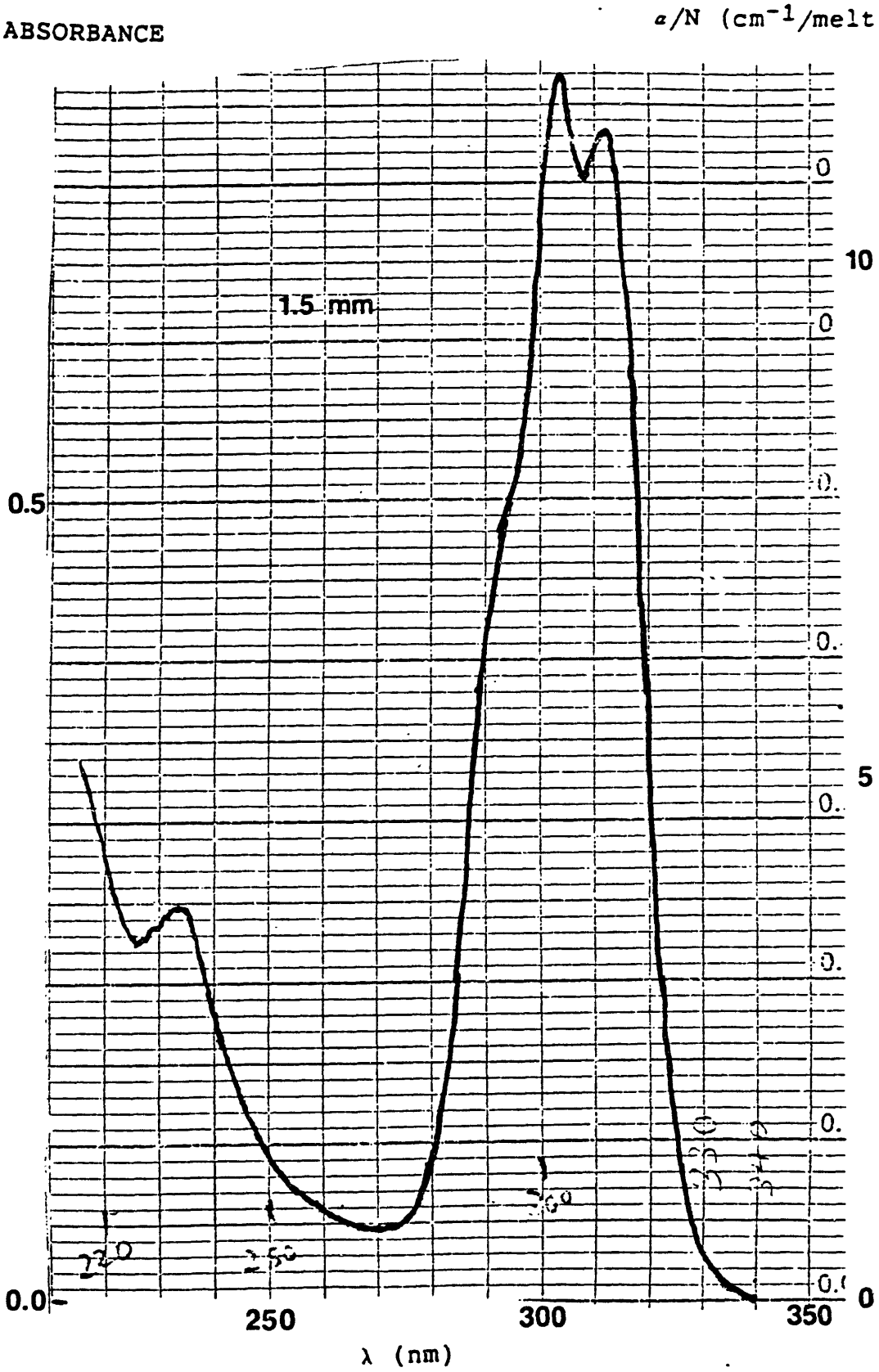

Figure 27 Rb_2NaYF_6:Ce Absorption Spectrum (sample 401F)

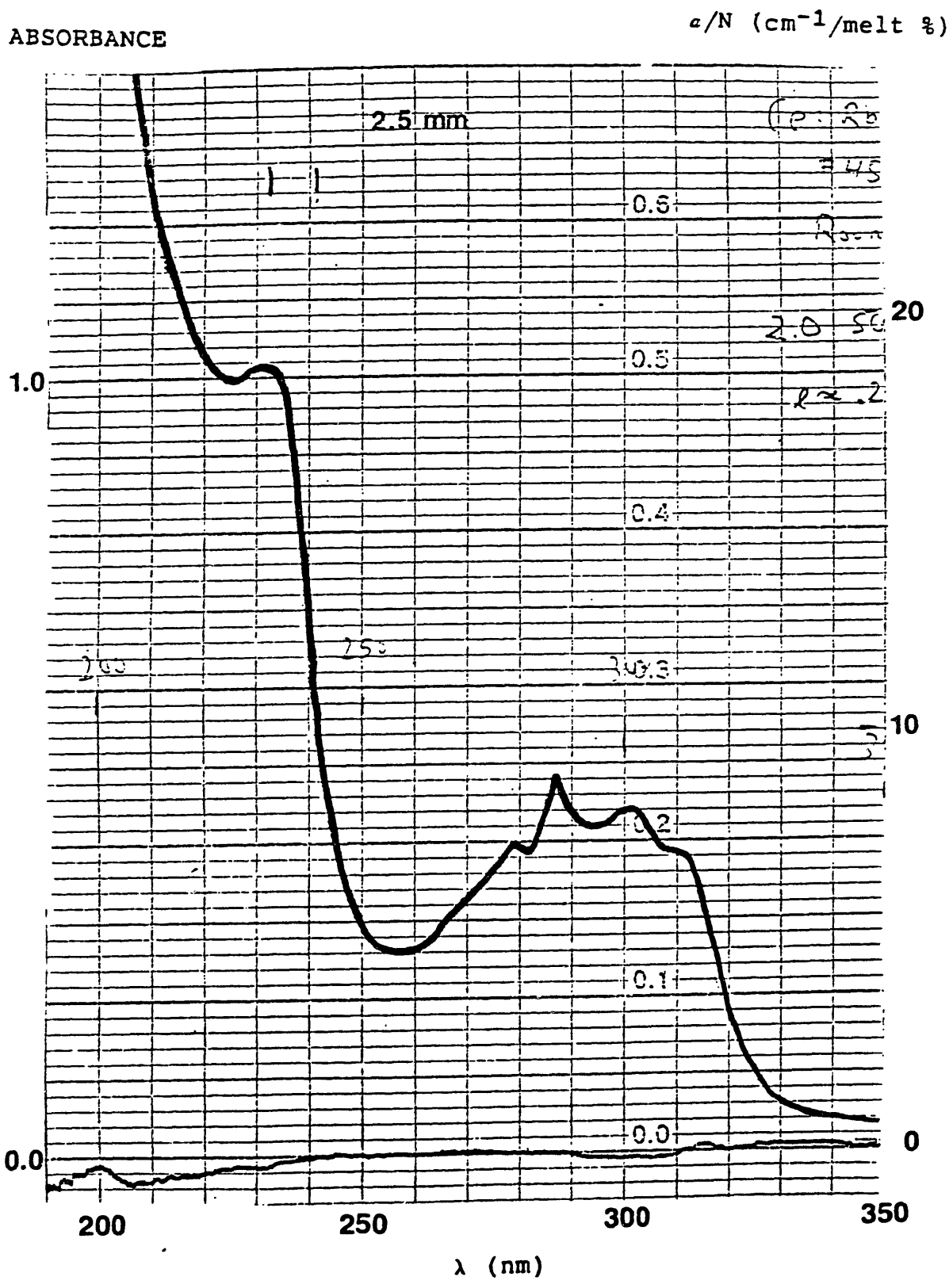

Figure 28 Rb_2NaYF_6:Ce Absorption Spectrum (sample 450F)

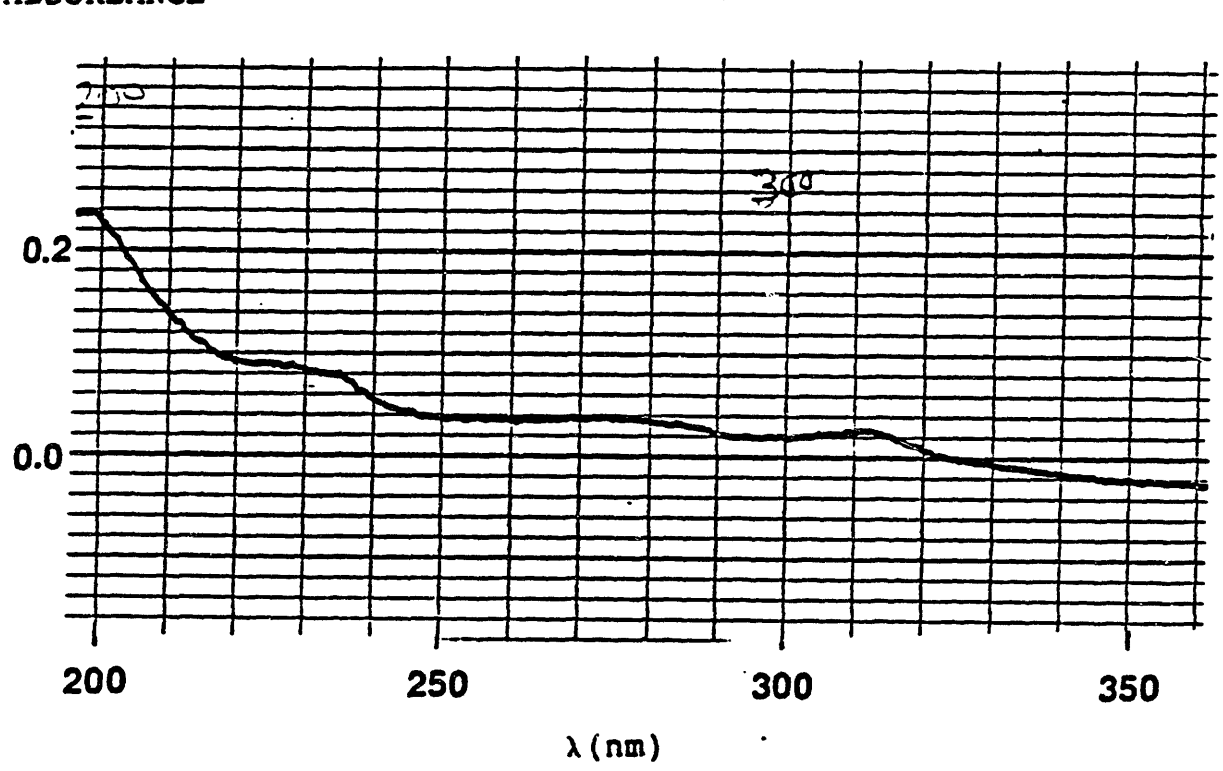

Figure 29 Absorption Spectrum of Undoped Rb_2NaYF_6

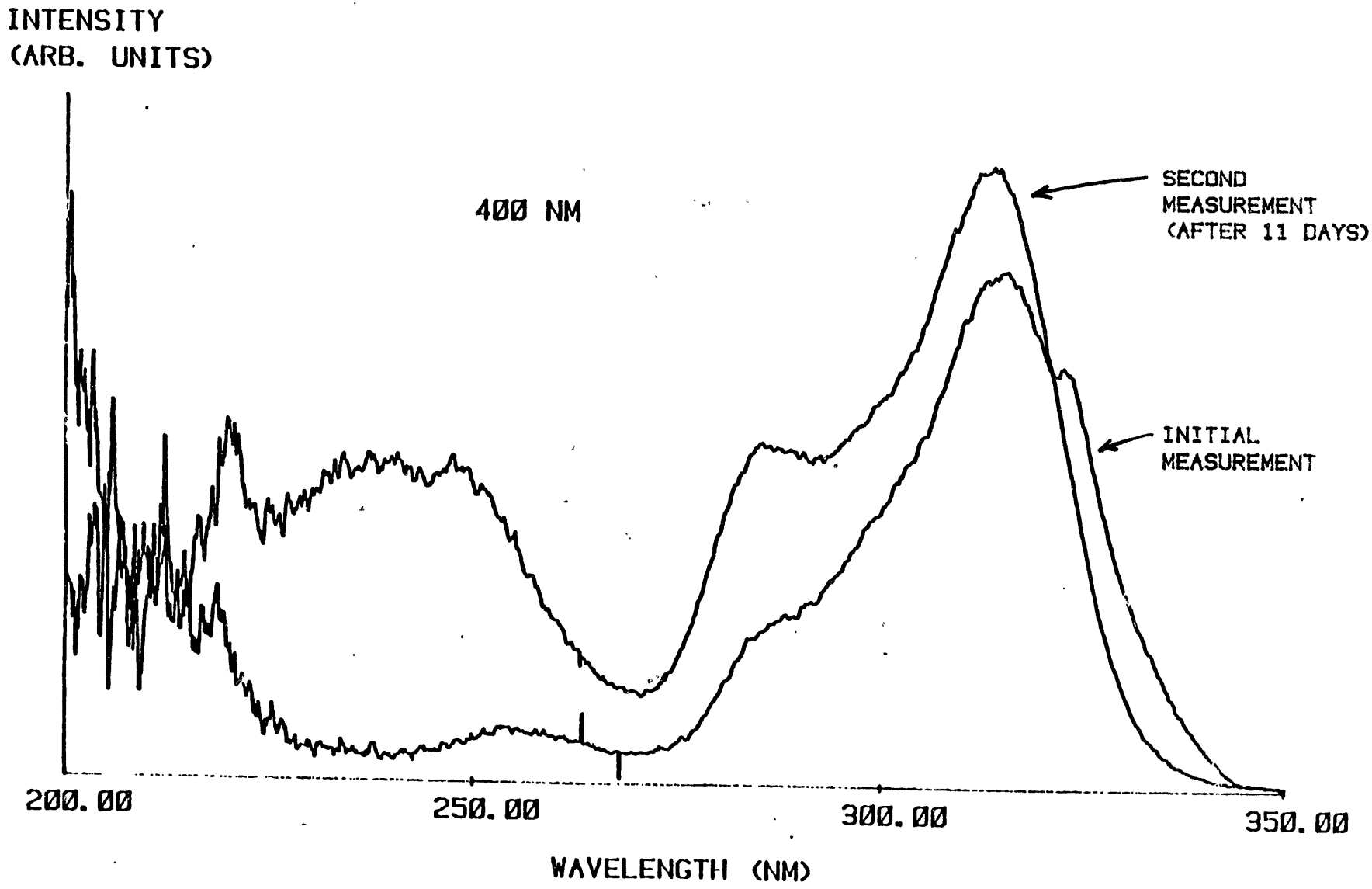

Figure 30 K_2NaYF_6 Excitation Spectra

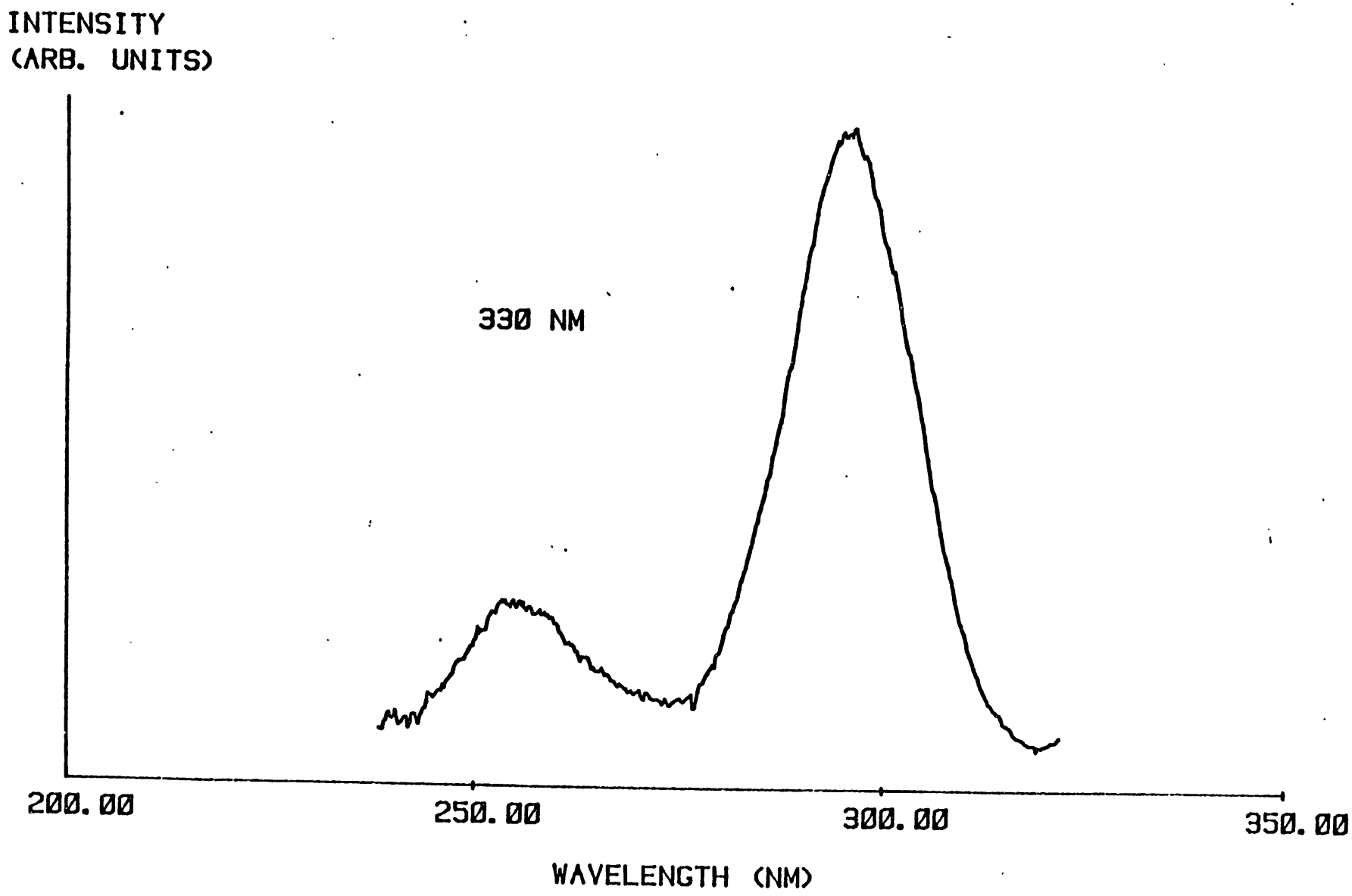

Figure 31 K_2NaYF_6 Excitation Spectrum

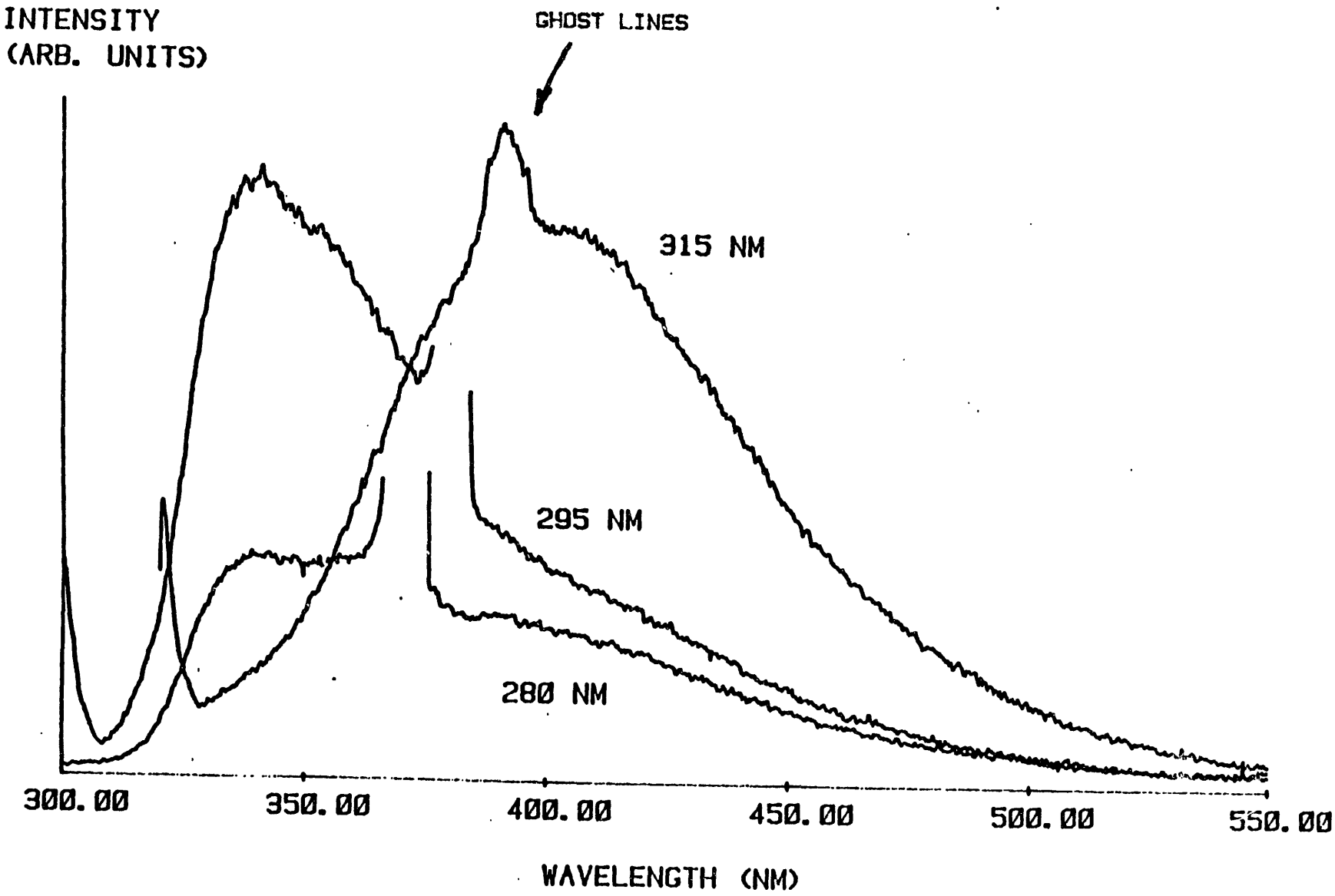

Figure 32 K_2NaYF_6 Emission Spectra

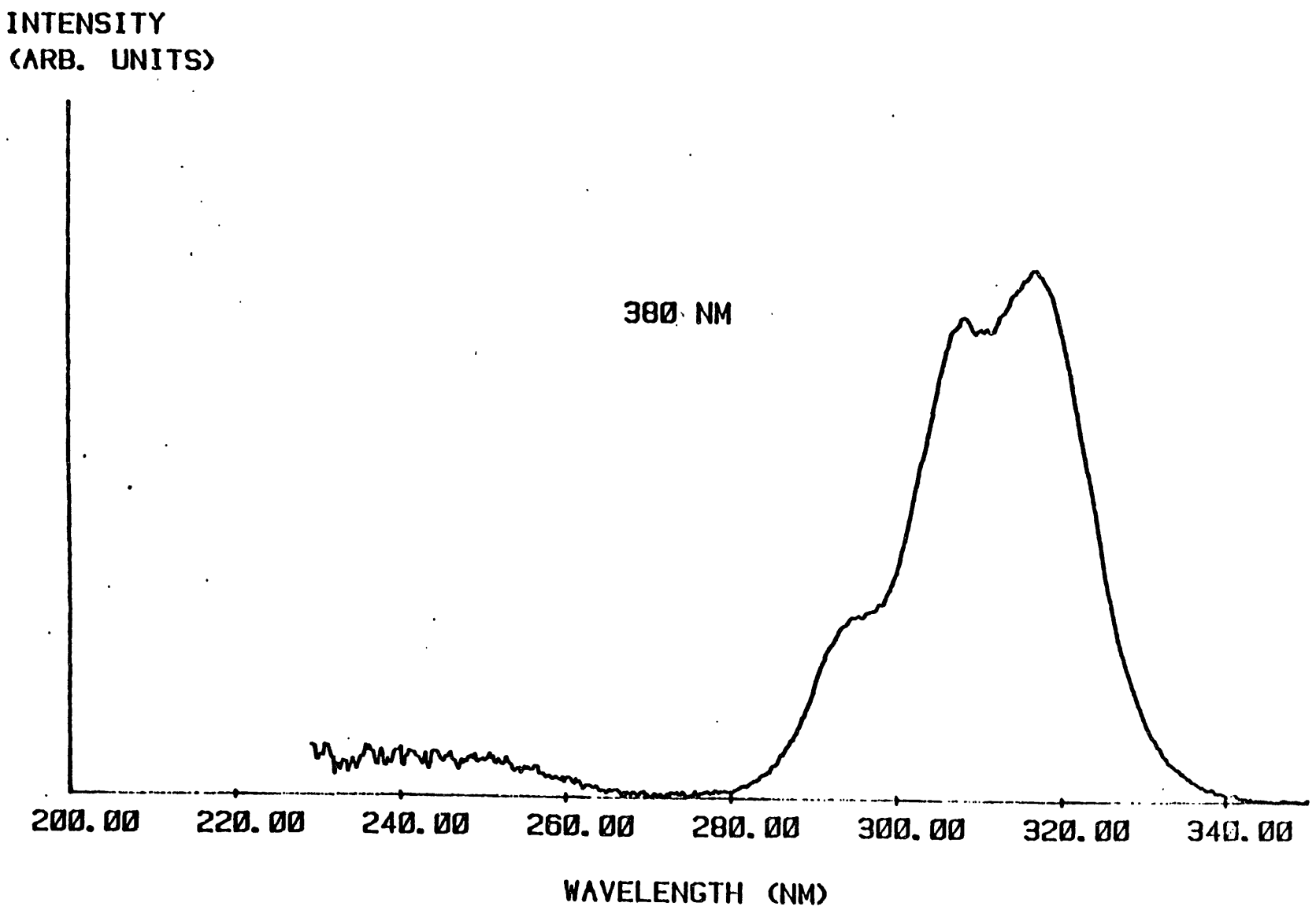

Figure 33 Rb_2NaScF_6 Excitation Spectrum

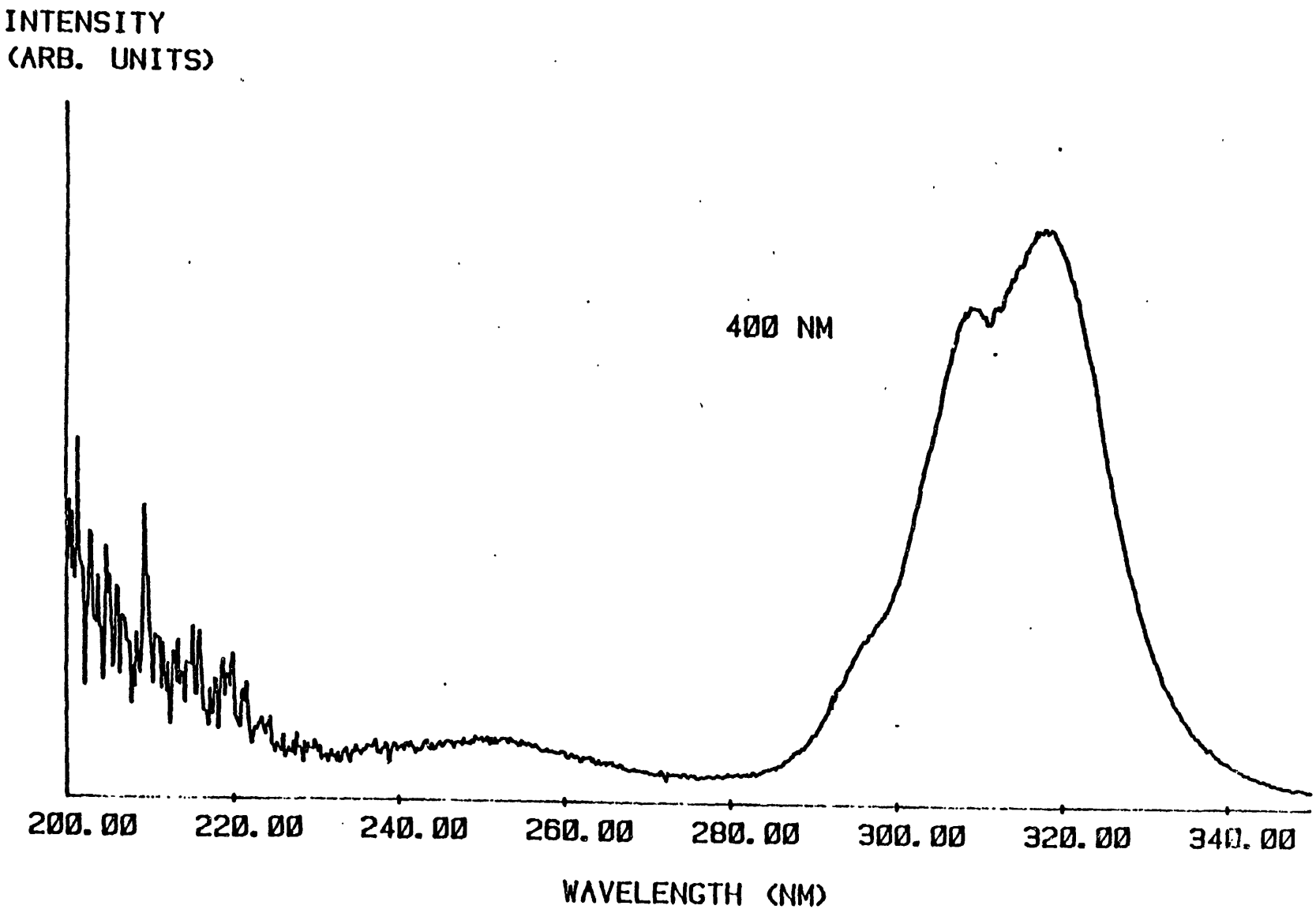

Figure 34 Rb_2NaScF_6 Excitation Spectrum

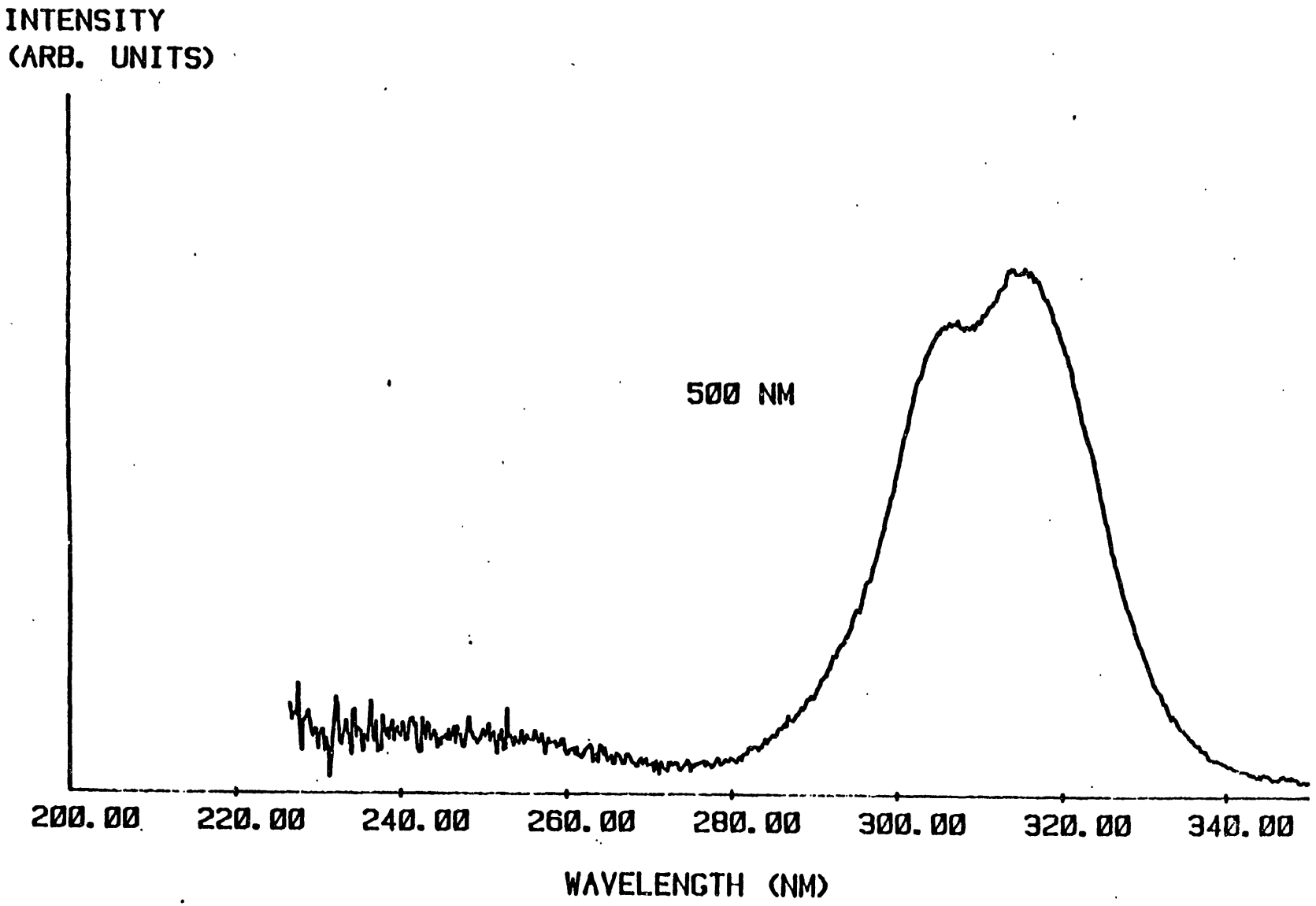

Figure 35 Rb_2NaScF_6 Excitation Spectrum

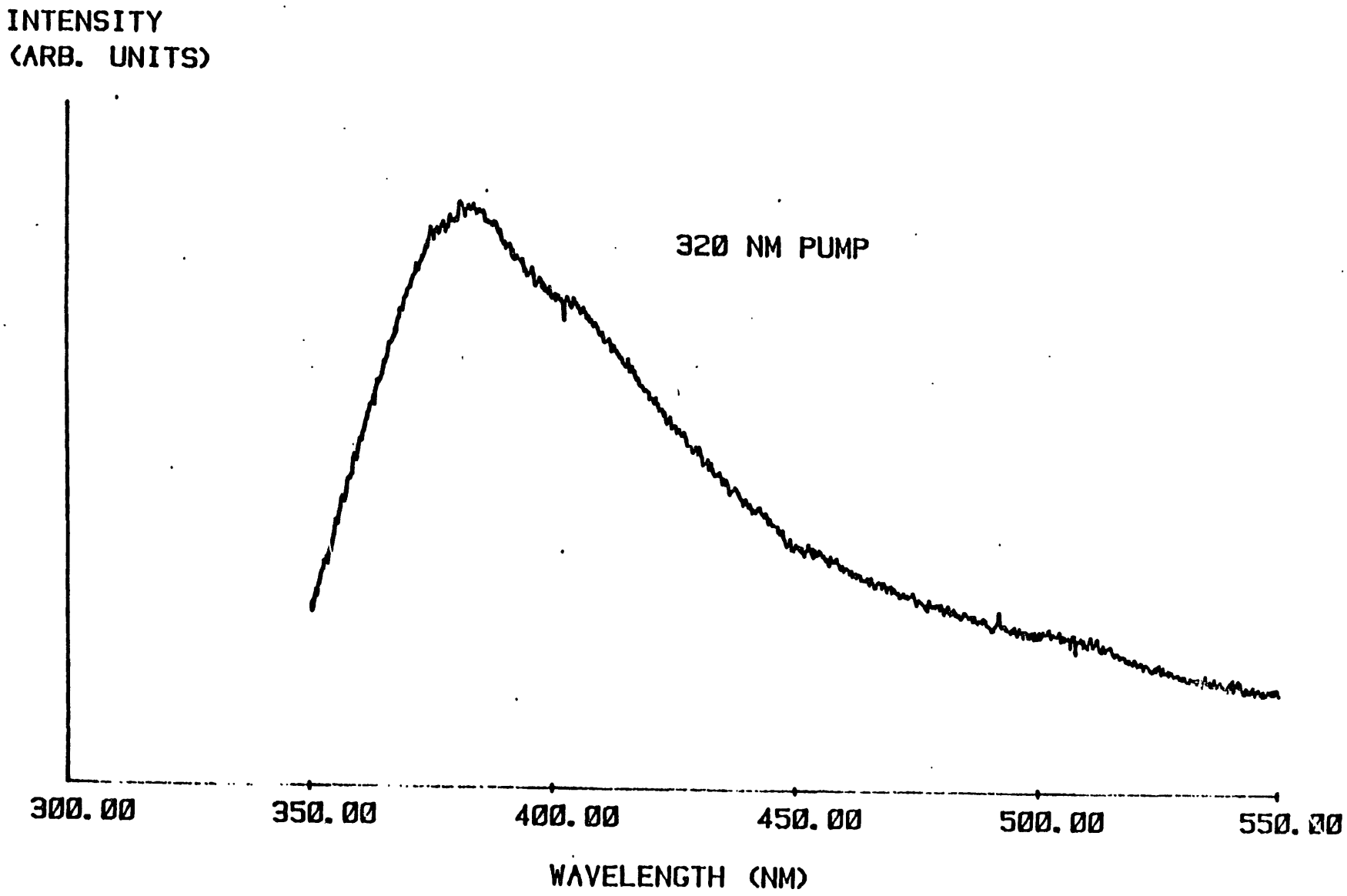

Figure 36 Rb_2NaScF_6 Emission Spectrum

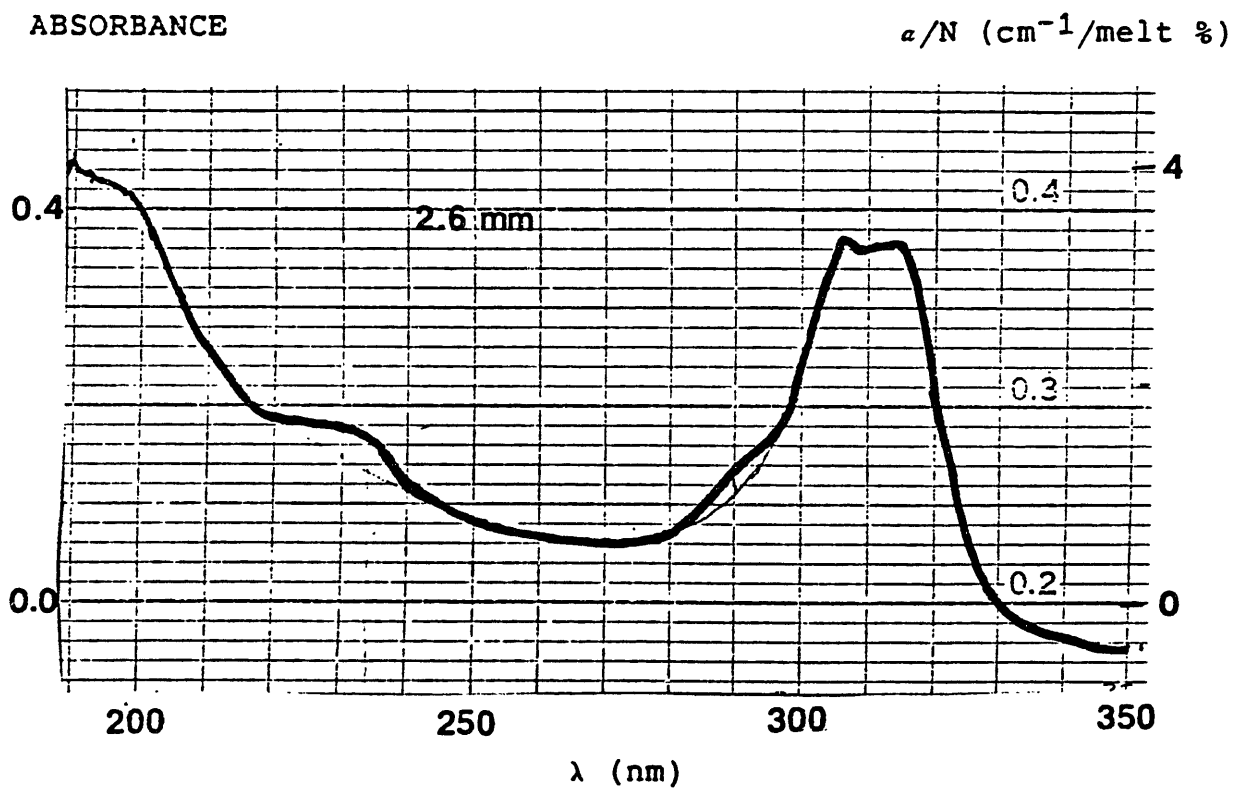

Figure 37 Rb_2NaScF_6:Ce Absorption Spectrum

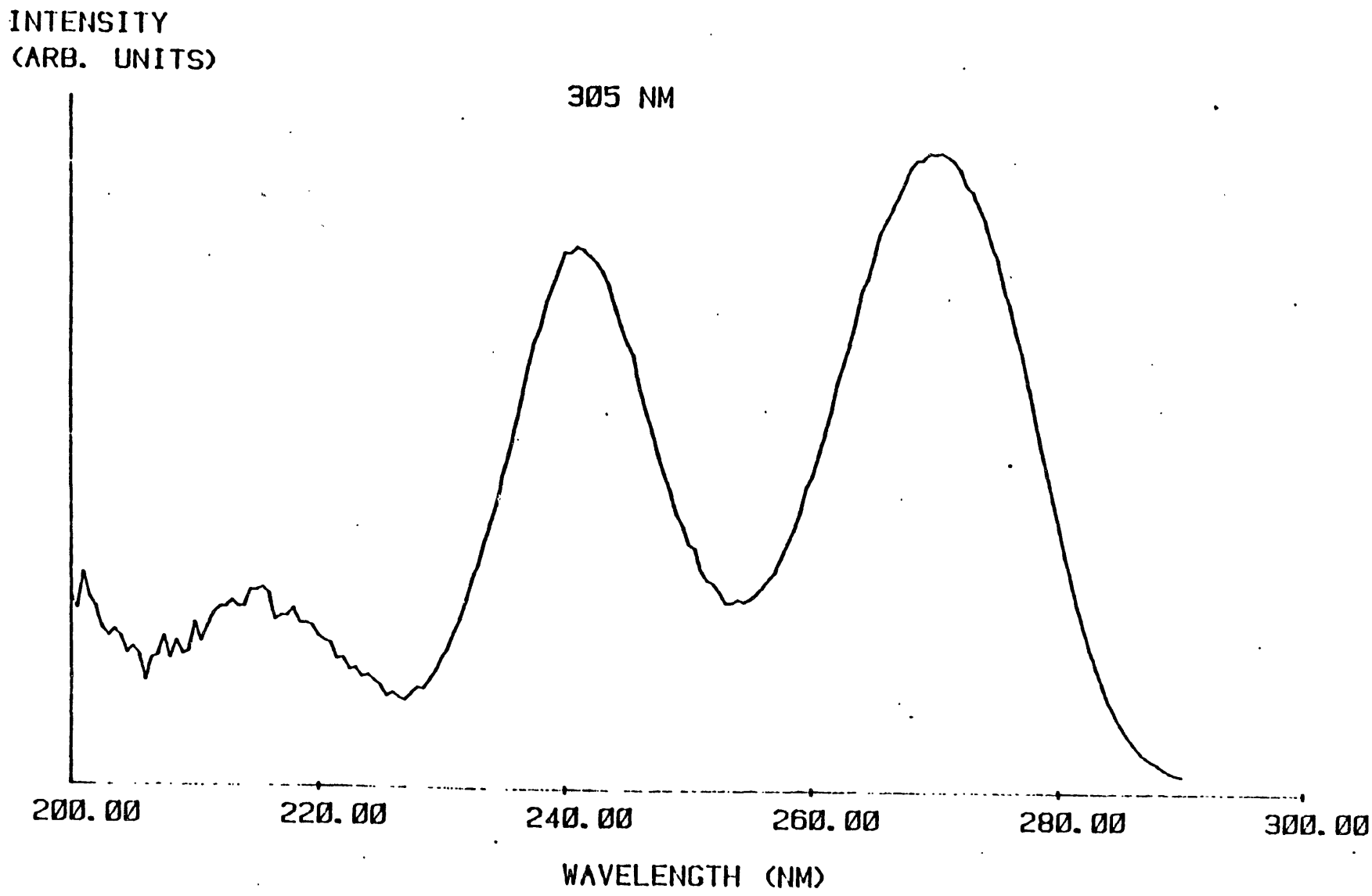

Figure 38 K_2NaScF_6 Excitation Spectrum

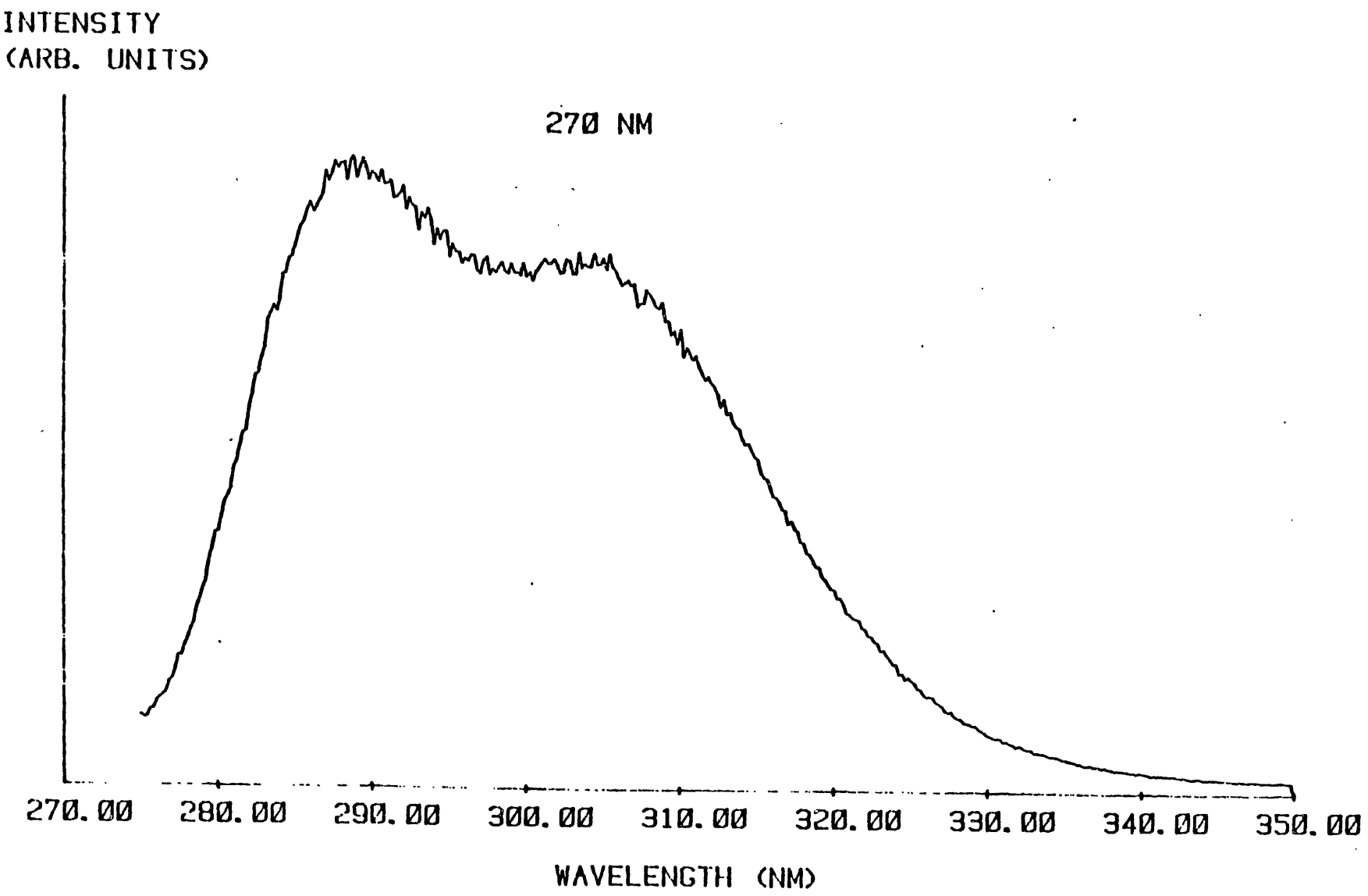

Figure 39 K_2NaScF_6 Emission Spectrum

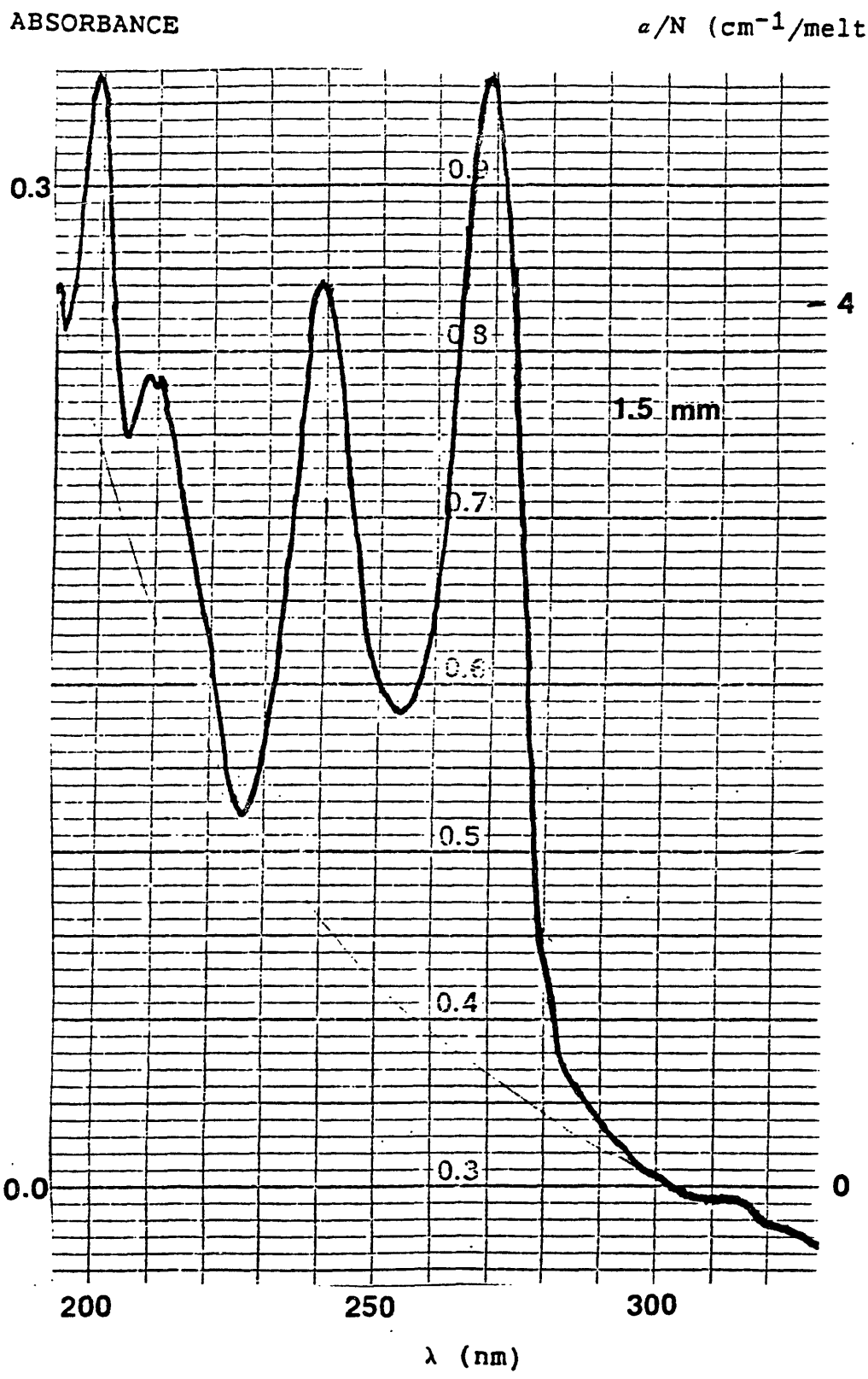

Figure 40 K_2NaScF_6:Ce Absorption Spectrum

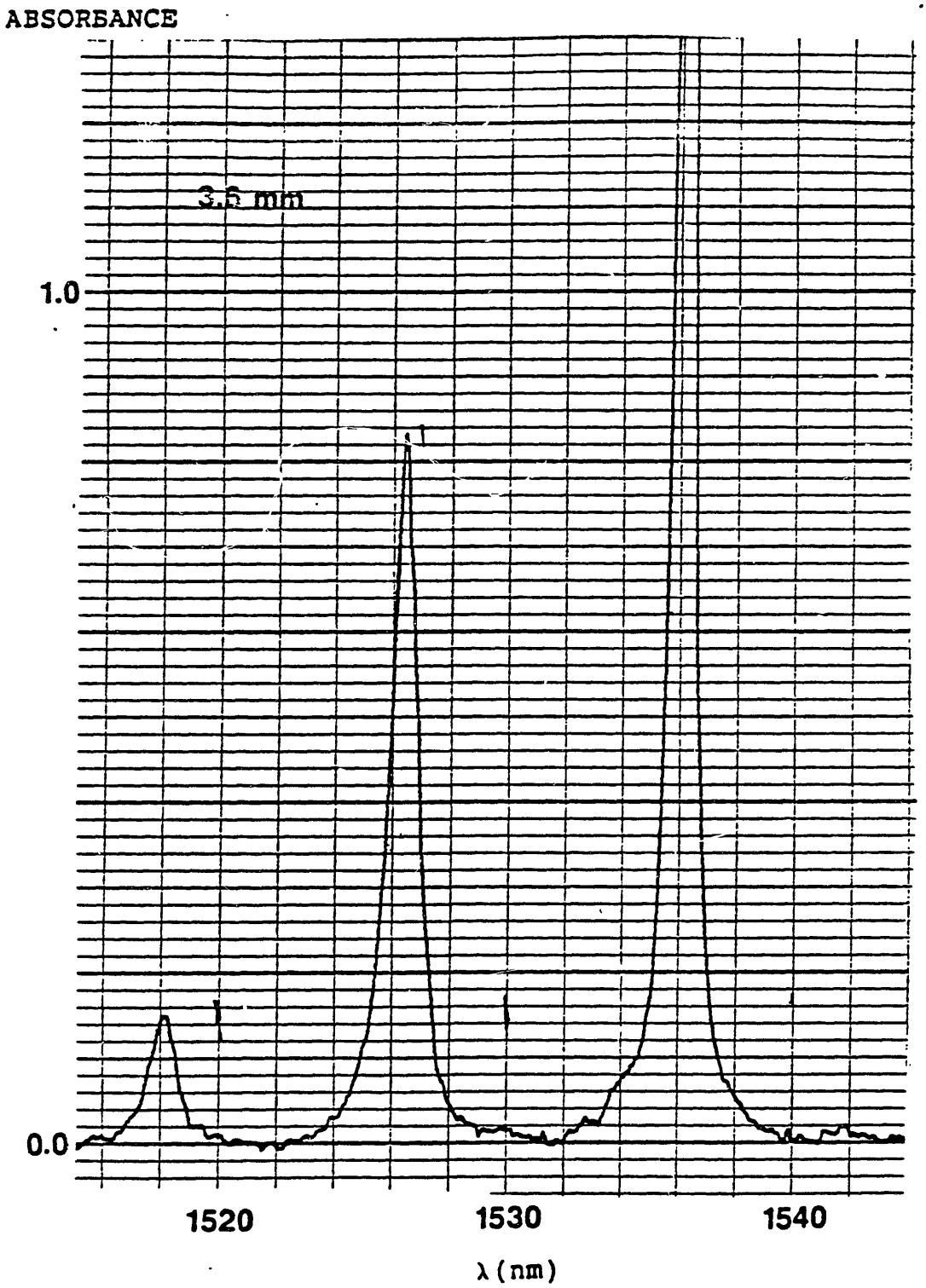

Figure 41 $Er^{3+}:Rb_2NaYF_6$ Absorption Spectrum at 4 K

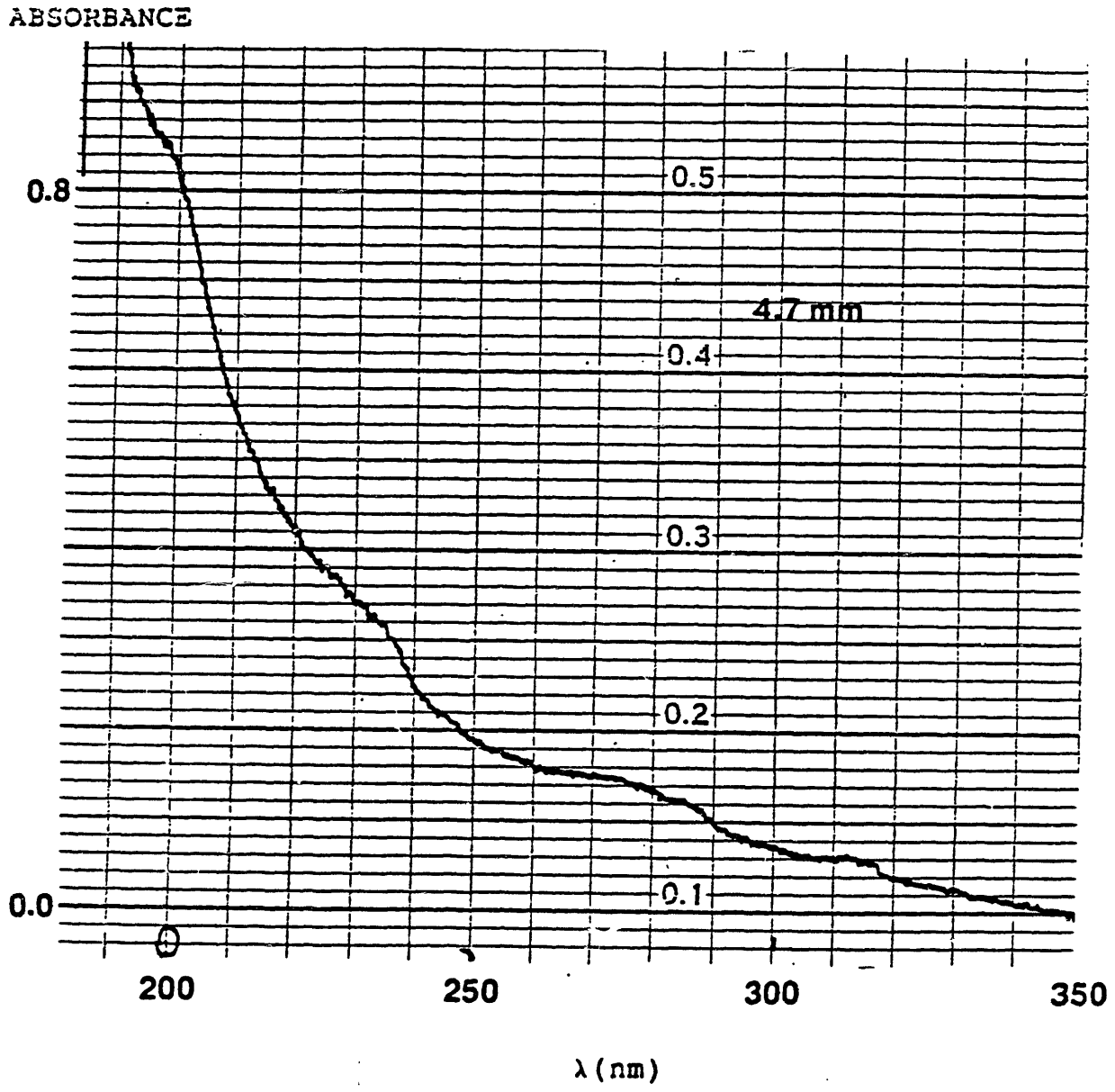

Figure 42 $La^{3+}:Rb_2NaYF_6$ Absorption Spectrum

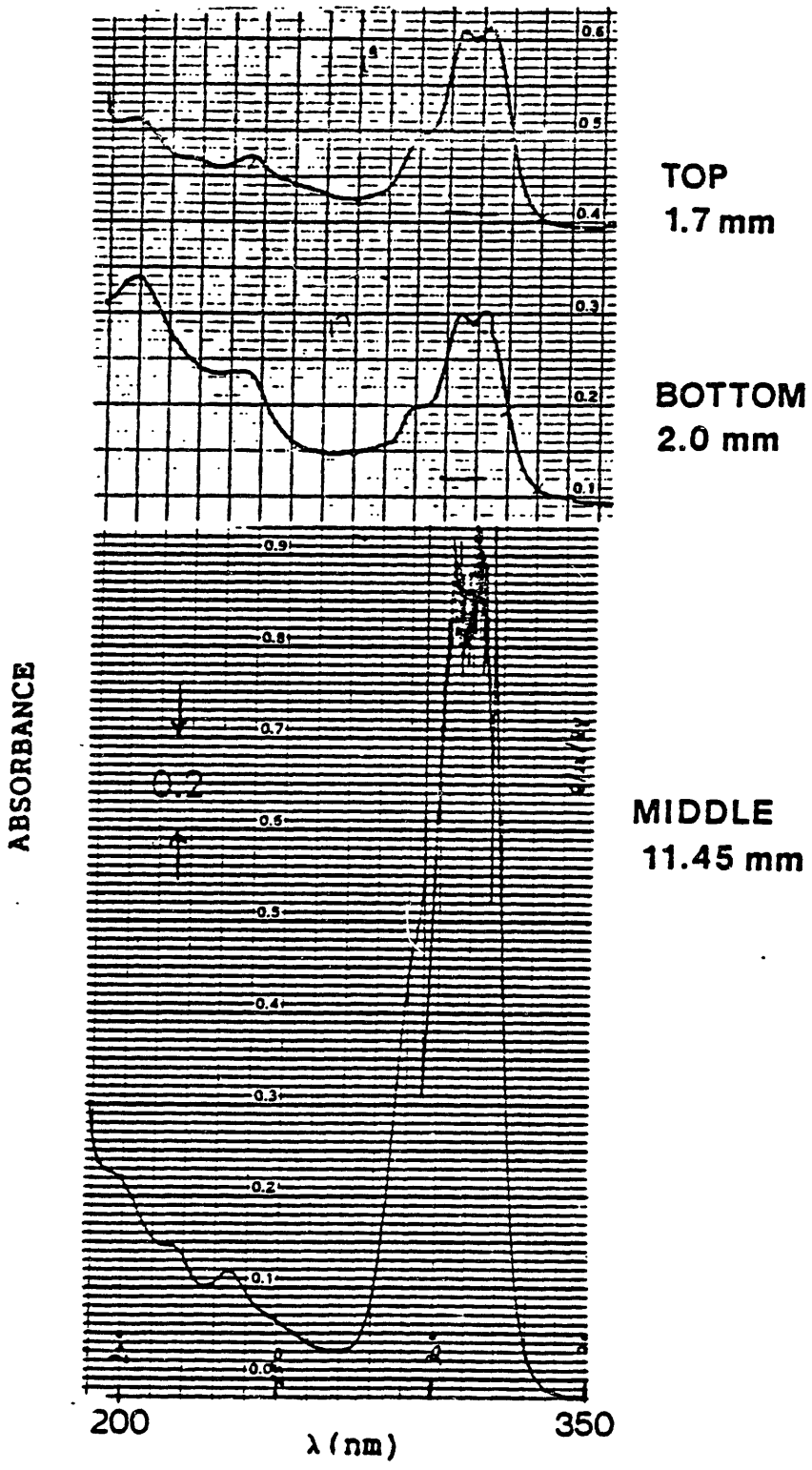

Figure 43 Absorption Spectra from Boule 20B

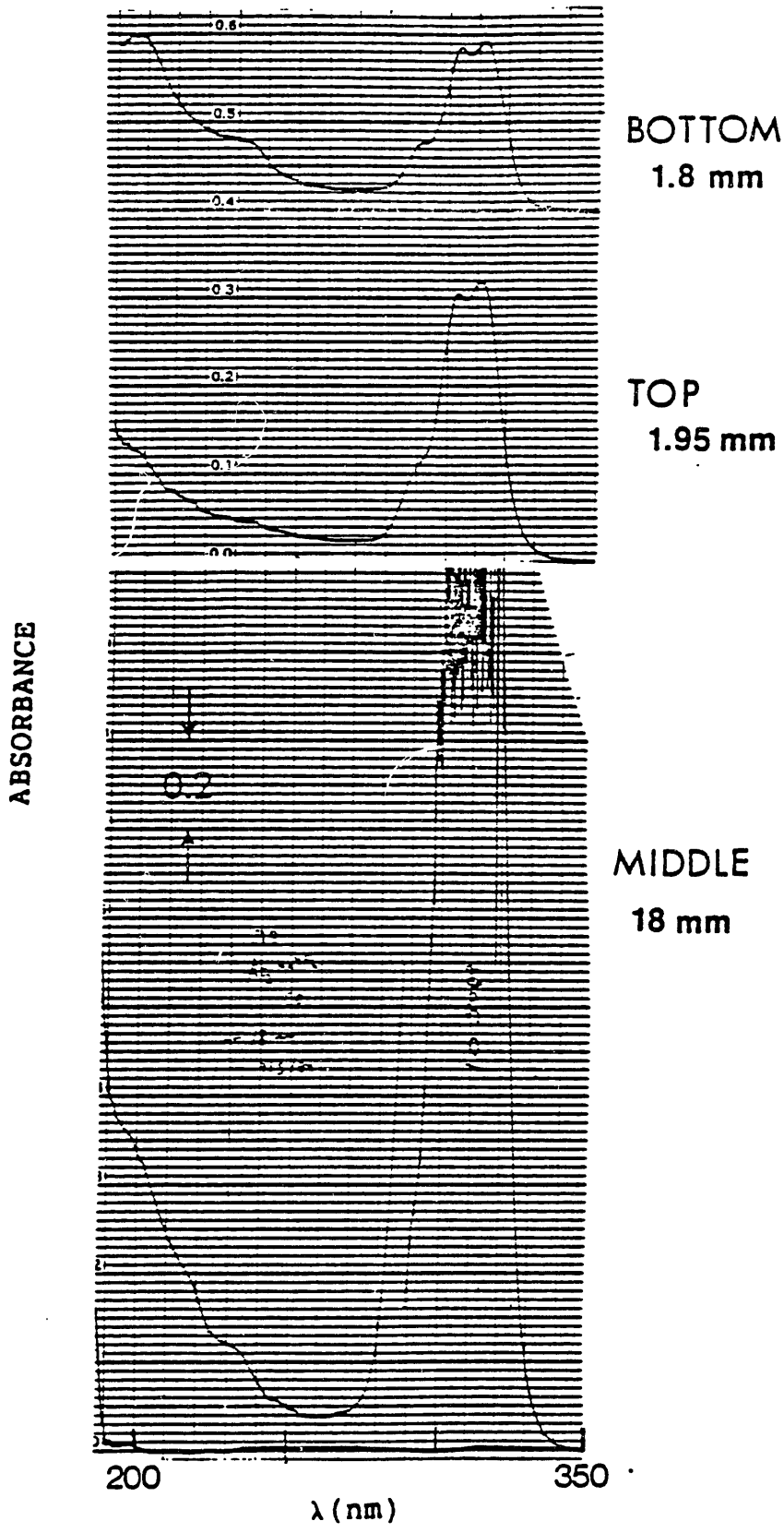

Figure 44 Absorption Spectra from Boule 21B

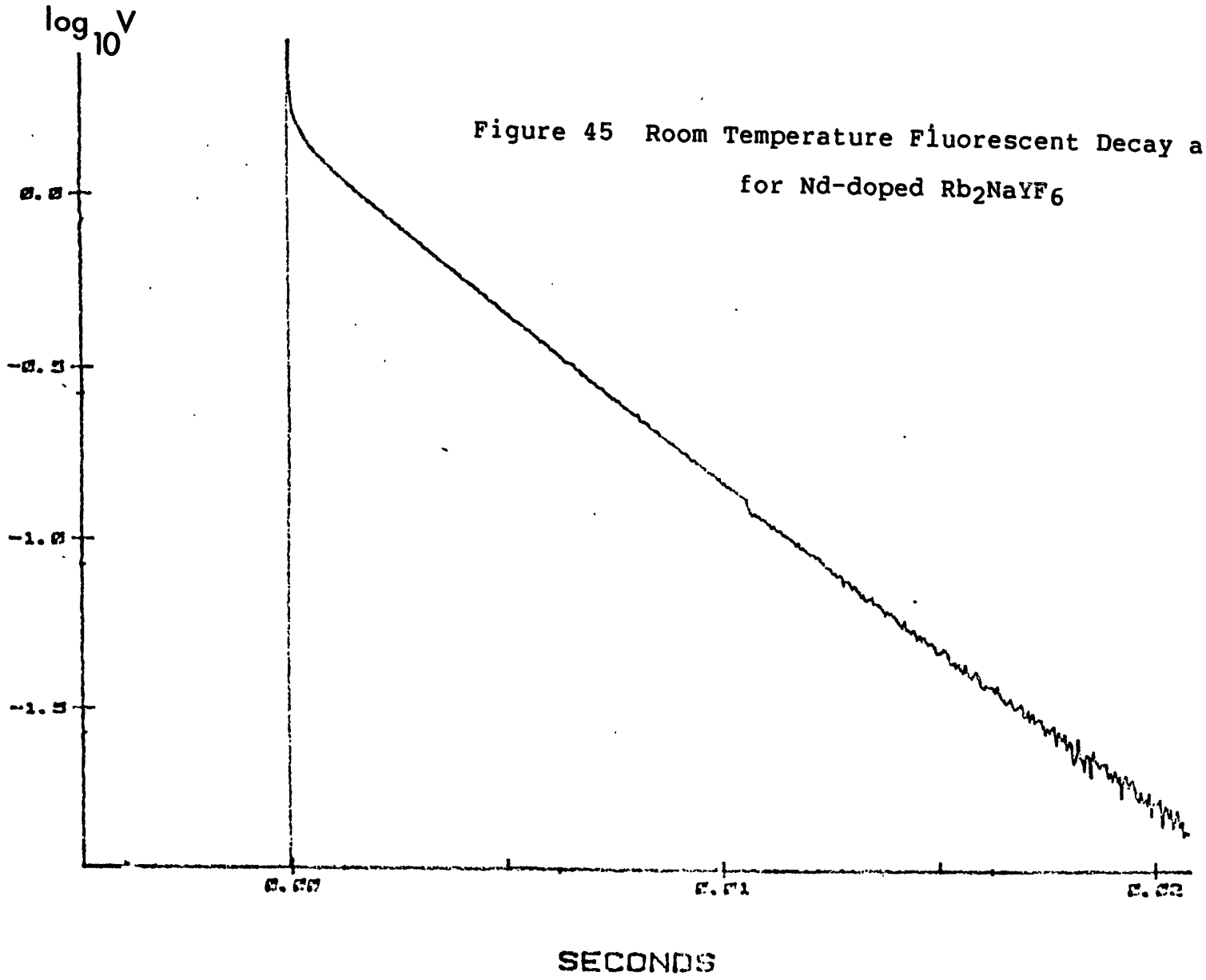

Figure 45 Room Temperature Fluorescent Decay at 1.06 μm for Nd-doped Rb_2NaYF_6

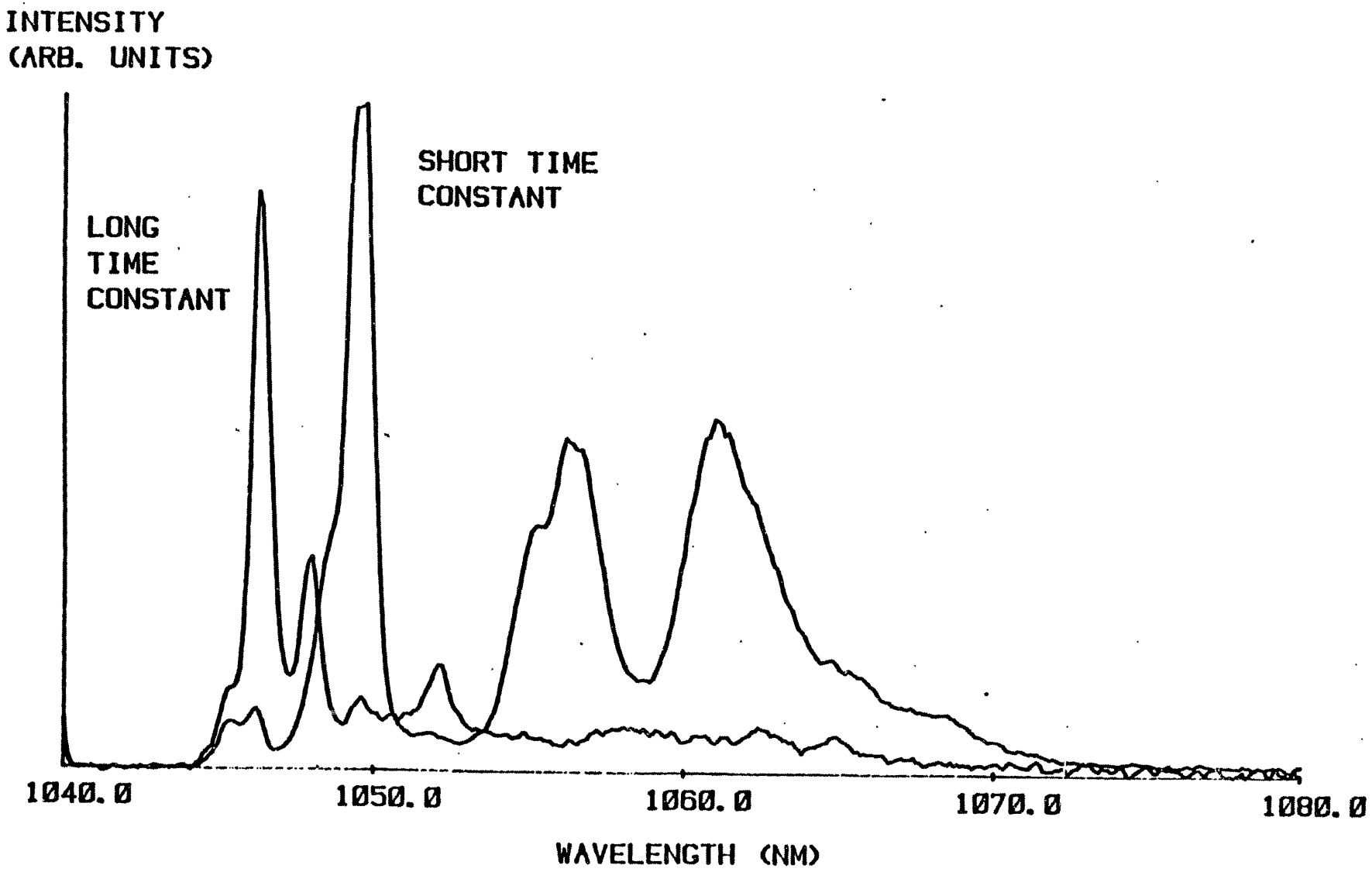

Figure 46 $Nd^{3+}:Rb_2NaYF_6$ Emission Spectrum at 4 K

Figure 47 Ce:Rb_2NaYF_6 VUV Transmission Spectrum

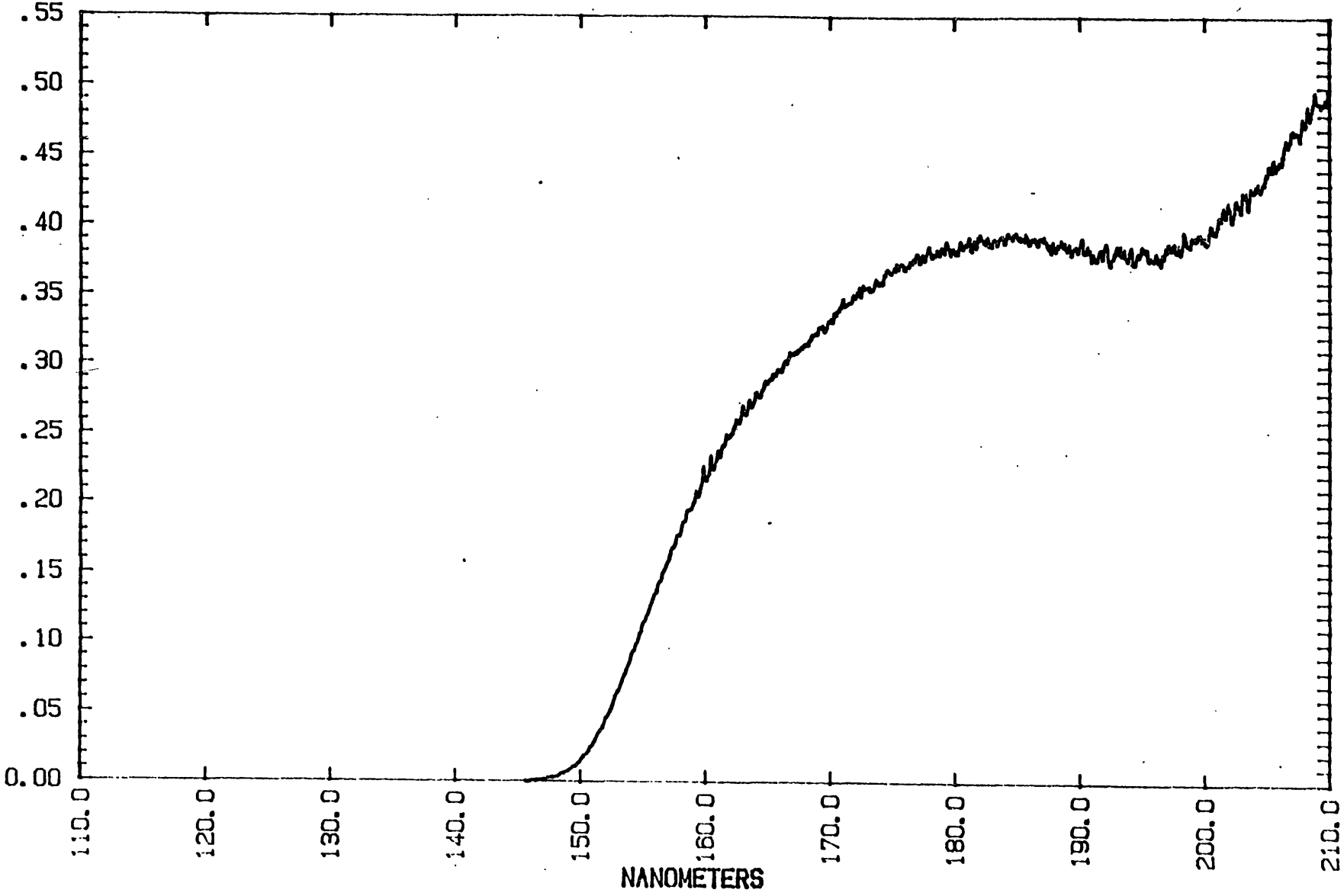

Figure 48 Ce:Rb_2NaYF_6 VUV Transmission Spectrum

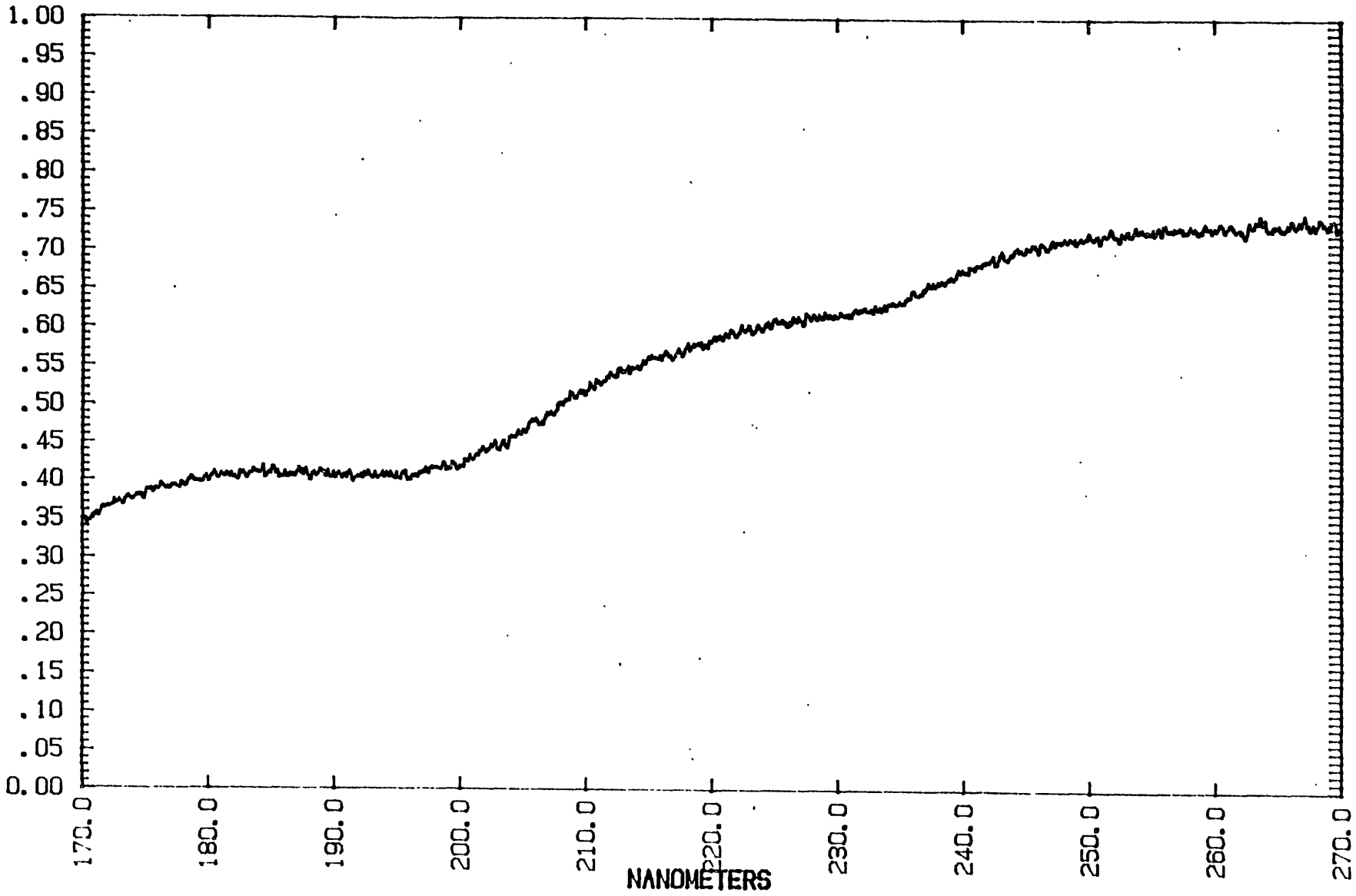

Figure 49 La:Rb_2NaYF_6 VUV Transmission Spectrum

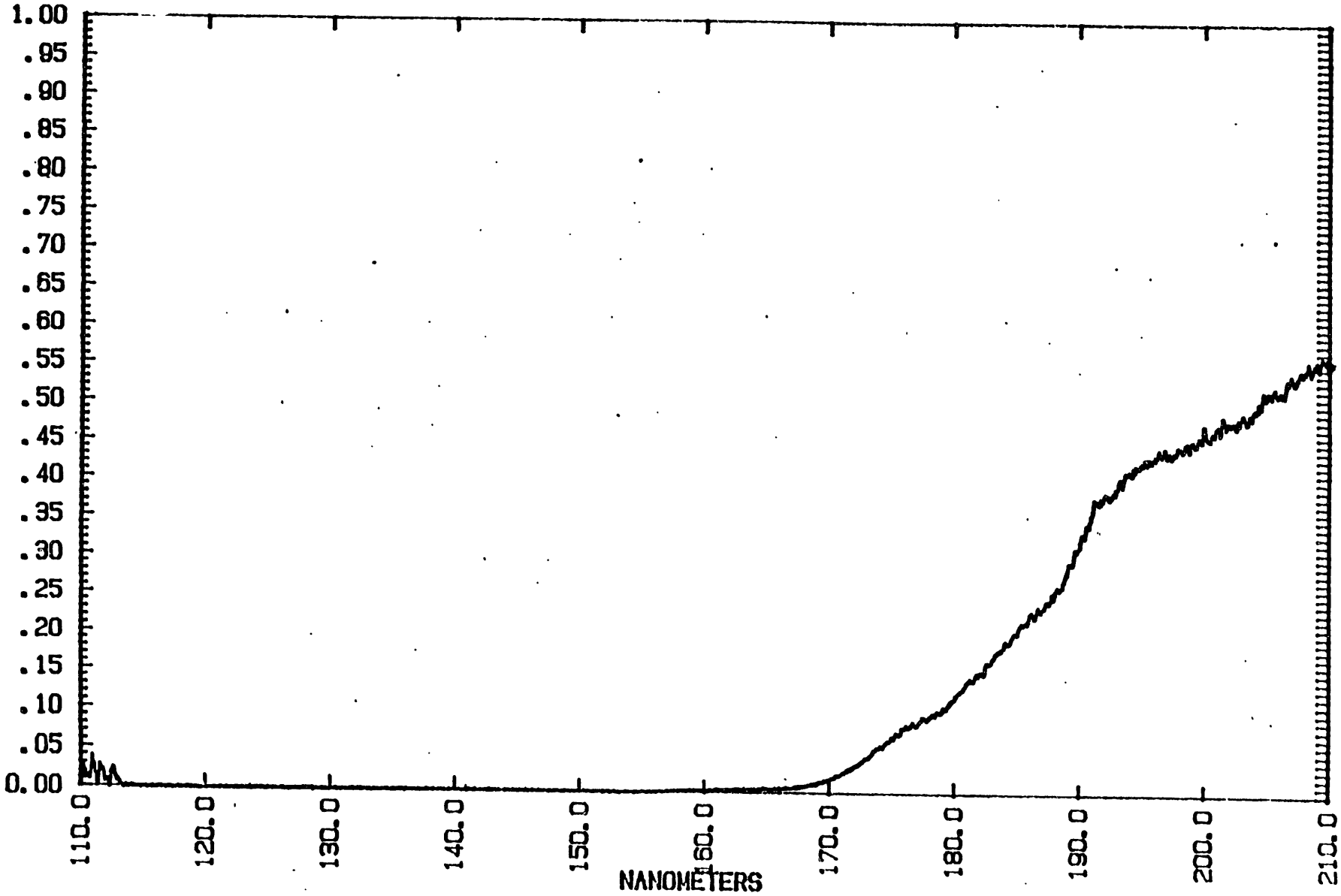

Figure 50 La:Rb_2NaYF_6 VUV Transmission Spectrum

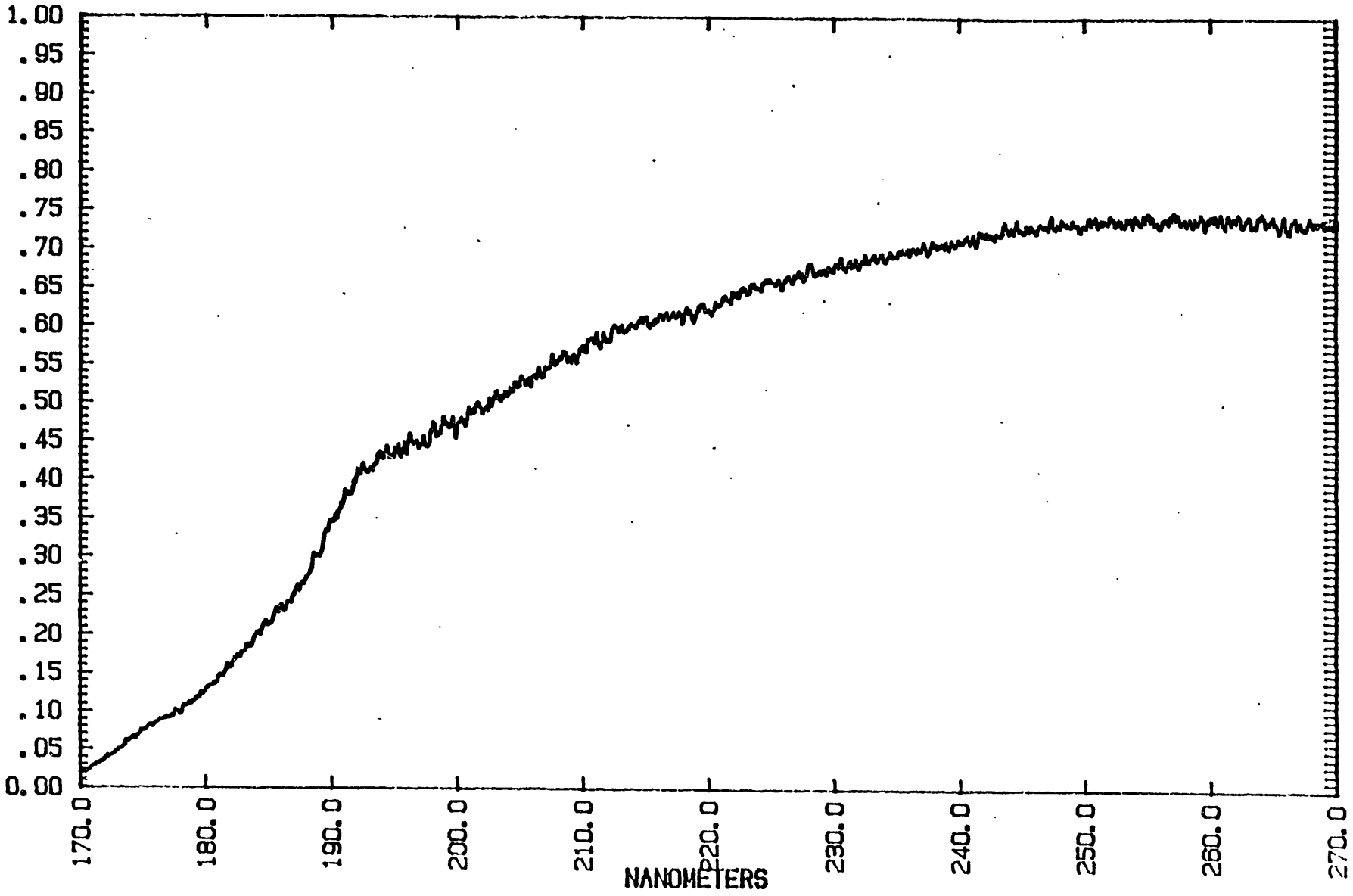

Figure 51 Ce:Rb_2NaScF_6 VUV Transmission Spectrum

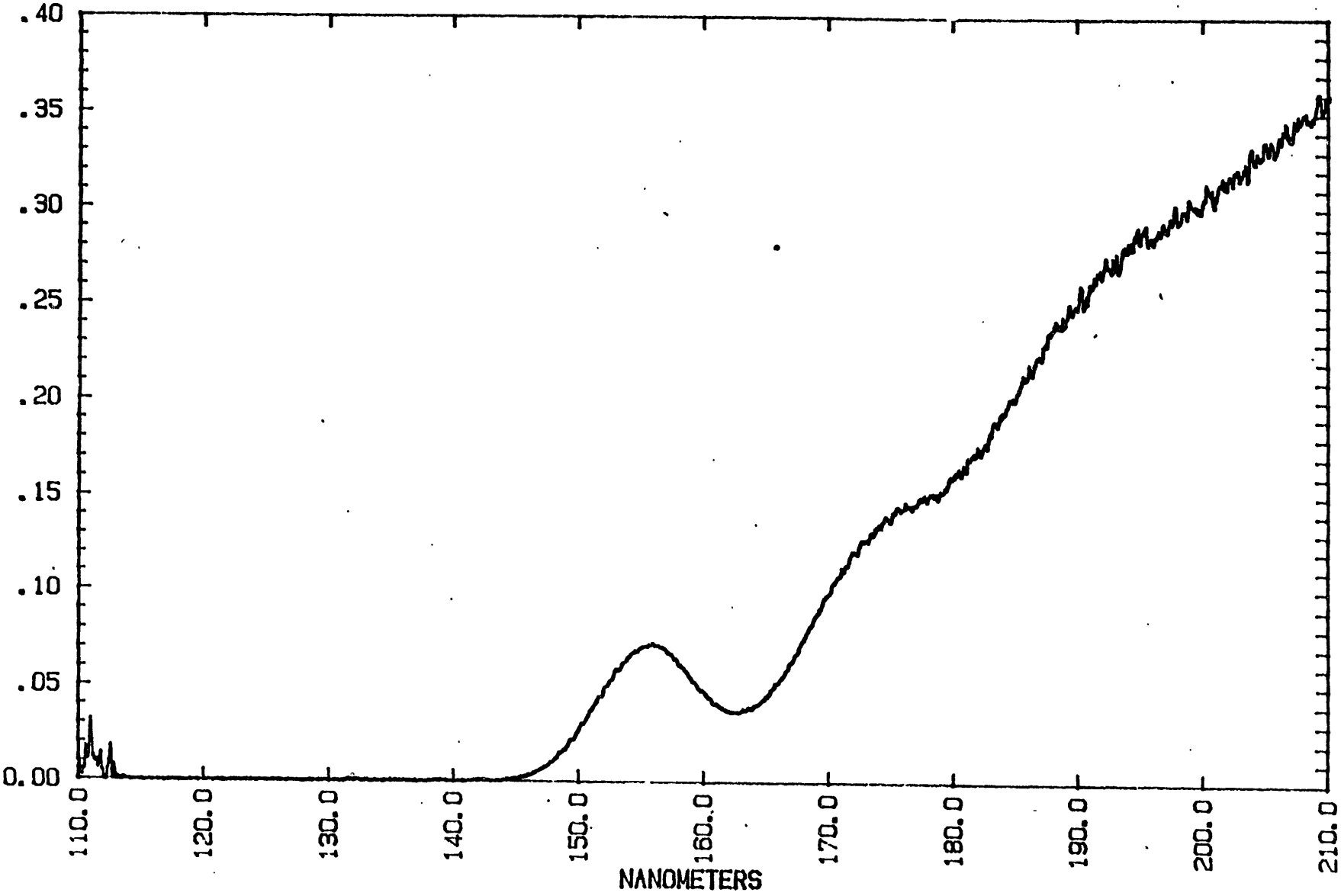

Figure 52 Ce:Rb_2NaScF_6 VUV Transmission Spectrum

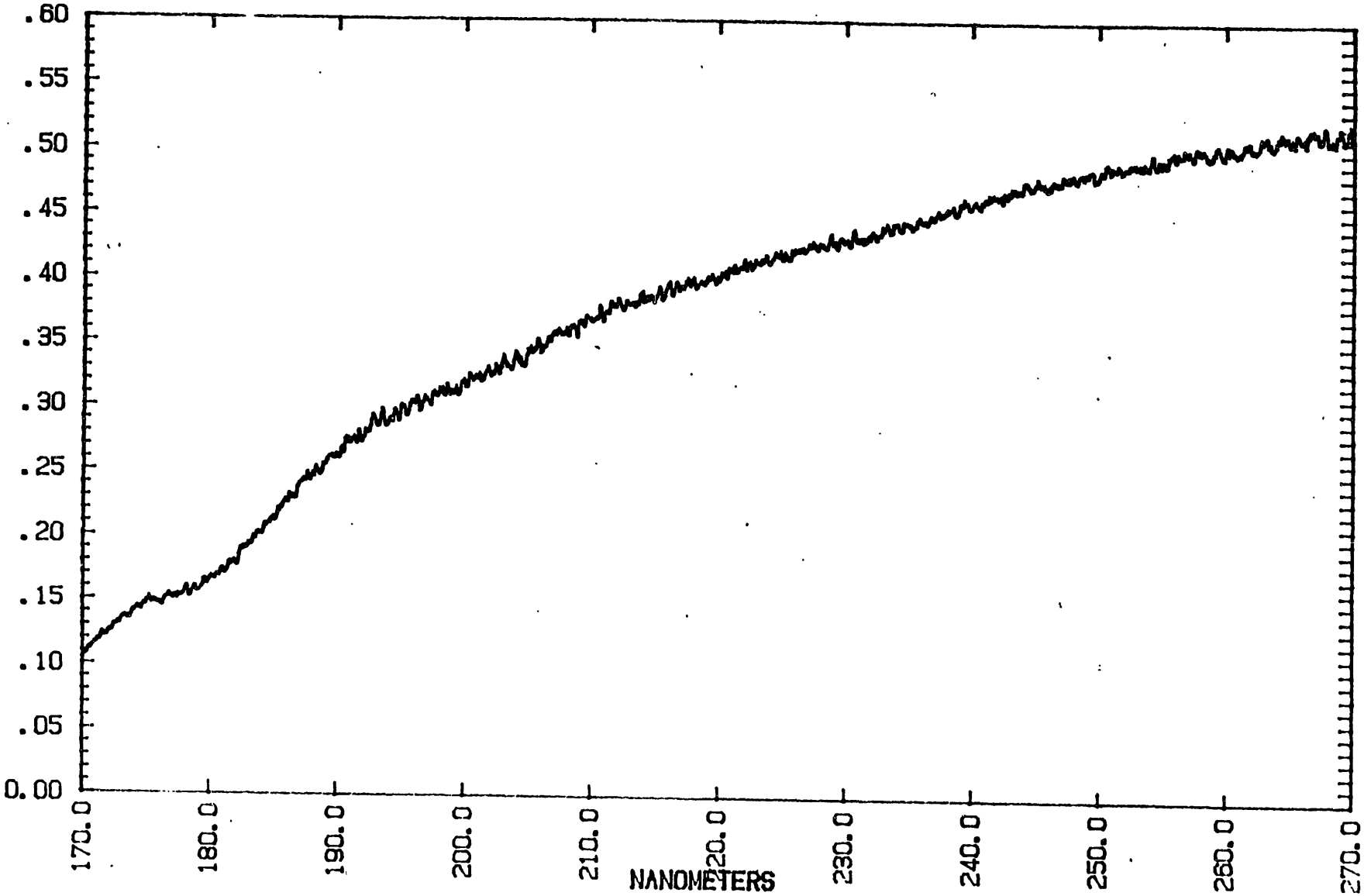

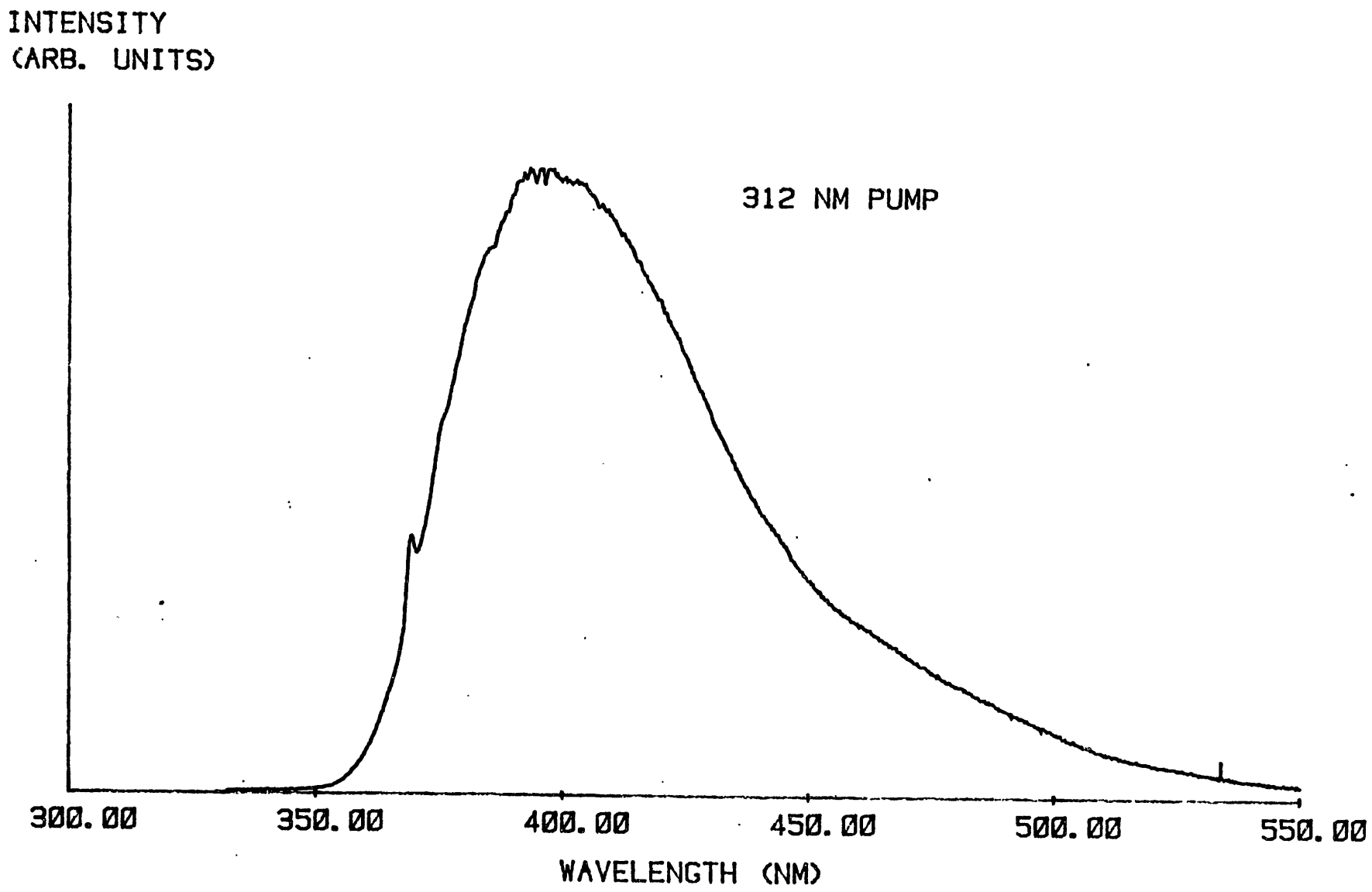

Figure 53 Ce:Rb_2NaYF_6 Emission Spectrum at 4 K

CHAPTER V

RESULTS AND DISCUSSION

5.1 Modeling of the 5d Splittings and Centroids

In order to interpret the spectroscopic results of the last chapter, it is necessary to construct, from the theory of chapter II, a simple phenomenological model. First, it is assumed that the crystal field interactions are dominated by the nearest-neighbor fluoride ions; the rest of the lattice constrains the Ce-F bond distance, and contributes to the field which polarizes the fluoride ions. Table IX summarizes the dependences on Ce-F bond distance R of the contributions to the 5d splitting, 10Dq, and centroid shift, Δ, which are included in our model. (NOTE: The fixed-dipole splitting actually scales as $R^{-6}a^{-2}$, where a is the lattice constant. Thus the R^{-8} entry in the table is based on a linear relationship between R and a.)

TABLE IX Range dependences of contributions to the 5d splitting and centroid shift

	10Dq	Δ
Point charge	$+R^{-5}$	0
Fixed dipole	$+R^{-8}$	0
Self-induced dipole	$-R^{-8}$	$-R^{-6}$
Covalency-overlap-exch	$+\exp(-\beta R)$	$+\exp(-\beta R)$

The first three rows of the table refer to the leading electrostatic and self-induced contributions to the splitting and centroid. These display inverse power law dependences, and are very easy to calculate, given reliable values of 5d radial expectation values and ligand polarizabilities. Covalency, classical overlap, and exchange terms are lumped together as a simple exponential in the fourth row, since they should all be roughly proportional to the square of the metal-ligand overlap integral. These terms are very difficult to calculate, and are sensitive to the wavefunctions used, both on the metal ion and on the ligands. Therefore, the contribution of these terms is best deduced by comparing experimental splittings and centroids to those predicted using the electrostatic and self-induced terms.

One difficulty which remains is that our experiments did not determine the symmetries of the 5d levels identified

in absorption spectra, and therefore the sign of 10Dq is undetermined. Although the point charge and covalency contributions are positive, the Sugano and Shulman results indicate that the classical overlap and exchange give sizable negative contributions (Table I). If the covalent contribution for Ce^{3+} turns out to be small, this could reverse the sign of the splitting.

To remove the doubt about a positive 10Dq, we turn to Phillips [62], who pointed out that even without covalency (γ=0 in Equation 16), metal-ligand overlap gives rise to the "non-orthogonality" and "renormalization" terms shown in Table I. Using the wavefunction of Equation 19, Phillips argued on general grounds that these terms give rise to an effective repulsion which approximately cancels the classical overlap and exchange. Physically, this is Pauli repulsion, since the necessity of orthogonalizing Ψ_b and Ψ_a is a reflection of the Pauli principle. Indeed, in Table I, the sum of the classical overlap, exchange, renormalization, and non-orthogonality terms is $-330\ cm^{-1}$, or 5% of the splitting. Although Phillips applied this argument to the splitting, the cancellation of terms affects the energy eigenvalues of the individual levels, and therefore applies to the centroid as well. Thus the terms in the fourth row of Table IX are both assumed to be positive and dominated by covalency. The covalent contribution to the 5d splitting is given by the difference between the σ and π antibonding energies, and the covalent contribution to the centroid is

given by a degeneracy-weighted average of these energies.

For an octahedral $(CeF_6)^{3-}$ complex, Figure 7a in chapter II qualitatively depicts the dependence of the 5d energies on bond distance. At large R, the centroid drops with an R^{-6} dependence as the complex is compressed, because of the isotropic self-induced dipole effect (Equation 15). When overlap becomes significant, covalency makes a positive, exponentially increasing contribution. At large R, the splitting is positive, and increases as the complex is compressed. In elpasolite the fixed dipole contribution is slightly larger than the self-induced dipole contribution, so the increase in the splitting contains both an R^{-5} and an R^{-8} term. As overlap becomes significant, covalency contributes an exponentially increasing and positive term, causing the splitting to increase even more rapidly. An important feature of the t_{2g} level in Figure 7a is that it displays a minimum.

Table X lists the lattice constants, t and e levels, splittings and centroids for the elpasolites. The e level was not obtained for K_2NaYF_6 because the samples were polycrystalline and VUV transmission measurements were not feasible.

TABLE X Experimental 5d energies in elpasolites

HOST	a(A)	$E(t_{2g})$	$E(e_g)$	10Dq	Δ
Cs_2NaYF_6	9.056[40]	32000[57]			
Rb_2NaYF_6	8.869	32500	50700	18200	-13163
K_2NaYF_6	8.72	31700			
Rb_2NaScF_6	8.60	32000	58800	26800	-10223

Values of the 5d-4f centroid shift Δ are based on a free ion centroid difference of 49943, and a 4f centroid which is 3000 cm^{-1} above the ground state in the elpasolites. (See Table XVI.)

The t level listed for Cs_2NaYF_6 is based on an excitation spectrum of a polycrystalline sample by Chang [57]. In Rb_2NaYF_6 the centroid of the high-energy absorption band is estimated to be 197 nm, and in Rb_2NaScF_6 the centroid of the double-peaked band is estimated to be 170 nm. As pointed out in Chapter II, such an asymmetrical double-peaked band is expected for a strong E-e Jahn-Teller effect, but the band centroid is a good estimate of the electronic transition energy for the undistorted complex [31].

We now compare these results to the predictions of a totally ionic model. Morrison [63] performed a lattice sum to calculate the 5d splitting in Rb_2NaYF_6, using the radial expectation values of Grossgut [64]. The first column of Table XI shows the results for a fluoride polarizability of

1 A^3. The second column shows the 5d-4f centroid shift for the same polarizability.

TABLE XI Calculated contributions to 10Dq and Δ in Rb_2NaYF_6

	10Dq	Δ
Point charge	17328	
Fixed dipole	9660	
Self-induced dipole	-7216	-9319
TOTAL	19771	-9319
EXPERIMENTAL	18200	-13163

The lattice sum overestimates the splitting by about 8%, and underestimates the centroid drop by 29%, leaving no room for the positive covalent contributions anticipated by our model. Thus a conservative estimate for the covalent contribution to the 5d energies is zero. This presents a problem, however. The t level in Table X remains relatively constant as the lattice parameter decreases, although the splitting increases. According to our model, as depicted in Figure 7a, if covalency is negligible, the t level should be dropping as the lattice parameter decreases. The insensitivity of the t level to lattice parameter suggests

that these elpasolite sites lie near the minimum of the t_{2g} curve. In this regime, covalent contributions are clearly not negligible.

This warrants estimation of the amount of stretch sustained by the fluoride octahedron as a result of the incorporation of the oversized Ce^{3+} ion in the Y^{3+} site. Fainstein et. al. [65] calculated impurity-ligand distances for Eu^{2+} in the fluorite lattices. For the small site in CaF_2, the nearest-neighbor distance increases by 0.08 A, 80% of the increase in cation ionic radius, and the next-nearest-neighbor distance only increases by 0.01 A. These calculations were confirmed by strain-induced hyperfine shifts. On this basis we propose the following "stretch model" for the elpasolites. In all the elpasolites in Table X, the second-nearest neighbor in the radial stretch direction is always sodium. We will assume that the Na^+ ion remains fixed, and that the F^- ions expand so that the Na^+-Ce^{3+} distance is divided up according to the ratios of the ionic radii. That is, the Ce-F bond distance x is given by

$$x = (a/2)(r_{Ce}+r_F)/(r_{Ce}+r_F+r_{Na}) \qquad (35)$$

Since the same formula applies to all the elpasolites under study, the bond distance x is proportional to the lattice constant a. A slight rotation or angular distortion of the octahedron may occur, but this would be in addition to the

radial expansion, since the expansion is necessary to reduce the Ce-F repulsion energy.

For Rb_2NaYF_6, (35) yields x=2.2478 A, and for Rb_2NaScF_6, x=2.1795 A. The use of a stretched bond distance requires that a greater polarizability be assumed for the fluoride ion in order to fit the centroid shift. Therefore, the issue of what polarizability to use must be explored.

As noted previously, anion polarizabilities decrease when the anions are put in crystalline environments. Table XII summarizes several theoretical estimates of the F^- polarizability in crystals.

TABLE XII Calculated in-crystal polarizabilities for F^- (A^3)

Mahan [21]	0.69 (NaF)
Schmidt et. al. [66]	0.73 (Watson sphere model)
Fowler and Madden [67]	0.91 (LiF)
	1.12 (NaF)
Wilson and Curtis [68]	1.56 ("Model I")
	1.83 ("Model II")

The values vary from 0.69 to 1.83 A^3, and Fowler and Madden [67] propose a value of 2.31 A^3 for the isolated ion. The values in Table XII are based on isotropic or spherically averaged crystal fields, and their "correctness" is tested by comparison to refractive index data on cubic crystals.

In the elpasolite lattice the contribution of F^- ions to the refractive index arises from six sites of C_{4v} symmetry, each of which, if acting alone, would be anisotropic. The polarizability appearing in the expressions for lattice-induced and self-induced dipolar crystal fields principally involves the F^- polarizability along the Ce-F bond axis, which is not the same as the polarizability which appears in an expression for the refractive index. Crystal field theory predicts that the polarizability along the Ce-F bond axis is enhanced at the expense of the transverse polarizability. The F^- ion sits on the bond axis directly between the Ce^{3+} and Na^+ ions, which are its nearest neighbors. This stabilizes excited d states on the F^- ion which contribute to the polarizability along the bond axis, and destabilizes excited d states which contribute to the transverse polarizability. In short, the polarizabilities in Table XII are only competitors for a lower bound.

However, if we assume the stretch-model bond lengths, we can use the data for Rb_2NaYF_6 to place tighter limits on α as follows. For x=2.2478, the splitting and centroid shift are given by

$$10Dq = 13197 + 2300\alpha + (10Dq)_{cov} \qquad (36a)$$

$$\Delta = -6720\alpha + \Delta_{cov} \qquad (36b)$$

The first term of (36a) is the point charge, and the second

term is the sum of the lattice-induced and self-induced dipole splittings. The first term of (36b) is the self-induced dipolar centroid shift. The last terms of both the Equations are positive covalent contributions. Equating (36a) and (36b) to the experimental values, and using the assumption that the covalent terms are positive, we obtain the inequalities,

$$13197 + 2300\alpha < 18200 \qquad (37a)$$

$$-6720\alpha < -13163 \qquad (37b)$$

This yields

$$1.96 < \alpha < 2.18 \qquad (38)$$

Use of the lower bound in (36a) and (36b) yields

$$(10Dq)_{cov} = 498$$

$$\Delta_{cov} = 0$$

and the upper bound yields

$$(10Dq)_{cov} = 0$$

$$\Delta_{cov} = 1454$$

The variation of both parameters is linear in α in between

the two extremes.

For Rb_2NaScF_6 (x=2.1795),

$$10Dq = 15397 + 2944\alpha + (10Dq)_{cov} \quad (39a)$$

$$\Delta = -8087\alpha + \Delta_{cov} \quad (39b)$$

In this case the bounds on α are far less restrictive than (38).

Let us now assume that α does not differ significantly in the two hosts and choose a value in the range (38) which yields the same $(10Dq)_{cov}/\Delta_{cov}$ ratio for both hosts. This criterion arises from the assumption in our model (Table IX) that the covalent contribution to both the splitting and the centroid shift vary exponentially with x with the same decay constant. This yields

$$\alpha = 2.02\ A^3$$

Rb_2NaYF_6:

$$(10Dq)_{cov} = 360$$

$$\Delta_{cov} = 402 \quad (40)$$

Rb_2NaScF_6:

$$(10Dq)_{cov} = 5460$$

$$\Delta_{cov} = 6102 \quad (41)$$

The estimates of (40) and (41) are clearly not intended to be accurate. The covalent splitting in (40) is of the

same order of magnitude as other corrections which were neglected in the model. Rather, these estimates give a rough indication of the importance of covalent effects, that is, whether they are negligible, dominant, or something in between. In Rb_2NaScF_6, which contains the smallest site, the covalent energies are several thousand wavenumbers, and contribute about a fifth of the splitting. For the larger site in Rb_2NaYF_6, the covalent terms are only a few hundred wavenumbers, though (40) is undoubtedly conservative, since attractive contributions to the splitting due to correlation were neglected in the model. Regardless of the uncertainties in the numbers, however, the qualitative behavior of the 5d levels (i.e., a higher centroid and an increased splitting for the smaller site) establishes that covalent contributions to the crystal field are important; they are not dominant, however, because if they were, the t_{2g} level would rise as the site size decreases.

Additional confirmation of this conclusion can be found by studying the spectrum of Ce:YLF. We have done low-temperature absorption measurements of this material, and Table XIII shows the 5d energy levels deduced from the band peak positions, along with the group theoretical labels assigned by Morrison [63]. Morrison calculated the theoretical 5d energies for Ce:YLF by scaling the phenomenological B_{kq} values for 4f electrons by the ratio $\langle r^k \rangle_{5d}/\langle r^k \rangle_{4f}$ obtained from Grossgut [64]. The resulting parameters are

listed in Table XIV along with the parameters determined directly from the data in Table XIII. In S_4 site symmetry, there are three independent parameters, and they are obtained exactly from the three independent splittings of Table XIII.

TABLE XIII 5d levels of Ce^{3+} in YLF

B (x^2-y^2)	51134
E (zx+izy)	49367
A (z^2)	41828
B (xy)	34004

TABLE XIV Crystal field parameters for Ce:YLF 5d electron

	EXPER.	$\langle r^k \rangle$ SCALING
B_{20}	6057	2340
B_{40}	-17649	-15577
B_{44}	21498	18549

The experimental fourth-rank parameters are only about 15% greater than those obtained by $\langle r^k \rangle$ scaling. The second-rank parameter is more than double, but it is small to begin with, and for the 4f electron, it is heavily shielded. If it is assumed that the 5d electron is unshielded, the theoretical B_{20} in Table XIV increases to 3600.

The $\langle r^k \rangle$ scaling procedure assumes the validity of Equation 2, or equivalently, Laplace's equation. Thus the differences between the theoretical and experimental values of B_{40} and B_{44} in Table XIV are estimates of the contributions of overlap and covalency effects (except for slight shielding corrections). The advantage of this procedure is that it requires no knowledge of nearest-neighbor distances or polarizabilities. The result confirms that covalent contributions to the splitting are small and positive (i.e., they make the ligands look somewhat more repulsive to the 5d electron.)

5.2 Elpasolite and YLF: Further Comparison

The Y^{3+} site in Rb_2NaYF_6 has six F^- neighbors at a distance of 2.1286 A, forming a perfect octahedron. Y^{3+} in YLF has eight F^- neighbors, at an average distance of 2.269 A, forming an almost perfect dodecahedron [69]. The fluorescence spectra of Ce^{3+} in the two hosts are very different. Ce:YLF displays a double-humped band with peaks at 310 and 325 nm [5]. This is due to transitions to the two spin-orbit-split multiplets of the 4f ground state. Ce^{3+} in Rb_2NaYF_6 displays a single broad band peaking at 390 nm, with nearly twice the energy half-width as the double-humped band in YLF. Originally, we suspected that the long emission wavelength in Rb_2NaYF_6 is due to a large splitting

produced by the octahedral coordination. That is, it was hypothesized that a dodecahedral coordination sphere is a closer approximation to a uniformly charged spherical shell than an octahedral coordination sphere. Purely on the basis of angular factors, the latter should produce a larger splitting. In particular, with octahedral coordination, the lobes of the e_g wavefunctions point directly at the ligands.

This hypothesis is not supported by the data, however. Inspection of Tables X and XIII shows that if the centroid and Stokes shift were the same for YLF and elpasolite, the emission in YLF would occur at an energy 3700 cm^{-1} less than the emission in elpasolite. A point charge model explains the reason for this. Table XV show the 5d energy levels for a perfect octahedron and for a perfect dodecahedron of negative point charges for a bond distance of 2.2 A. The $\langle r^2 \rangle$ and $\langle r^4 \rangle$ values of Grossgut [64] are used in the calculation, and the centroid is set to zero.

TABLE XV 5d splittings in a point charge model

Octahedron		Dodecahedron	
e_g	+8542	b_1	+3088
		e	+3066
		a_1	+457
t_{2g}	-5694	b_2	-9680

The hypothesis that a dodecahedral environment is "more isotropic" indeed seems to work for the levels that are destabilized by the ligands. The e_g state sustains 2.5 times the repulsion energy of the b_1 state. However, the levels which are most stabilized by the crystal field display the opposite pattern - the "more isotropic" environment produces a greater drop with respect to the centroid. In the case of the dodecahedron, the small repulsion energies for four of the five states require a large attraction energy for the remaining one (the b_2) in order to preserve the centroid.

The redshifted emission in elpasolite as compared to YLF arises mainly from differences in the centroid and the Stokes shift. The 5d centroid is 5340 cm^{-1} lower in elpasolite than in YLF (measured with respect to the ground state). The apparent Stokes shift (measured using 310 nm and 390 nm as the emission wavelengths in YLF and elpasolite, respectively) is 5000 cm^{-1} greater in elpasolite than in YLF. Both these factors favor longer-wavelength emission in elpasolite.

It is interesting to note that the 5d-4f centroid shift in YLF is -6450 cm^{-1}, compared to -13163 cm^{-1} in Rb_2NaYF_6; the latter is over twice as large. Yet the sum of e^2/R^6 over the ligands favors elpasolite by only 10%. The relatively small size of the covalent terms suggests that the effective F^- polarizability is lower in YLF than in

elpasolite.

Another important difference between YLF and Rb_2NaYF_6 is that the latter host produces much larger 4f splittings. Table XVI show the theoretical Ce^{3+} 4f levels in the two hosts predicted by Morrison [70] using lattice sums. In YLF, the weak-field coupling scheme is appropriate, as there are two groups of closely spaced levels separated by a 2400 cm^{-1} gap, which is mostly the spin-orbit splitting.

TABLE XVI 4f energy levels of Ce^{3+}

	YLF		Rb_2NaYF_6		
	Γ_{56}	0			
$^2F_{5/2}$	Γ_{78}	321	Γ_7	0	a_{2u}
	Γ_{56}	511	Γ_8	1941	
	Γ_{78}	2378	Γ_7	2612	t_{2u}
$^2F_{7/2}$	Γ_{56}	2439	Γ_8	4876	
	Γ_{78}	2606	Γ_6	5856	t_{1u}
	Γ_{56}	3307			

In elpasolite, however, the strong field labeling is more appropriate, since the levels fall into three groups. The right hand column of Table XVI shows the cubic strong field labels. At first, there seems to be a conflict between the behavior of the 5d splittings and the 4f

splittings. Elpasolite 4f splittings are much greater than YLF 4f splittings, but the total 5d splittings are very similar; the total separation of the YLF B levels in Table XIII is 17130 cm^{-1} compared to an 18200 cm^{-1} splitting in elpasolite. The answer to the paradox is that the 5d splitting in YLF includes a large contribution from B_{20}, which has a large radial parameter. In a point charge model for the 5d splittings, $\langle r^2 \rangle / R^3$ is roughly twice as large as $\langle r^4 \rangle / R^5$. In elpasolite, the 5d splitting must come entirely from the fourth-rank field, since B_{20} vanishes by symmetry. For the 4f electrons, however, the second-rank field is heavily shielded, and the competition is based on fourth- and sixth-rank fields. Thus the notion that elpasolite is "less isotropic" than YLF is confirmed by the 4f splittings. The dopant site in elpasolite is also tighter, as expected for a lower coordination number.

If spin-orbit interactions in elpasolite are neglected entirely, the 5d-to-4f fluorescent branching ratios to the three groups in Table XVI are easy to calculate, and are shown in Table XVII.

TABLE XVII 5d to 4f fluorescent branching ratios in a strong octahedral field

t_{2g} to a_{2u}	0.24
t_{2g} to t_{2u}	0.48
t_{2g} to t_{1u}	0.28

Thus, the peak of the emission band in elpasolite is close to the energy of the t_{2g} to t_{2u} transition. Therefore, use of the emission band peak to measure the Stokes shift overestimates it by more than 2000 cm^{-1}. The true Stokes shift in elpasolite is close to 4700 cm^{-1}, compared to 1750 cm^{-1} in YLF.

In short, the blue emission of Ce^{3+} in elpasolite arises from a large 5d centroid shift, a large Stokes shift, and large 4f splittings compared to YLF. The 5d splittings oppose rather than contribute to this difference. These results indicate that the site symmetry and coordination number are important design parameters for tunable 5d-to-4f lasers, but not simply because of angular crystal field parameters. Rather, different coordination spheres produce different values of ligand polarizability along the metal-ligand bond axis. In elpasolite, the line-of-sight alternation of cations and anions produces a strong attractive field on the ligand along the bond axis which enhances its polarizability along that axis, contributing to the 5d centroid drop. Point charge lattice sums [70] reveal that

the second-rank field on the fluoride ion along the bond axis is roughly three times greater in elpasolite than in YLF.

Emission to the three groups of levels in Table XVI are not resolvable in the elpasolite spectra, even at liquid helium temperature, although they are as widely separated as the two weak-field groups in YLF. Vibronic mode softening of the emitting 5d level is the only known mechanism which would produce such behavior, since the absorption bands to this level are much narrower. Even though the $Ce:Rb_2NaYF_6$ showed no clear signs of polarization memory, the absorption spectrum in Figure 27 shows two overlapping bands split by 800 cm^{-1} (which increases to as much as 1000 cm^{-1} if the bands are resolved). Indeed, the t_{2g} level should be split by the spin-orbit interaction into a Γ_8 and a Γ_7 level. Using the measured free-ion spin-orbit parameter, Morrison [63] determined that the Γ_7 should lie 1600 cm^{-1} above the Γ_8. Use of the free-ion spin-orbit Hamiltonian is justified in the crystal because ℓ is good quantum number. Sugano and Shulman show that in Ni^{2+}, covalency reduces the spin-orbit parameter by only 3%. Therefore, the most plausible mechanism underlying the 40% reduction observed here is the Ham effect. This is the amount of Ham reduction which occurs for a JT stabilization energy which is half the vibrational quantum, i.e., a few hundred wavenumbers. Therefore a consistent explanation for the broad emission and lack of

polarization memory is a pseudo-Jahn-Teller coupling between the spin-orbit-split levels of the t_{2g} which softens the mode for the emitting Γ_8 state without creating distortion minima deep enough to display polarization memory.

5.3 The Stokes shift

The Stokes shifts in the four elpasolites can be estimated by subtracting the peak energy of the lowest wavelength emission band from the t_{2g} energies in Table X. The results are shown in Table XVIII, and show a monotonic trend: the Stokes shift increases with site size, precisely the opposite of the Blasse hypothesis. Accounting for the 4f splittings reinforces the trend.

TABLE XVIII Uncorrected Stokes shifts for the elpasolites

Cs_2NaYF_6	8590
Rb_2NaYF_6	6870
K_2NaYF_6	6710
Rb_2NaScF_6	5690

The state of knowledge about the Stokes shift is not sufficiently advanced to make any claims about the physical reasons for the trend in Table XVIII. We have seen in chapter II (Equation 26) that for each symmetric or

JT-active mode, the contribution to the Stokes shift is determined by a competition between the first order vibronic coefficient for the emitting state and the background spring constant. It is impossible to say whether the trend in the table is due to smaller spring constants for the larger sites, larger vibronic couplings, or both.

Available data on Ce-doped fluorides does not support the notion that the Stokes shift is related to site size or site symmetry and coordination number by simple rules of thumb. Ce:Rb_2NaYF_6, for example, has a corrected Stokes shift of about 4700 cm^{-1}. The absence of a Jahn-Teller effect (i.e., low site symmetry) might be expected to produce a smaller Stokes shift, a hypothesis which works when comparing elpasolite and YLF. However, both Ce:LaF_3 and Ce:LuF_3 (a larger site and a smaller site, respectively, than elpasolite) produce larger Stokes shifts (5200 and 4800 cm^{-1}, respectively [71,72]). Thus, the only statement that can be confidently made about the Stokes shift is that it is sensitive to the specific arrangement of atoms in the environment of the emitting ion.

CHAPTER VI

CONCLUSIONS AND RECOMMENDATIONS

The qualitative dependence of the 5d levels on the lattice constant in the elpasolites clearly shows that covalency contributes significantly to the crystal field interactions. Our numerical estimates of these contributions are consistent with this conclusion. In Rb_2NaScF_6, for example, covalency accounts for roughly 20% of the 5d splitting.

The results of this work suggest design rules for choosing a fluoride host which redshifts the 5d-to-4f emission of Ce^{3+}. First, the alternation of nearest-neighbor cations and anions along a straight line, including the substituted cation, is a desirable host property; it creates an anisotropic crystal field at the ligand which enhances the ligand polarizability along the dopant-ligand bond axis, which in turn brings down the 5d centroid. Second, a tight, strong-field site is desirable, and this usually occurs for low coordination numbers (4 or 6). Third, a high site symmetry has the potential advantage of enhancing the Stokes shift through a Jahn-Teller effect on the emitting 5d level.

The factors limiting the amount of spectroscopic data

in this thesis were (1) the difficulties involved in the growth of single crystals, and (2) anomalous behavior which necessitated a time-consuming investigation to identify the normal Ce^{3+} site. Clearly, the spectroscopy cannot be divorced from materials preparation issues and chemical and structural analysis. An integrated approach to crystal physics research is necessary: an understanding of growth-related anomalies must temper the interpretation of spectroscopic data, and conversely, the insights yielded by spectroscopic evaluation must guide the search for new crystals.

Rb_2NaYF_6 and Rb_2NaScF_6 doped with cerium are promising tunable blue lasers spectroscopically. The t_{2g}-to-e_g excited-state absorption transition is strictly parity forbidden. The peak stimulated emission cross sections are approximately 10^{-18} cm^2. The best parts of the Bridgman-grown boules are clear and free of scattering, but are also very susceptible to cracking under mechanical and thermal stress, especially Rb_2NaYF_6. The materials are also not as hygroscopic as originally thought; at the time of this writing, samples have survived over a year in open air with no discernible moisture decomposition.

Better growth conditions may yield samples with much better mechanical and thermal properties, even for Rb_2NaYF_6. Further crystal growth research aimed at obtaining laser quality boules of elpasolites should be undertaken, with the

emphasis placed on Bridgman growth. Bridgman runs are less time consuming than Czochralski runs, and the Bridgman technique is free of evaporation troubles. This makes it feasible to experiment with several different compositions; for Rb_2NaYF_6 the best composition is the one which maximizes the extent of the elpasolite phase field and enters this field as soon as possible after the start of crystallization (i.e., while the melt is still relatively homogeneous). For Rb_2NaScF_6 a stoichiometric melt is the best starting point.

For Bridgman growth, differential thermal analysis should be done on the compositions used in order to determine the melting point. The Bridgman furnace should be a two-zone furnace, with the hot and cold zones separately temperature controlled. The crucible should be thin-walled so that thermal conduction in the walls does not blunt the temperature gradient in the melt. The crucible should also be wide enough to facilitate convective stirring. If these improvements do not yield laser quality boules, the compositions which work best can be tried in the Czochralski furnace using diameter control.

The spectroscopic evaluation of Ce-doped elpasolites suggests theoretical and experimental studies that are needed to improve on the estimates made in chapter V. Experimentally, more optical data on other hosts would be helpful, but other types of measurements are also needed, particularly to determine nearest-neighbor distances. One method is to do superhyperfine measurements to determine the

magnetic dipolar interaction energies between the Ce^{3+} and F^- nuclei. Another method is to measure x-ray absorption spectra. These spectra should display a sharp photoionization edge for the Ce 4f electron. The high-energy side of the edge should display oscillatory fine structure resulting from the scattering of the electron wave packet from the ligands; the bond distance can be determined accurately from this fine structure [73].

A major theoretical study which suggests itself is the calculation of ligand polarizabilities, particularly anisotropic contributions at a particular ligand site. Another useful study would be a covalency calculation, in the style of Sugano and Shulman, on the $(CeF_6)^{3-}$ complex. Also, the adequacy of Hartree-Fock free ion 5d wavefunctions should be investigated.

REFERENCES

1. John C. Walling, Otis G. Peterson, Hans P. Jenssen, Robert C. Morris, and E. Wayne O'Dell, "Tunable Alexandrite Lasers", *IEEE J QE QE-16*, 1302 (1980).

2. L. F. Johnson, R. E. Dietz, and H. J. Guggenheim, "Optical maser oscillation from Ni^{2+} in MgF_2 involving stimulated emission of phonons", *Phys Rev Lett 11*, 318 (1963).

3. L. F. Johnson, R. E. Dietz, and H. J. Guggenheim, "Spontaneous and stimulated emission from Co^{2+} ions in MgF_2 and ZnF_2", *Appl Phys Lett 5*, 21 (1964).

4. Donald S. McClure, *Electronic Spectra of Molecules and Ions in Crystals, Part II*, pp. 54-55, Academic Press, New York (1959).

5. D. J. Ehrlich, P. F. Moulton, and R. M. Osgood, Jr., "Ultraviolet Solid-State Ce:YLF Laser at 325 nm", *Optics Lett 4*, 184 (1979).

6. D. J. Ehrlich, P. F. Moulton, and R. M. Osgood, Jr., "Optically Pumped Ce:LaF_3 Laser at 286 nm", *Solid State Research, No. 2*, (Lincoln Laboratories, Lexington, MA, 1980).

7. W. J. Miniscalco, J. M. Pellegrino, and W. M. Yen, "Measurements of Excited-State Absorption in Ce^{3+}:YAG", *J Appl Phys 49*, 6109 (1979).

8. Ralph R. Jacobs, William F. Krupke, and Marvin J. Weber, "Measurement of Excited State Absorption Loss for Ce^{3+} in $Y_3Al_5O_{12}$ and Implications for Tunable 5d to 4f Rare-Earth Lasers", *Appl Phys Lett 33*, 410 (1978).

9. B. W. Bryant, "Spectra of Doubly and Triply Ionized Ytterbium, Yb III and Yb IV", *J Opt Soc Am 55*, 771 (1965).

10. J. Hernandez A, F. J. Lopez, H. Murrieta S, and J. Rubio O, "Optical absorption, emission, and excitation

spectra of Eu^{2+} in the alkali halides", *J Phys Soc Japan 50*, 225 (1981).

11. A. Bril, G. Blasse, and J. A. dePoorter, "Fast-Decay Phosphors", *J Electrochem Soc 117*, 346 (1970).

12. Clyde A. Morrison, *Lectures in Crystal Field Theory*, HDL-SR-82-8 (Harry Diamond Laboratories, Adelphi, MD, 1982).

13. Clyde A. Morrison, Gilberto F. de Sa, and Richard P. Leavitt, "Self-induced multipole contribution to the single-electron crystal field", *J Chem Phys 76*, 3899 (1982).

14. W. H. Kleiner, "Crystalline Field in Chrome Alum", *J Chem Phys 20*, 1784 (1952).

15. D. Garcia and M. Faucher, "Crystal-field parameters in rare-earth compounds: Extended charge contributions", *Phys Rev B 30*, 1703 (1984).

16. S. Sugano and R. G. Shulman, "Covalency Effects in $KNiF_3$", *Phys Rev 130*, 506, 512, and 517 (1963).

17. D. J. Newman, "Theory of Lanthanide Crystal Fields", *Adv. Phys. 20*, 197 (1971).

18. B. R. Judd, "Ionic transitions hypersensitive to environment", *J Chem Phys 70*, 4830 (1979).

19. Jeremy K. Burdett, *Molecular Shapes*, (Wiley, New York, 1980).

20. R. M. Sternheimer, "Shielding and Antishielding Effects for Various Ions and Atomic Systems", *Phys Rev 146*, 140 (1966).

21. G. D. Mahan, "Polarizabilities of Ions in Crystals", *Solid State Ionics 1*, 29 (1980).

22. G. Blasse and A. Bril, "Characteristic luminescence", *Philips Tech Rev 31*, 303 (1970).

23. R. Englman, *The Jahn-Teller Effect in Molecules and Crystals*, (Wiley, London, 1972).

24. I. B. Bersucker, *The Jahn-Teller Effect and Vibronic Interactions in Modern Chemistry*, (Plenum Press, New York, 1984).

25. I. B. Bersucker, *The Jahn-Teller Effect: A Bibliographic Review*, (IFI/Plenum, New York, 1984).

26. F. S. Ham, "Dynamical Jahn-Teller Effect in Paramagnetic Resonance Spectra: Orbital Reduction Factors and Partial Quenching of Spin-Orbit Interaction", *Phys Rev 138*, A1727 (1965).

27. C. W. Struck and F. Herzfeld, "Vibrational Levels of the ^{2}D-E State of Ce^{3+} in CaF_2", *J Chem Phys 44*, 464 (1966).

28. A. A. Kaplyanskii and A. K. Przhevuskii, "Deformation splitting and enhancement of spectral lines and the structure of excited levels of Eu^{2+} in alkali-earth fluoride crystals", *Opt Spec 19*, 331 (1965).

29. A. A. Kaplyanskii and A. K. Przhevuskii, "Piezospectroscopic study of the diagram of levels and transitions in Sm^{2+} ions in alkali-earth fluoride crystals", *Opt Spec 20*, 577 (1966).

30. L. L. Chase, "Microwave-Optical Double Resonance of the Metastable $4f^6 5d$ Level of Eu^{2+} in the Fluorite Lattices", *Phys Rev B2*, 2308 (1970).

31. R. L. Fulton and M. Gouterman, "Vibronic Coupling. II. Spectra of Dimers", *J Chem Phys 41*, 2280 (1964).

32. A. A. Kaplyanskii, V. N. Medvedev, and P. L. Smolyanskii, "Spectra, kinetics, and polarization of the luminescence of CaF_2-Yb^{2+} crystals", *Opt Spec 41*, 615 (1976).

33. S. A. Payne, A. B. Goldberg, and D. S. McClure, "One- and two- photon spectra of NaF: Cu^+: Jahn-Teller and vibronic coupling effects", *J Chem Phys 78*, 3688 (1983).

34. A. B. Goldberg, D. S. McClure, and C. Pedrini, "Optical absorption and emission spectra of Cu^+: NaF single crystals", *Chem Phys Lett 87*, 508 (1982).

35. R. Roy, "Multiple Ion Substitution in the Perovskite Lattice", *J Am Cer Soc 37*, 581 (1954).

36. J. G. Wurm, L. Gravel, and R. J. A. Potvin, "The Mechanism of Titanium Production by Electrolysis of Fused Halide Baths Containing Titanium Salts", *J Electrochem Soc 104*, 301 (1957).

37. F. H. Bright and J. G. Wurm, "New Fluoride Complexes of Trivalent Titanium", *Can J Chem 36*, 615 (1958).

38. K. Knox and D. W. Mitchell, "The preparation and structure of K_2NaCrF_6, K_2NaFeF_6, and K_2NaGaF_6", *J Inorg Nuc Chem 21*, 253 (1961).

39. G. Garton and B. M. Wanklyn, "Growth of Complex Fluoride Single Crystals by the Flux Method", *J Cryst Growth 1*, 49 (1967).

40. S. Aleonard et C. Pouzet, "Etude Cristallographique de Quelques Fluorures Complexes de Terres Rares de Formule A_2NaTF_6", *J Appl Cryst 1*, 113 (1968).

41. P. J. Nassiff, T. W. Couch, W. E. Hatfield, and J. F. Villa, "Magnetism and Spectroscopy of a Series of Hexafluorotitanates (III)", *Inorg Chem 10*, 368 (1971).

42. V. S. Schneider und R. Hoppe, "Uber neue Verbindungen Cs_2NaMF_6 und K_2NaMF_6 sowie uber Cs_2KMnF_6", *Z Anorg Allg Chem 376*, 268 (1970).

43. V. I. Siddiqi und R. Hoppe, "Zur Kenntis der Verbindungen Cs_2KSEF_6", *Z Anorg Allg Chem 374*, 225 (1970).

44. J. Chassaing, "New fluorine-containing compounds of scandium of the superperovskite structure", *Compt Rend Acad Sci C 272*, 209 (1971).

45. E. Bucher, H. J. Guggenheim, K. Andres, G. W. Hull, Jr., and A. S. Cooper, "Magnetic properties of some cubic rare-earth elpasolite hexafluorides", *Phys Rev B 10*, 2945 (1974).

46. P. Merchandt, J. Grannec, J. P. Chaminade, and Claude Fouassier, "Concentration Quenching of Nd^{3+} Fluorescence in Ordered Perovskite Oxides and Fluorides", *Mat Res Bull 15*, 1113 (1980).

47. E. J. Veenendal, H. B. Bron, and J. Ihringer, "Structural Phase Transitions in the Cubic Elpasolite Rb_2NaHoF_6", *Physica B 114*, 31 (1982).

48. E. P. Babaeva and G. A. Bukhalova, "The K, Na, Sc || F System", *Russ J Inorg Chem 10*, 791 (1965).

49. A. Vedrine, J. Besse, G. Baud, et M. Capestan, "Fluorures triples de structure perovskite, de sodium-potassium-rubidium ou cesium, de calcium et

d'yttrium-lanthane ou gallium. Substitution diverses entre ces elements", *Rev Chim Min 7*, 593 (1970).

50. P. Burkert, H. P. Fritz, and G. Stefaniak, "Structure of $[TiF_6]^{3-}$ in dipotassium sodium hexafluorotitanates (III)", *Z Nat B 23*, 872 (1968). In German.

51. G. A. Bukhalova and E. P. Babaeva, "The Cs^+, Li^+, Sc^{3+} || F^- System", *Russ J Inorg Chem 11*, 350 (1966).

52. P. W. Richter and C. W. F. T. Pistorius, "Phase diagram of K_3YF_6 and K_3SmF_6 to 35 kbar and 900 C", *High Temp - High Press 8*, 53 (1970).

53. R. E. Thoma, G. M. Hebert, H. Insley, and C. T. Weaver, "Phase Equilibria in the System Sodium Fluoride - Yttrium Fluoride", *Inorg Chem 2*, 1007b (1963).

54. R. E. Thoma and R. H. Karraker, "The Sodium Fluoride - Scandium Trifluoride System", *Inorg Chem 5*, 1934 (1966).

55. J. Chassaing, "Les fluorures ternaires d'yttrium et de rubidium", *J Inorg Nucl Chem 37*, 1554 (1975).

56. E. P. Babaeva and G. A. Bukhalova, "Interaction of Scandium Fluoride with Alkali Metal Fluoride", *Russ J Inorg Chem 11*, 1045 (1966).

57. Richard K. Chang, "Tunable Wavelength Solid-State Lasers and Turbulent Jet Diagnostics by Rayleigh and Fluorescence Scattering", *AFOSR-TR-82-0135* (1981).

58. Brian F. Aull, "The Computer-Controlled Spectroscopy System: An Operator's and Programmer's Manual", MIT Crystal Physics and Optical Electronics Laboratory internal memorandum, 1984.

59. Roger H. French, "Electronic Structure of Al_2O_3: VUV Reflectivity Measurement from Room Temperature to 1100 ^oC", Ph.D. thesis, MIT Department of Materials Science and Engineering, 1985.

60. Clyde Morrison, private communication.

61. J. C. Brice, *The Growth of Crystals from Liquids, Selected Topics in Solid State Physics, Vol. XII*, E. P. Wohlfarth, ed., North Holland Publishing, Amsterdam (1973).

62. J. C. Phillips, "On the Calculation of Crystal Field Parameters", *J Phys Chem Solids 11*, 226 (1959).

63. Clyde Morrison, "A Preliminary Investigation of Ce^{3+} in the Elpasolite and Scheelite Structures", *HDL-TL-83-4*, Harry Diamond Laboratories, Adelphi, MD, 1983.

64. P. Grossgut, "Analytical Wave Functions and Oscillator Strengths for Ce^{3+}, Pr^{3+}, Nd^{3+}, and Cu^{2+}", Ph.D. Dissertation, Texas Christian University, 1971.

65. C. Fainstein, M. Tovar, and C. Ramos, "Effect of uniaxial stress on the fluorine-transferred hyperfine parameters and lattice distortions in alkaline-earth fluorides with Tm^{2+} impurities", *Phys Rev B 25*, 3039 (1982).

66. P. C. Schmidt, Alarich Weiss, and T. P. Das, "Effect of crystal fields and self-consistency on dipole and quadrupole polarizabilities of closed-shell ions", *Phys Rev B 19*, 5525 (1979).

67. P. W. Fowler and P. A. Madden, "In-crystal polarizabilities of alkali and halide ions", *Phys Rev B 29*, 1035 (1984).

68. J. Norton Wilson and Richard M. Curtis, "Dipole Polarizabilities of Ions in Alkali Halide Crystals", *J Phys Chem 74*, 187 (1970).

69. C. Keller and H. Smutz, "Die Reaktion von Lithiumfluorid mit der Trifluoriden der Lanthaniden und einiger Actiniden", *J Inorg Nucl Chem 27*, 900 (1965).

70. Clyde Morrison, private communication.

71. W. S. Heaps, L. R. Elias, and W. M. Yen, "Vacuum-ultraviolet absorption bands of trivalent lanthanides in LaF_3", *Phys Rev B 13*, 94 (1976).

72. K. H. Yang and J. A. DeLuca, "UV fluorescence of cerium-doped lutetium and lanthanum trifluorides, potential tunable coherent sources from 2760 to 3220 Å", *Appl Phys Lett 31*, 594 (1977).

73. Prof. Bernard Wuensch, private communication.